AB-INITIO STUDY OF LITHIUM DYNAMICS IN SILICON-BASED MATERIALS FOR BATTERY APPLICATIONS

Dissertation présentée en vue de l'obtention du grade de
Docteur en Sciences de l'Ingénieur et Technologie

VISHANK KUMAR

SUPERVISOR:
Xavier Gonze

MEMBERS OF THE JURY:
Laurent Pizzagalli
Davide Di Stefano
Jean-François Gohy
Gian-Marco Rignanese (Secretary)
Bernard Nysten (Chairman)

UCLouvain

March 2020

Dedicated to my family, friends and teachers who shaped me the human being I am today.

ABSTRACT

Silicon-based materials are promising candidates to replace commercial graphite-based anodes in lithium ion batteries. Silicon-based anodes can possess 10 times more capacity than graphite, but with a humongous volume expansion of 300%. At the atomic scale, the rate of lithium migration plays a key role in controlling the volume expansion. Thus, understanding the lithium atom migration and the structural evolution of Si atoms at atomic scale is essential to mitigate volume expansion and achieve maximum capacity. In this thesis, we approached this problem from two ends: 1) Studying diffusion of lithium in bulk silicon and lithiated LiSi from first-principles methods within the transition state theory framework, and 2) Analysing delithiation dynamics through first-principles followed by an empirical potential to study large supercells. Our approach provides a better agreement with the experimental data as compared to the previous experimental or theoretical data with useful insight on the diffusion mechanism. The impact of quantum tunnelling effects and anharmonicity on lithium diffusion have also been estimated for the first time and are moderate for Si and negligible for the LiSi case. A novel first-principles-based approach has been developed to study the step-by-step delithiation of lithium atoms, which can capture the change in the local environment of silicon during delithiation. The analysis of the local environment of delithiated Si suggests that most of the delithiated silicon atoms (75%) returns back to the tetrahedral coordination. The characterization of delithiated silicon obtained by empirical potential shows strong resemblance with amorphous Si.

ACKNOWLEDGEMENTS

"I would rather have questions that cannot be answered than answers that cannot be questioned."

- Richard P. Feynman

Questioning knowledge and logical reasoning are the building blocks of wisdom and understanding. Sometimes intimidating, these basic actions have helped me in having a better understanding of natural phenomena by the means of physical laws and mathematics. I am not sure how much honest I have been to question basic knowledge before accepting it, but I can say that I tried my best to further develop my scientific questioning. A large part of it is owed to the conducive research environment of SC-17 laboratory and the proximity of good people with brilliant minds that populate it. They not only taught me science, but also provided a different perspective towards life in general that reshaped my thinking process.

First and foremost, I would like to sincerely thank my supervisor Prof. Xavier Gonze, who showed confidence in me, despite the fact that I did not have proper scientific training for theoretical work. His faith in my abilities always motivated me to try harder and often acted as a source of inspiration during difficult times. I cannot add anything to his already known scientific prowess, I have been very lucky to get an opportunity of working under his supervision. His attention to details, mathematical rigour, passion towards science and time management are some of the invaluable teachings I will take with me for life. I would also like to acknowledge his understanding nature and patience with which he taught me every small calculation and let me learn at my own pace. He was always a silent guardian watching out for me, but from a distance to let me grow and learn from my mistakes. My only regret is that I neither managed to play whist nor chess with him, I will look forward to such opportunities in future.

Next, I would like to acknowledge the guidance and support that Prof. Gian-Marco provided during the last four years, especially while preparing the manuscript of the paper and associated scientific discussion. Many thanks to Prof. Laurent Pizzagalli, Prof. Jean-Franc̈ois Gohy, Prof. Bernard Nysten and Davide Di Stefano for being the part of the jury for reviewing my PhD thesis. I am grateful for their constructive feedback, useful suggestions and insightful discussions that have helped in improving this manuscript significantly. I tried my best to incorporate all your suggestions in this final version of the manuscript.

Then, I would like to thank Prof. Sorin Melinte and Georgiana Sandu for including me in their projects that gave me an opportunity to explore the experimental research work outside our lab. I would also like to thank Prof. Jean-Christophe Charlier for his support during several BATWAL meetings and reports along with his incredible sense of humour. I would also like to thank Prof. Geoffroy Hautier for some fundamental discussions during group meetings, which sometimes induce intriguing coffee break research discussions.

Fourth, I would like to acknowledge those people who were knowingly unknowingly my scientific mentors, which include Benoît van Troeye, Matteo Giantomassi, Guido Petretto, Davide Di Stefano, Sriram and Anna Miglio. I am really thankful to you guys for all your scientific help, guidance and humbleness with which you used to explain me everything and bear with my ignorance. Especially to Benoît for sitting in front of me and answering all my stupid questions and for the evening music time in the lab that introduced me to belgian classics like Jacques Brel. I would also like to thank Jean-Jo and Marco to help me in getting up to speed with LAMMPS in the beginning and Jan for having interesting scientific discussions. Apart from science, I really enjoyed long philosophical discussions with Carina, Simon, Samuel, Maksim and David.

Fifth, I would like to give a big thanks to the hidden backbone of SC-17, i.e., Vinciane, Sadia, Jean-Michel and Fabienne. Thank you for making me feel at home, especially Sadia and Vinciane, without whom every administrative process is a night-

mare and with whom every drinks or lunch is fun and relaxing. You guys showed me the importance of personal life apart from work and how you treated me like a child and took care of me is unexplainable in any language. A big thanks for all the love and care you gave to me, without you I would not have the courage to cross the finishing line in the final days.

Sixth, I would like to acknowledge my team Namur led by Aurélie aka Cruella. I am still mad at you for leaving Pongo, when we used to make fun on Sriram and annoy Benoît. Anyways, thank you Cruella for your special affection towards Pongo and including this “real" Indian guy in events and gatherings. Also thank you Ricci and Pauline for your warmth presence in all the gatherings. I still remember the first time I met you Pauline and you pulled a prank on me, and I blamed poor Sriram. And Sriram, thank you for your love and affection that made me feel at home from the first day at lab and hosting me in Leuven after friday parties. Your confidence in me (sometimes unrealistic) to handle a situation often motivates me to keep up in difficult times. Special thanks to Benoît, Jonathan, David, Jean-Jo («sans atout»), Aurélien and Yannick for introducing me to card games where I learn my first few french words and numbers.

I would also like to thank people from ACIM: Ricky, Quentin, Guillaume, Andra, Arnaud and Nicolas without whom a non-french speaking guy like me could not have managed to do much in ACIM. I got so much love and respect from all of them, though I should mention they teased me a lot as well with Mr. President, but it was fun. Specially, George, Sergi and Volodia made a lot of fun but at the same time it created a joyful atmosphere in the lab. I am glad that I spend some fun time with great people of Sc-17 including Fnac, Martha, Bogdan, Henrique, Nicolas, Diana, Yasmine, Roman, Tushar, VietAnh, Viet-Hung, Janine, Yongchao, Khaoula, Wei, Andrés, Gil, Guodong. I apologize if I have missed someone, but believe me everyone in Sc-17 has been like a family to me and I am really thankful for all your warmth.

Then, I would like to thank my Indian friends, especially Ashwini, Ruchika, Saroj, Jyoti, Shashi, Varun, Mridul and San-

jay for playing cricket and preparing dinner together on weekends. I am also thankful to my Indian community in Louvain-la-Neuve (Atul, Itika, Koyel, Kaushal, Pooja, Vijay, Bob, Jason, Kiran, Ashish, Deepak, Ramesh, Raj, Palraj, Ramesh) for providing a homely environment and organizing several Indian festivals and get together.

A special thanks to my fake Belgian friend Francesca, my event planner, and a go to person for Exki or random sushi night, and a really sweet friend who helped me integrating in Louvain-la-Neuve. I am also glad that I made friends like Vanessa Kaden, Alice Tilquin, Alice Rokh, Alda (and baby Leo), Fred, Thibaut, Thibaut Gillet, Jeanne, Asseline, who tried their best to teach me French but instead learned some hindi words from me. Furthermore, I would like to thank Lisa for all her support, patience and amazing patisserie items. You gave me a new perspective towards art, literature and ecology (one day I will convince you how science can help ecology). I would also like to thank Robin, Mireille, Spip and Jason for the home-made food and affection. I am also thankful to my close friends Anish, Abhishek, Rahul Singh, Anshul, Siddharth, Alok and Aditya for watching over me and being in constant touch with me during difficult times.

Then, I have to thank the CÉCI and the CISM for having provided the clusters on which all the computations of this PhD work have been performed. Without them, this work could never have been done. I also acknowledge the BATTAB and BATWAL project grants for financial support.

Last but not the least, I would like to thank my parents for their blessings and being there for me. Especially my mom, often giving advice without completely knowing the subject, yet she was right most of the time. I don't know how you know the right words to say at the right time, but I always get motivated when I talk to you in difficult times. I am also greatly thankful to my brother and sister for sharing a lot of responsibilities at home during these last few years. Without the support of my family, I wouldn't be able to reach here today.

In last, I would like to thank each one of you who taught me small lessons of life and shaped me a better human being.

CONTENTS

List of Figures xiii
List of Tables xvii
List of Acronyms xix
1 INTRODUCTION 1
1.1 Working mechanism of a battery 4
1.2 Commercial anode material in LIB 9
1.3 Prospective anode materials 9
1.4 Li diffusion in Si-based anodes 12
1.5 Delithiation of silicon-based anodes 15
2 THEORETICAL BACKGROUND 17
2.1.1 Schrodinger equation 17
2.1.2 Born-Oppenheimer approximation 18
2.2 Density Functional Theory 19
2.2.1 Hohenberg and Kohn theorem 20
2.2.2 Kohn-Sham formulation 22
2.2.3 Exchange-correlation energy 24
2.2.4 Structural relaxation 25
2.3 Density Functional Perturbation Theory 26
2.3.1 Introduction 27
2.3.2 Response functions 27
2.3.3 Interatomic force constants and phonon frequencies 30
2.4 Diffusion 32
2.4.1 Introduction 32
2.4.2 Driving force for diffusion 33
2.4.3 Fundamental concepts of diffusion 35
2.4.4 Classical transition state theory 41
2.4.5 Quantum mechanical effects in TST 45
2.4.6 Anharmonic effects 51
2.4.7 Kinetic Monte Carlo method 52
2.5 Classical potentials 55
2.6 Chemenv tool 56
3 DIFFUSION OF LI IN BULK SI AND CRYSTALLINE LISI 59

3.1 Introduction . . . 59
3.2 Computational details . . . 63
3.3 Li diffusion in bulk Si . . . 65
3.3.1 Li insertion into bulk Si . . . 65
3.3.2 Diffusion mechanism: Interstitial diffusion . . . 68
3.3.3 Effect of quantum mechanical approximation . . . 72
3.3.4 Effect of mass rescaling . . . 76
3.3.5 Effect of anharmonicity . . . 80
3.3.6 Discussion . . . 83
3.4 Li diffusion in LiSi . . . 87
3.4.1 Bulk LiSi and Li vacancy effect . . . 87
3.4.2 Migration path and energy barrier . . . 89
3.4.3 Phonon calculations . . . 91
3.4.4 Effective diffusion coefficient: KMC . . . 92
3.4.5 Effect of anharmonicity . . . 95
3.4.6 Discussion . . . 100
3.5 Conclusion . . . 102
4 DELITHIATION OF C-$Li_{13}Si_4$ BY FIRST-PRINCIPLES 105
4.1 Introduction . . . 105
4.2 Computational details . . . 106
4.2.1 Delithiation protocol . . . 107
4.2.2 Characterization: . . . 109
4.3 Structure of $Li_{13}Si_4$ . . . 110
4.4 Volume and formation energy . . . 112
4.5 Structural evolution of Si atoms . . . 117
4.6 Delithiated Silicon . . . 124
5 DELITHIATION USING CLASSICAL POTENTIALS 127
5.1 Validation of MEAM potential . . . 127
5.2 Simulation Method . . . 131
5.3 Delithiated Silicon . . . 133
6 CONCLUSIONS AND PERSPECTIVE 141
A CONVERGENCE RESULTS 147
B COORDINATION ENVIRONMENTS 155
C SCIENTIFIC COMMUNICATION 157
Bibliography 159

LIST OF FIGURES

Figure 1.1	Growing CO_2 level in the atmosphere	2
Figure 1.2	Schematic of a commercial Li-ion battery	5
Figure 1.3	Different types of batteries	6
Figure 1.4	Open circuit diagram for a Li-ion battery	7
Figure 1.5	Prospective cathode and anode materials	8
Figure 1.6	Illustration of structural changes in silicon nanostructures	12
Figure 1.7	TEM images showing the formation a-Li_xSi layer during lithiation	13
Figure 2.1	Gibbs free energy and chemical potential change	35
Figure 2.2	Illustration showing parameters of Chemenv tool	57
Figure 3.1	Electronic density of states of bulk Si with 1 Li atom	66
Figure 3.2	Phonon band structures	67
Figure 3.3	Partial phonon density of states	67
Figure 3.4	Diffusion barrier calculated by the NEB method	69
Figure 3.5	Partial phonon density of states at initial and saddle points	70
Figure 3.6	Vibrational free energy change	71
Figure 3.7	Calculated diffusion coefficient	72
Figure 3.8	Effect of quantum corrections	73
Figure 3.9	Effective activation barrier and diffusion prefactor	74
Figure 3.10	Tunneling correction factor (Γ)	75
Figure 3.11	Effect of mass scaling on vibrational free energy	77
Figure 3.12	Effect of mass scaling on diffusion coefficient	78
Figure 3.13	Quantum corrections with mass rescaling	79

Figure 3.14 Quantum tunneling corrections with mass rescaling . . . 80
Figure 3.15 Diffusion barrier with anharmonic effects 81
Figure 3.16 Diffusion coefficient with anharmonic effects . . . 82
Figure 3.17 Effect of anharmonicity on diffusion . . . 84
Figure 3.18 Crystal structure of LiSi . . . 88
Figure 3.19 Electronic density of states of LiSi . . . 89
Figure 3.20 NEB profile for different Li vacancy jumps in LiSi . . . 91
Figure 3.21 Vibrational free energy change for Li vacancy jumps . . . 92
Figure 3.22 Kinetic Monte Carlo statistics . . . 94
Figure 3.23 Effective Li diffusion coefficient in LiSi . . . 95
Figure 3.24 Volume expansion curve for LiSi structure 96
Figure 3.25 Temperature dependence of the LiSi bulk modulus . . . 96
Figure 3.26 Diffusion barrier with anharmonic effects 98
Figure 3.27 Effective diffusion coefficient with anharmonic effects . . . 99
Figure 3.28 Effect of anharmonicity on Li diffusion in LiSi . . . 100
Figure 4.1 Delithiation workflow . . . 108
Figure 4.2 Crystal structure of primitive $Li_{13}Si_4$ cell . 111
Figure 4.3 Illustration of few local environments . . 111
Figure 4.4 Fractional volume change . . . 113
Figure 4.5 Formation energies . . . 114
Figure 4.6 Crystal structure of intermediate steps . . 115
Figure 4.7 Potential-composition curve . . . 116
Figure 4.8 Radial distribution functions . . . 118
Figure 4.9 Radial distribution function: delithiated Si 119
Figure 4.10 Evolution of coordination number . . . 120
Figure 4.11 Average Li neighbours . . . 122
Figure 4.12 Average Si neighbours . . . 123
Figure 4.13 Partial neighbour count method . . . 124
Figure 4.14 Structures and RDF of delithiated Si . . . 126
Figure 5.1 Cohesive energy of Li_xSi alloys . . . 128

Figure 5.2 Volume of formation of Li_xSi alloys 130
Figure 5.3 Illustration of model setup for delithiation 134
Figure 5.4 Two snapshots of delithiation process . . 134
Figure 5.5 Density of delithiated Si 136
Figure 5.6 Radial Distribution Functions of delithiated Si compared with a-Si 137
Figure 5.7 Comparison of a-Si RDF with different potentials 138
Figure 5.8 Rings statistics for a-Si and delithiated Si 139
Figure A.1 Diffusion barriers with varying cell size of bulk Si 147
Figure A.2 NEB profile with varying cell size of LiSi 148
Figure A.3 Diffusion coefficient with varying cell size of LiSi 149
Figure A.4 Effect of quantum tunneling corrections with varying cell size of LiSi 150
Figure A.5 Effective Li diffusion coefficient with varying cell size of LiSi 151
Figure A.6 Phonon band structure of LiSi 151
Figure A.7 Volume expansion curve for bulk Si . . . 152
Figure A.8 Temperature dependency of bulk modulus of Si 153
Figure B.1 Schematic of some common coordination environments 155

LIST OF TABLES

Table 3.1	Li vacancy jump parameters in LiSi	90
Table 4.1	Lattice parameters of $Li_{13}Si_4$	112
Table 5.1	Bulk properties of Li_xSi alloys	132
Table A.1	Li vacancy migration with varying cell size of LiSi	148

ACRONYMS AND ABBREVIATIONS

AFM	Atomic Force Microscopy.
AGW	Anthropogenic Global Warming.
AIMD	Ab initio molecular dynamics.
ASR	Acoustic Sum Rule.
BCC	Body Centered Cubic.
BFGS	Broyeden-Fletcher-Goldfarb-Shanno.
BO	Born-Oppenheimer.
CG	Conjugate Gradient.
CI-NEB	Climbing Image Nudged Elastic Band.
CN	Coordination Number.
CNT	Carbon Nano Tubes.
DFPT	Density Functional Perturbation Theory.
DFT	Density Functional Theory.
DOS	Density of States.
EAM	Embedded Atom Method.
EIS	Electrochemical Impedance Spectroscopy.
ESM	Electrochemical Strain Mapping.
EV	Electric Vehicles.
FCC	Face Centered Cubic.
GGA	Generalized Gradient Approximation.
GGA-PBE	Generalized-Gradient Approximation in the Perdew-Burke-Ernzerhof formulation.
GITT	Galvanostatic intermittent titration technique.
H_x	Hexagonal void.
HOMO	Highest Occupied Molecular Orbital.
IFC	Interatomic Force Constant.
IPCC	Intergovernmental Panel for Climate Change.
KMC	Kinetic Monte Carlo.
L-BFGS	Low memory BFGS.
LDA	Local Density Approximation.

LED	Light Emitting Diode.
LIB	Li-ion batteries.
LUMO	Lowest Unoccupied Molecular Orbital.
MD	Molecular Dynamics.
MEAM	Modified Embedded Atom Method.
MEP	Minimum Energy Path.
MSD	Mean-Squared Displacement.
NEB	Nudged Elastic Band.
NMR	Nuclear Magnetic Resonance.
NPT	Nose-Hover Thermostat with constant number of atoms, pressure and temperature.
NVT	Nose-Hover Thermostat with constant number of atoms, volume and temperature.
NW	Nanowires.
ONCVPSP	Optimized Norm-Conserving Pseudopotential.
PDE	Partial Differential Equation.
PITT	Potentiostatic intermittent titration technique.
PPDOS	Partial Phonon Density of States.
QHA	Quasi-harmonic Approximation.
RDF	Radial Distribution Function.
Reaxff	Reactive Force-Field.
SCF	Self-Consistent Field.
SEI	Solid Electrolyte Interface.
SS:4	See-saw geometry.
SW	Stillinger-Weber potential.
T_d	Tetrahedral void.
T:4	Tetrahedral geometry.
TEM	Transmission Electron Microscopy.
TST	Transition State Theory.
ZPE	Zero Point Energy.

1

INTRODUCTION

Climate change or global warming is one of the biggest problems that life is facing on earth. There was a large debate on whether the global warming is a cyclic process of glacial advance and retreat due to the movement of earth's tectonic plates or it is a man made/Anthropogenic Global Warming (AGW). Systematic research has confirmed that it is an anthropogenic event as more than 97% of the ~12,000 scientific papers published on climate change, agrees that human activities are causing global warming [1, 2].

The earth's temperature has fluctuated in a cyclic way throughout its history as represented by the CO_2 level in Fig. 1.1. In the last roughly 650,000 years there have been 7 cycles of glacial advance and retreat with the last end of ice age marking the beginning of human civilization roughly 11,000 years ago [3]. However, the level of CO_2 has never been as high as the post industrialization era suggesting it as an anthropogenic event. Numerous evidences of global warming have been reported such as the increase in earth's temperature, glaciers retreat, increase of sea level and extreme hot conditions in some parts of the world where climate change is already a matter of life and death [4, 5].

These growing concerns of climate change is not only subjected to a part of the world but affects everyone in one way or the other. Thus, all the major countries participated in the Paris climate agreement, signed in 2016, to take effective measures for limiting the human induced global warming. Based on scientific evidences, the Intergovernmental Panel for Climate Change (IPCC) suggested policy makers to limit their carbon emission to keep the increase in global average temperature below 2°C above pre-industrial levels [5]. Although the required efforts to meet the expectations of the Paris agreement is relatively debated [7, 8], it pushes the policy makers to move from fossil fuels to renewable energy sources on an urgent basis.

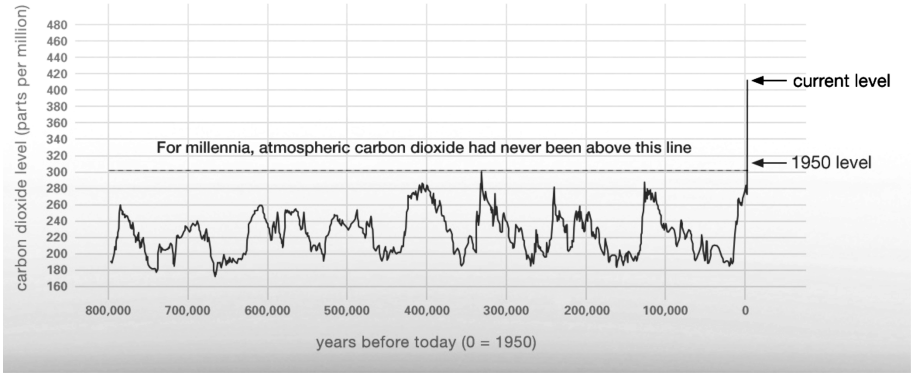

Figure 1.1: Growing CO_2 level in the atmosphere computed from the comparison of ice cores and more recent direct measurements [3]. Plot adapted from "NASA's Global Climate Change website" [6]

Scientific research has played a significant role in coming up with innovative solutions to provide alternate green energy solutions to the policymakers. Whether it is in the field of energy generation (finding organic materials for photovoltaic cells [9]), or for energy consumption (e.g. search for new Light Emitting Diode (LED) materials [10]), or for efficient energy storage [11]. The technological advancement, especially in the energy storage plays a central role in the life cycle of energy creation and consumption irrespective of source and consumption. For example, two main sources of renewable energy, wind and solar energy, are intermittent and require efficient storage units to supply power when there is no wind for the former and no sun for the latter, respectively. Other renewable energy sources like nuclear reactors and geothermal energy also benefit from energy storage and transmission.

The energy can be stored mechanically (hydroelectric dams), thermally (thermal energy storage), chemically (hydrogen storage), electrochemically (batteries) or electrically (capacitors). However, our current storage technologies are not sufficient for the growing energy demand and will increase further with more renewable energy generated by solar and wind energy. Some key limitations are environmental consequences and geographical

limitations (dams), energy leakage (capacitors), energy density and capacity (batteries), etc.

Out of the above-mentioned technologies, batteries have a wide range of applications from small portable devices to electric vehicles [12]. Specifically, Li-ion batteries (LIB) are the most commonly used batteries owing to their higher energy density, higher operating voltage, lower cost and longer life-cycle as compared to other alternatives [13]. However, the current commercially available Li-ion batteries are not sufficient to meet the high energy density demand of electric vehicles (EV) or high capacity demand of power grids [14]. In portable devices, they occupy a significantly large volume and limit the designing capability to make smaller devices. Thus, there is a huge demand to make smaller batteries and/or increasing the time between two consecutive charges. Moreover, incidents of battery failure, ranging from portable mobile phones to EV's and airplanes, have raised serious safety concerns over the Li-ion batteries [15, 16]. Thus, researchers have been actively working on augmenting the capacity of existing Li-ion batteries [17], designing safer solid state batteries [18], or replacing Li with Na-ion batteries [19] avoiding environmental hazard of Li mining [20]. The interdisciplinary nature of the problem, involving materials science, electrical engineering, electrochemistry, health and environmental science, makes it an enormously challenging problem of the 21st century. The importance of this problem can be felt in the fact that the Nobel prize of 2019 in Chemistry was awarded to three researchers (John Goodenough, M. Stanley Whittingham and Akira Yoshino) for the development of Li-ion batteries [21].

In this thesis, we will address the material perspective of the LIB problem and associated limitations for commercial applications. More precisely, we will focus on the application of silicon-based materials for anodes, Li migration in them and the structural changes during charging and discharging. In this scope, the application of first-principles-based methods to study Li migration will be discussed, along with the validation of associated approximations and limitations. The structural changes that silicon atoms undergo during charging and discharging will also be in-

vestigated followed by future potential to use this information in designing next-generation batteries. The first section briefly introduces the basics of a LIB.

1.1 WORKING MECHANISM OF A BATTERY

This section introduces the reader to the basic working principles of a Li-ion battery and areas of opportunities for designing next generation batteries. The section is largely based on various review papers on LIB [17, 19, 22].

Fig. 1.2 shows a schematic representation of a LIB and all its vital components. It consists of a positive electrode (cathode) and a negative electrode (anode) immersed in a liquid electrolyte that acts as an ionic carrier to transport Li^+ ions from one electrode to the other and a separator that avoids electron transfer. In a commercial LIB, normally $LiCoO_2$ is used as cathode, though other metals oxides of form Li_xMO_2 (M =Mn, Al, Ni) can also be used. The anode is graphite and the electrolyte typically consists of a lithium salt ($LiPF_6$) in an organic solvent [19]. During discharging of a battery, the current is generated by the following electrochemical reactions at the two electrodes:

$$\text{Anode: } Li_xC_6(s) \longrightarrow xLi^+(soln) + 6C(s) + xe^- \tag{1.1}$$

$$\text{Cathode: } Li_{1-x}CoO_2(s) + xLi^+(soln) + xe^- \longrightarrow LiCoO_2 \tag{1.2}$$

The Li^+ ion and e^- generated at the anode migrate to cathode to complete the cell reaction, where the former migrate via the electrolyte and the latter goes through the load (providing current to the device). The layered structure of both the electrodes facilitate the movement of Li ions from one interlayer location at anode (graphite intercalation) to another interlayer location between CoO_2 crystals. During charging of a battery, a voltage is applied across the electrodes that reverses the abovementioned reactions and forces lithium ions to move from the $LiCoO_2$ crystal to be intercalated between graphite sheets at anode. The potential application of this intercalation behaviour led

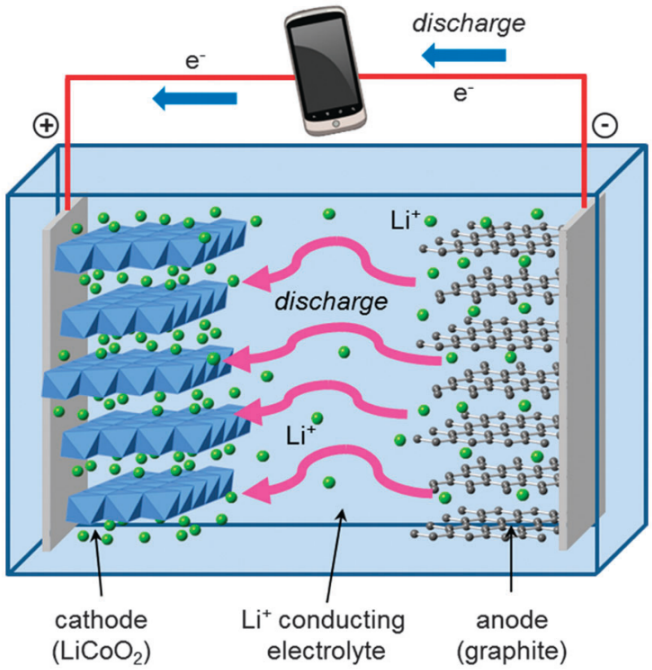

Figure 1.2: Schematic representation of a commercial Li-ion battery. Extracted from Ref. [19] - Published by The Royal Society of Chemistry

the commercialization of these electrodes for LIB and the process has been optimized over the years [19].

The design of LIB's has evolved in the last 2 decades to cater different applications. Fig. 1.3 shows 4 common types of batteries we use in daily applications, along with a schematic representation of different components.

The selection of electrodes (anode and cathode) has to be in agreement with their electrochemical stability in presence of the electrolyte. For instance, an anode with an electrochemical potential μ_A greater than the Lowest Unoccupied Molecular Orbital (LUMO) of the electrolyte will reduce the electrolyte. Similarly, a cathode of electrochemical potential μ_C lower than the Highest Occupied Molecular Orbital (HOMO) will oxidize the electrolyte [17]. The reaction between the electrolyte and the electrodes can lead to loss of active material from electrodes resulting in significant capacity fading and poor cyclability, i.e. capa-

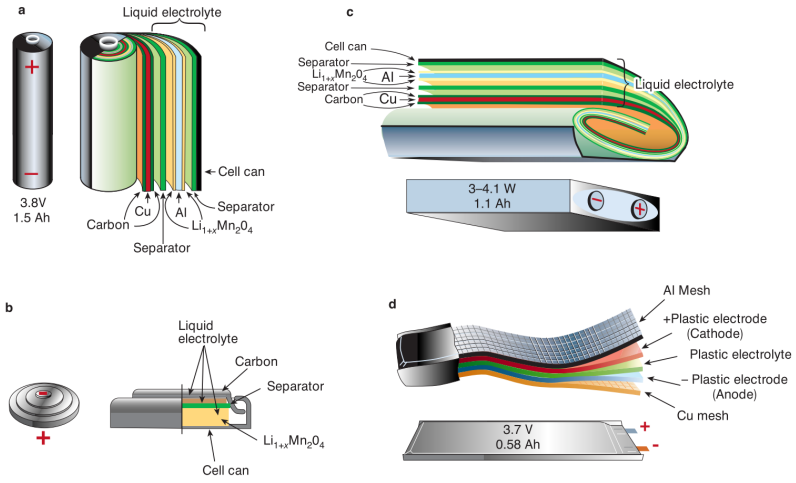

Figure 1.3: Schematic drawing of different types of batteries and their essential battery components for a) cylindrical, b) coin, c) prismatic, and d) thin and flat Li-ion batteries. Reprinted by permission from Springer Nature: Nature (Ref. [13]), Copyright 2001.

city loss after few charge-discharge cycles. This can be avoided either by selecting the electrodes with electrochemical potentials μ_A and μ_C similar to LUMO and HOMO of the electrolyte, or by a passivation layer (SEI) that blocks electron transfer while maintaining fast Li^+ ion migration between the active material and the electrolyte (refer Fig. 1.4).

The existing technology of a commercial LIB is highly optimized incorporating these above-mentioned limitations. However, the technology in itself has reached a saturation point mainly limited by material constraints. Thus, to cater growing energy demands of EV's, power grids and small portable devices, innovation is demanded for finding new materials to upgrade existing components. Moreover, for an economically viable and sustainable solution, the next-generation battery materials should be readily available and environmental friendly [19]. For instance, the CoO_2 can be replaced by other multivalent elements such as Fe or Mn to increase the capacity while maintaining the layered oxide structure for easy Li intercalation. Similarly, the flammable

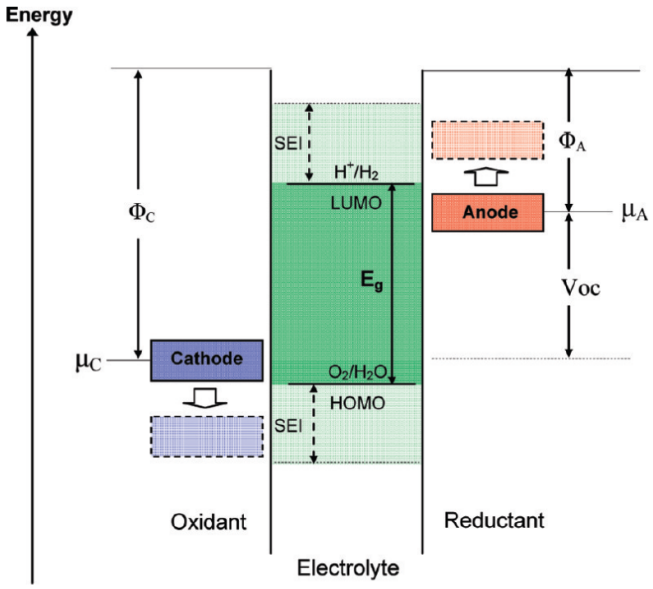

Figure 1.4: Schematic of the open circuit diagram for a Li-ion battery showing the energy window E_g of the thermodynamical stability of electrolyte to select cathodes and anodes. Φ_A and Φ_C are the workfunctions of anode and cathode, respectively. Reprinted with permission from Ref. [17]. Copyright 2010 American Chemical Society.

liquid electrolyte that has resulted in thermal hazards [15] can be replaced with safer solid-state electrolytes [23]. On the other side, replacing standard graphitic anodes with materials of higher specific capacity (amount of charge stored per gram) will open new commercial market for LIB applications. Some of these prospective anode materials (silicon and lithium metal) show as high as 10× more capacity than graphite as shown in Fig. 1.5.

Replacing the graphitic anode by these high capacity anodes will significantly reduce the battery size or increase the capacity by accommodating more active material. It will facilitate the option to either design smaller portable devices which are, at present, restricted by the battery size or make EVs that can go longer distance within one charge. One can choose depending on the end application. Although these new materials look promising, different issues limit their commercial development.

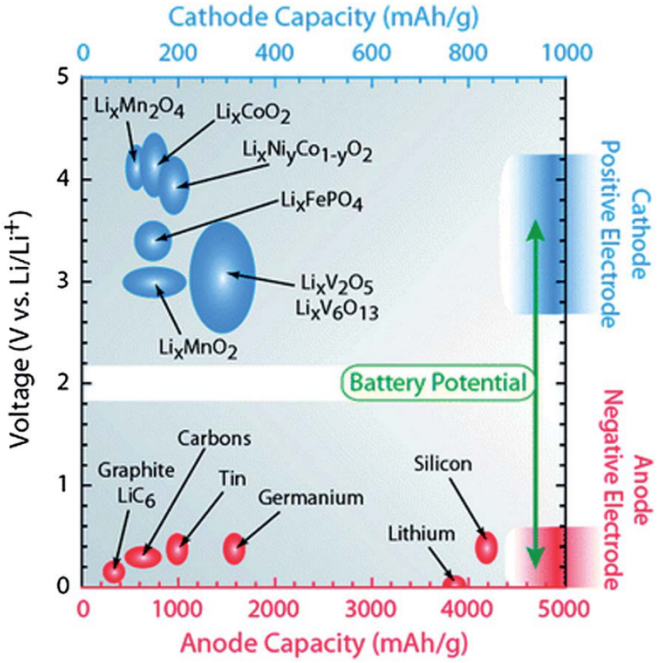

Figure 1.5: Diagram illustrating capacity of prospective cathode and anode materials along with electrochemical reduction potential compared to Li metal. Reproduced from Ref. [24] with permission from The Royal Society of Chemistry.

For instance, new cathode materials (such as $LiFePO_4$) do not always form a layered structure restricting the Li^+ ion migration only to 1-D channels, which can then be easily blocked by defects [19]; solid-state electrolytes show lower ionic conductivity as compared to the liquid counterpart [25]. On the anode side, prospective materials replacing graphite show poor cyclability caused either due to mechanical failure of anodes [26], the loss of electrical contact [27], or due to the Solid Electrolyte Interface (SEI) formation [28] or due to the formation of Li dendrites (only in bulk lithium anodes) [13]. Thus, the development of next-generation battery, even from just the materials perspective, is three-fold: to find new low cost and environmentally benign materials for (1) a thermodynamically stable solid-state electrolyte with a high Li^+-ion conductivity, (2) an anode, and (3) a cathode with electrochemical potential μ_A and μ_C matching

with the LUMO and HOMO of the electrolyte. Going forward in this thesis we will only focus on the anode part of this challenging three-fold problem and the following sections introduce the working of a commercial anode material in LIB.

1.2 COMMERCIAL ANODE MATERIAL IN LIB

In commercial LIB, graphite is the standard anode material with a gravimetric capacity of (370 mAh/g). During charging, graphite stores Li^+ ions in between graphene sheets up to a concentration of LiC_6 for an applied voltage difference of 0.3 V [19]. The sp^2 hybridized carbon atoms in graphite form strong C-C bonds in-plane with half-filled p_z orbitals out-of plane [17]. These half-filled p_z orbitals can interact with the 2s orbitals of Li atoms sitting on top of hexagonal centres of graphene, separated by a few Å. This Li-C bonding maintains the mechanical integrity of graphite during intercalation and limits the volume expansion.

As mentioned in the previous section, the interface with electrolyte and the formation of SEI layer plays an important role in the mechanical stability of anodes and overall cyclability of the battery. For graphite, an organic solvent (a blend of ethylene carbonate and diethyl carbonate), identified in the early years of lithium-ion batteries [29], limits and stabilize the formation of SEI in the first charge-discharge cycle, otherwise ever growing. Thus, a stable conductive SEI layer and a negligible volume expansion in Li intercalation between graphene layers, largely explains the good cyclability of graphitic anodes. This also highlights one of the key issues with the next-generation anode materials that suffer from poor cyclability either due to large volume expansion or unstable SEI formation. The next section covers these new prospective materials and associated problems.

1.3 PROSPECTIVE ANODE MATERIALS

The intercalation mechanism in graphite provides an efficient way of Li^+-ion insertion and removal while minimizing the volume

expansion, but it also limits the maximum number of Li atoms stored per host atom. In graphite this ratio is 0.1667 (1/6) for most lithiated LiC_6 structure. To overcome this limitation, most of the next-generation anode materials are based on alloy formation, which is also sometimes refered as Type B or conversion materials [30]. As the name suggests, these materials convert and undergo structural transformation to form lithiated alloys during lithiation (charging of the battery). The alloy formation allow to increase the Li:host ratio as high as 4.4 for silicon forming $Li_{22}Si_5$ [31] or 3 for phosphorus forming Li_3P [32] upon lithiation resulting in theoretical gravimetric capacity of ~4400 mAh/g and ~2500 mAh/g, respectively. Experiments suggest that the maximum possible lithiated level for silicon at room temperature is close to $Li_{15}Si_4$ [33, 34], which gives a ratio of 3.75 Li atoms per Si atom that is way higher than for graphite.

The alloy formation ability of these new anode materials on one hand benefit from alloying capability to store more Li atoms, on the other hand, induces huge volume expansion. For instance, the alloy formation in both silicon and phosphorus is accompanied by a huge volume change (~200-300%) [33, 35] to accommodate the large amount of Li atoms, which can not be endured mechanically by the material [36]. Moreover, the structural transformation changes the crystallographic orientation and local environments of host atoms [31, 37], which often leads to the breaking of SEI and the loss of electrical contact [38]. Furthermore, the breaking of SEI would expose the anode for reduction, leading to a loss of active material and reduced Li diffusion through thicker SEI interface [28]. These factors mainly associated with volume change result in significant capacity loss within the first few cycles [35].

Another material of interest is Lithium metal that got renewed scientific interest owing to its high specific capacity, low density, and lowest redox potential [28]. Its commercial potential as an anode material was first observed by Whittingham in 1976 [39] that motivated Exxon to commercialize its development as an anode material in LIB [22]. Unfortunately, the formation of Li dendrites had limited its development. These Li dend-

rites grow upon extensive cycling and reach cathode by penetrating the SEI layer, resulting in short circuiting the battery leading to dangerous thermal hazards [22]. This material has been revisited by scientists recently in hope of finding a suitable SEI formation mechanism that can limit the dendritic formation, which up to the best of our knowledge has not yet been tackled entirely. Thus, these new prospective materials show huge potential to improve the capacity of LIBs but with associated challenges that motivate researchers to bring innovative solutions. More specifically, in terms of silicon/phosphorus, the innovative use of nanocomposites and nanoengineering has shown promising results in tackling the main problem of volume expansion and a significant improvement in cyclability [14, 40].

The use of nanostructures limits the volume expansion in 1-D (for nanowires), 2-D(nanotubes or nanoribbons) or in a relatively small 3-D space (nanospheres) and provides a greater design control to accommodate the volume expansion while maintaining the mechanical integrity [41, 42]. The nanoengineering of anodes results in better cyclability and better overall performance as compared to their bulk counterparts as shown in the schematic illustration in Fig. 1.6 [43].

This elegant solution significantly increased the practical application of silicon-based anodes [41, 44, 45]. Though, the problem of forming a stable SEI becomes more tricky as the use of nanostructures increase the surface area to volume ratio. Several options to overcome the issue have been suggested for surface passivation [27, 46, 47]. Not exhaustively for silicon, suggestions include: carbon coating of silicon nanowires [42], encapsulation by carbon spheres [46, 48], mixing carbon nanotubes (CNT) with silicon nanowires (NW) [49, 50], etc. The benefit of using carbon here is 2-fold. Firstly, it provides the mechanical integrity as it has lower affinity towards lithium and thus acts as an elastic buffer for silicon/phosphorus to expand. Secondly, it enhances the electrical conductivity as it is a better conductor than silicon/phosphorus. The use of carbon-based nanocomposites increase the stability of anodes but at the expense of active materials, a compromise which might be fair depending on the end

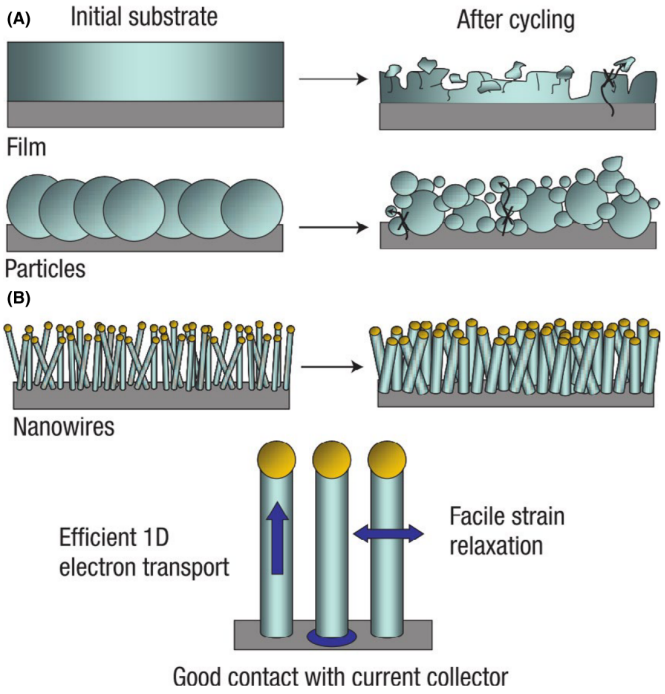

Figure 1.6: Illustration of structural changes that different nanostructures undergo upon several lithiation-delithiation cycles. Silicon NW show better performance than thin films and microparticles. Reprinted by permission from Nature Springer: Nature Nanotechnology (Ref. [43]), Copyright 2007.

application. Nonetheless, the underlying mechanism of phase transformation during lithiation have to be understood. Since this is largely governed by the reaction rate and diffusion of Li atoms, the next section focuses on the importance of Li diffusion in lithiation/delithiation mechanism at the atomic scale.

1.4 LI DIFFUSION IN SI-BASED ANODES

During initial lithiation of Si-based anodes, Li atoms are adsorbed at the surface forming a layer of amorphous Li_xSi (a-Li_xSi), through which they diffuse to reach the bulk Si (two phase reaction) [51–53] (see Fig. 1.7). The rate of further lithiation then depends on the interplay between the Li diffusion

rate and the reaction rate of Si-Si bond breaking and of Li-Si bond formation [54, 55]. Nanostructured Si anodes, with shorter diffusion length and high surface-volume ratio facilitates effective diffusion and thus, the lithiation process is reaction-rate controlled [55], while in bulk Si, it is largely diffusion controlled at room temperature [56]. Moreover, the rate of Li diffusion is 1-2 magnitudes higher in a-Li_xSi as compared to crystalline Si (c-Si).

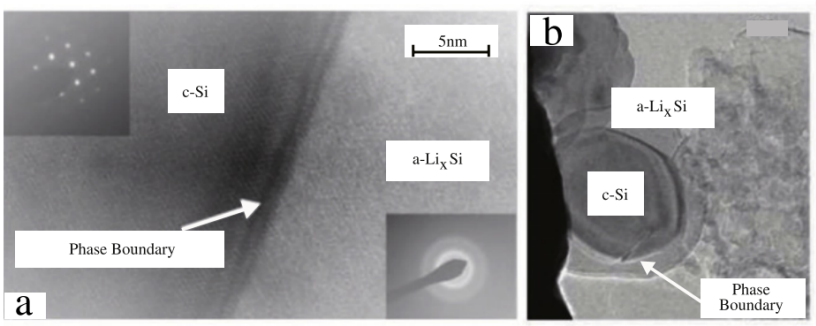

Figure 1.7: TEM images showing the formation a-Li_xSi layer during the lithiation of a) c-Si wafer and b) c-Si nanoparticle. In both the cases, a sharp phase boundary can be observed. Reprinted figure a) from Ref. [51]. Copyright 2011 by the American Physical Society. Figure b) adapted with permission from Ref. [57]. Copyright 2012 American Chemical Society.

In-situ Transmission Electron Microscopy TEM studies have revealed that above a certain size of Si nanoparticle, this interplay between reaction rate and Li diffusion results in concentration mismatch between the two phases leading to a stress induced fracture [57]. Conversely, the induced stress also affects the diffusion barrier, i.e. the application of a tensile (compressive) stress lowers (increases) the diffusion barrier as confirmed by theoretical calculations [58]. The effect of stress on diffusion partially explains the improved performance with kinked and curved Si NW [50, 59]. Most of these above-mentioned experimental and theoretical analysis are based on certain range of Li diffusivity values obtained from experiments or computations. Thus, it is important to have accurate diffusivity values of Li in bulk Si as well as in lithiated Li_xSi phases.

Li diffusion in bulk Si is well researched experimentally as well as theoretically establishing the migration of Li atom from one tetrahedral (T_d) interstitial to another via a hexagonal (H_x) position. The *ab-initio* computed value of the diffusion barrier for this jump is 0.60 eV [60], which is in good agreement with the experimental data of 0.655±0.01 eV [61]. However, the value for Li diffusivity in lithiated phases, for instance in LiSi, is still debated [62] owing to the slow kinetics of formation of LiSi phase. The reported values (experimental and theoretical) vary from 10^{-9} to 10^{-14} cm^2/sec spanning 5 orders of magnitude [62–66]. Such a large window of diffusivity values raises questions on the reliability of any model based on this data.

Computational methods provide an alternative way to calculate properties of materials which are difficult to synthesize at room temperature conditions. Empirical potentials are computationally faster but difficult to parametrize and are subjected to a restricted window of application. The *ab-initio* molecular dynamics (AIMD) simulations are accurate but often conducted at high temperatures to expedite diffusion and low temperature extrapolation might amplify the errors. Furthermore, the estimation of diffusion barrier from Mean-Squared Displacement (MSD) obtained from AIMD as well as from experimental data points at discrete temperature, use the Arrhenius relation of diffusivity. The Arrhenius equation relates the diffusion barrier ΔE_m as the exponential factor of the diffusion coefficient with a constant pre-factor D_0 [67]

$$D = D_0 \exp^{-\Delta E_m/kT} \tag{1.3}$$

This relation is a special case of a more general expression and holds true for most diffusing atoms at room temperature. It consists of temperature independent pre-factor and energy barrier using the classical harmonic approximation without taking into account quantum mechanical effects. At lower temperature or with relatively smaller diffusing atom than the host atom, the quantum effects become important, resulting in a significant deviation of diffusivity values from the Arrhenius behavior (H in Fe) [68, 69]. Li is also very small and quantum mechanical effects

lower its diffusivity values in graphite at room temperature by 30% as compared to the classical Arrhenius equation [70]. Such a calculation to estimate the quantum mechanical effects on Li diffusivity in Si has not yet been explored to the best of our knowledge. Moreover, as silicon shows anharmonic behavior at high temperature [71–73], its effect on Li diffusivity should also be studied to get a correct estimate of Li diffusivity values for a varied temperature range. In this thesis we first address these two problems and estimate the effect on Li diffusivity in Si and LiSi. Another important aspect we explored in this thesis is the delithiation process of Si based anodes and analyzing the delithiated Si structure that is summarized in the next section.

1.5 DELITHIATION OF SILICON-BASED ANODES

Lithiation of silicon-based anodes is well studied experimentally [14, 27] and theoretically [31, 74] as discussed in the previous section. However, the removal of Li atoms or delithiation is not yet fully understood, at least theoretically [37, 75]. For instance, Si lithiates via a two-step process but what is the delithiation mechanism? Is it diffusion controlled or reaction rate controlled? Crystalline silicon transforms to a-Si upon delithiation but does a-Si comes back to a structure similar to a-Si? How does the local environment of Si evolves as Li atoms are removed? Does Si retains the tetrahedral structure (4-fold coordination) upon delithiation?

Lithium insertion (lithiation) is thermodynamically favourable and thus easier to study computationally, at least by using AIMD techniques [54]. At variance delithiation is thermodynamically unfavourable and thus AIMD techniques can not be used to study delithiation unless an external potential is applied. One of the most commonly used method is the step-by-step Li removal followed by a volume reduction (associated to per Li atom) and relaxation of atomic positions at fixed volume [37, 75]. The volume reduction at each step (~14 $Å^3$) is the average volume occupied by a Li atom obtained experimentally [33]. Although this strategy provide a stable method, the assumption of

constant volume reduction at each Li atom removal might not be true, especially if Li atoms are coordinated differently. Moreover, this algorithm only allows volume scaling and no cell relaxation is allowed, while we know that silicon undergoes structural transformation upon lithiation/delithiation [31]. In this thesis we have proposed a modification in this method including complete cell relaxation followed by a few molecular dynamics (MD) steps to allow free structural evolution (Chapter 4). Furthermore, to gather statistics and analyze amorphous structure, we have used empirical potentials validated for Li-Si system in Chapter 5. Motivated by the method used in Ref. [76], a shell method has been adopted in studying delithiation that involves removing n Li atoms followed by a few MD time steps. This way we have tried to answer some of the above stated questions that will augment the understanding of delithiated silicon structures and guide in designing next-generation batteries.

The outline of the thesis is as follows:

- Chapter 2 recalls the fundamentals of Density Functional Theory used for ground state calculations and Density Functional Perturbation Theory used for phonon calculations. It also covers the basics of diffusion mechanisms, the Transition State Theory and the Kinetic Monte Carlo methods.

- Chapter 3 includes the calculation of Li diffusion coefficient in bulk Si and LiSi using the transition state theory. The effect of quantum tunneling effects, and anhamonicity has also been assessed for future applications.

- Chapter 4 covers the delithiation studies of lithiated Li_xSi phases by the means of first-principles calculations. The local environment of delithiated structures are analyzed by the Chemenv code within Pymatgen package.

- Chapter 5 outlines the validation of classical potential, which is used for studying large scale delithiation simulation.

2

THEORETICAL BACKGROUND

This chapter introduces the theoretical framework of first-principles methods that are used in the subsequent chapters for studying properties of silicon as an anode material. In Sec. 2.1.1 and Sec. 2.2, we briefly introduced the development of density functional theory (DFT) and its applicability to study the electronic structure of materials and computing their properties. In 2.3, the density-functional perturbation theory (DFPT) [77, 78] introduces the perturbative approach in DFT to calculate derivatives of the ground state energy for the computation of interatomic force constant, phonon frequencies, etc . Sec. 2.4 then introduces diffusion laws followed by the transition state theory framework for studying diffusion from first-principles. Subsequent approximations for the inclusion of quantum tunnelling effects and anharmonic effects are also discussed.

2.1.1 *Schrodinger equation*

The ground state of a system at equilibrium with N_n nuclei and N_e electrons can be completely described by its many-body wavefunction, Ψ^{MB} according to the time-independent Schrödinger equation.

$$H^{MB}(r, R)\Psi^{MB}(r, R) = E\Psi^{MB}(r, R) \tag{2.1}$$

where H^{MB} is the many-body Hamiltonian that can be written as:

$$H^{MB}(r, R) = T_n(R) + V_{nn}(R) + T_e(r) + V_{ee}(r) + V_{ie}(r, R) \tag{2.2}$$

where $T_n(R)$ and $V_{nn}(R)$ are the kinetic energy and the potential energy operators for nuclei. Similarly, $T_e(r)$ and $V_{ee}(r)$ denotes the kinetic and potential energy operators for electrons. The interaction between electrons and nuclei is denoted by $V_{ne}(r, R)$. The notation r and R is used as a shorthand representation for

the position coordinates of all the electrons (r_i, for $i = 1, 2, 3, ..., N_e$) and all the nuclei (R_α, for $\alpha = 1, 2, 3, ..., N_n$), respectively. The explicit definition of different operators appearing in Eq. 2.2 can be written as:

$$T_n(R) = -\sum_{\alpha} \frac{1}{2M_\alpha} \nabla^2_{R_\alpha} \tag{2.3}$$

$$V_{nn(R)} = \sum_{\alpha<\alpha'} \frac{Z_\alpha Z_{\alpha'}}{|R_\alpha - R_{\alpha'}|} \tag{2.4}$$

$$T_e(r) = -\sum_{i} \frac{1}{2} \nabla^2_{r_i} \tag{2.5}$$

$$V_{ee(r)} = \sum_{i<i'} \frac{1}{|r_i - r_{i'}|} \tag{2.6}$$

$$V_{ne(r,R)} = \sum_{i,\alpha} \frac{Z_\alpha}{|r_i - R_{\alpha'}|} \tag{2.7}$$

where M_α is the mass of atom α, and Z_α is the atomic mass number of nuclei α.

Given all these ingredients *a-priori*, the many-body Hamiltonian H^{MB} and the wavefunction Ψ^{MB}, in principle, can be determined and the corresponding ground-state energy (E) can be obtained from the eigenvalue problem in Eq. 2.1. However, in practice it is already difficult to obtain these many-body terms for He atom with only 2 electrons, without using any approximations. The complexity increases many fold with an increase in number of atoms and thus obtaining Ψ^{MB} or H^{MB} is nearly impossible. Thus, in the last few decades, researchers in this field have tried controlled approximations to the many-body Hamiltonian H^{MB} and wavefunction Ψ^{MB} for computing properties of interest in a reasonable computational time while keeping the desired accuracy and physical significance.

2.1.2 *Born-Oppenheimer approximation*

One of the first approximation that significantly reduce the complexity of the problem is by taking into account the heavy mass

of nuclei and thus their dynamics (T_{nn}) are comparatively much slower. Moreover, the nuclei-nuclei interaction (V_{nn}) is constant for a given set of atomic coordinates. Thus, for a given set of nuclear positions, their kinetic energy term $T_n(R)$ and the potential term $V_{nn}(R)$ can be dissociated from Eq. 2.2 and can be treated as a perturbation or as an external potential:

$$H(r, R) = H_e(r) + V_{ext}(R) \tag{2.8}$$

where

$$V_{ext}(R) = T_n(R) + V_{nn}(R) \tag{2.9}$$
$$H_e(r, R) = T_e(r) + V_{ee}(r) + V_{ne}(r, R) \tag{2.10}$$

It is the *Born-Oppenheimer* (BO) approximation [79], which reduces the problem to an electronic system. The information of nuclei are the parameters of the Hamiltonian in the form of an external potential experienced by the electrons. This is why, this field of physics is also called as *electronic structure theory*

The BO approximation is based on the instantaneous and adiabatic adaptation of the electronic density with the change in the positions of nuclei. This holds true for the ground state calculations of most solids at equilibrium and in this thesis, we will restrict ourselves within the realm of its applicability. Although BO approximation significantly simplifies the many-body problem, the remaining electronic Hamiltonian still contains electron-electron interaction terms, which are not trivial to compute for large systems with many electrons. Thus, further approximations are needed to transform this many-body problem to a simpler form, which led to the development of Density Functional Theory.

2.2 DENSITY FUNCTIONAL THEORY

Density Functional Theory (DFT) [80, 81] is currently the most widely used first-principles approach to compute material properties by studying their electronic structure. Over the decades the theory has developed rigourously. Consequently, its scope

has extended to compute advanced material properties from electron-phonon coupling, electronic excitations and anharmonic effects [82–84]. Moreover, the increase in computational resources, and the efficiency of DFT codes has made it possible to study systems of hundreds or thousands of atoms [85]. Though there is a tradeoff between accuracy and computational time and depending on the computed property, the balance has to be made to get the desired accuracy. This is where a thorough knowledge about the working of DFT is useful for adjusting the parameters. However, the description in this thesis will be limited to basic understanding of the theory and its relevant application to the scientific inquiry in subsequent chapters. More pedagogical reviews can be found in Ref. [77, 86, 87] and books by [80, 81, 88–91].

2.2.1 *Hohenberg and Kohn theorem*

The development of DFT was primarily motivated by the works of Hohenberg, Kohn and Sham [92, 93] that demonstrated the possibility to map the many-body wavefunction to a one-body electronic density for solving the Schrödinger equation. Although the original idea of using the electronic density was proposed by Thomas and Fermi [81], the Hohenberg and Kohn theorem [92] followed by Kohn-Sham scheme [93] provided the theoretical foundation for developing the framework.

For a system of N interacting particles with non-degenerate ground state, it is evident that there exists a unique ground state density $n_o(r)$ associated to the external potential $V_{ext}(r)$. In 1964, Hohenberg and Kohn [92] proved the opposite, which was not straightforward. They proposed two important theorems. The first theorem states that:

> **Theorem 1:** The ground state electronic density $n_o(r)$ of an interacting many-electron system can uniquely determine the external potential $V_{ext}(r)$, up to a constant.

This proved that the mapping from density to the external potential is unique. In other words, if there are two potentials V_{ext} and V'_{ext} that differs by more than a constant, they will always leads to two different ground state densities n and n'. Moreover, given a charge density $n(r)$, the external potential $V_{ext}(r)$ is fixed, and so in turn the Hamiltonian. Thus, the Hamiltonian as well as the other associated quantities (wavefunction, total energy, etc) can then be written as a functional of the density. Using this relation and applying the variational principles, the total energy and the ground state energy can then be written as:

$$E = \int V_{ext}(r)n(r)\,dr + \min_{\phi\to n}\left\{ \langle\phi|T_e + V_{ee}|\phi\rangle \right\} \tag{2.11}$$

> **Theorem 2:** The total energy of an interacting electron gas is a universal functional of its density, $E[n(r)]$, independent of $V_{ext}(r)$. The ground state is thus obtained by the wavefunction that minimizes this functional.

As the total energy is one of the observables and thus the above statement can be generalized for any observable to be defined as a universal functional of the density. These findings suggested a way to find the ground state of the electronic system by minimizing the energy functional:

$$E[n(r)] = \int V_{ext}(r)n(r)\,dr + F[n(r)] \tag{2.12}$$

under the constraint to yield the correct total number of electrons N_e. Hohenberg and Kohn proved the existence of a functional of the density $E[n]$ that defines the ground state. However its exact form was unknown untill Kohn and Sham demonstrated a practical way [93] and only after then DFT became useful to solve the Schrödinger equation.

2.2.2 *Kohn-Sham formulation*

In 1965, Kohn and Sham [93] proposed a scheme to approximate the unknown energy functional based on the energy of a non-interacting system of the same density n. The formulation is in the following context. Imagine a system of fictitious non-interacting electrons with the same ground state density as the interacting system. For such a non-interacting electronic system, the Schrödinger equation can be written as:

$$\left(-\frac{\nabla^2}{2} + V_{KS}(r)\right)\phi_n^{KS}(r) = \epsilon_n^{KS}\phi_n^{KS}(r) \tag{2.13}$$

using a basis set of single-particle orbitals, ϕ_n^{KS}. The corresponding electronic density can be written as:

$$n_{KS}(r) = \sum_n^{N_e} \left|\phi_n^{KS}(r)\right|^2 = n(r) \tag{2.14}$$

The first term in Eq. 2.13 is the kinetic energy operator of the non-interacting electron system, and the second term is the Kohn-Sham potential. Thus, given the exact Kohn-Sham potential, one can find the ground state of the non-interacting system which will give the same density as the interacting one, and by Hohenberg-Kohn theorem [92], the corresponding ground state. This maps the real system to the fictitious Kohn-Sham system, whose total energy can be written as:

$$E[n(r)] = T_{KS}[n(r)] + E_H[n(r)] + E_{ext}[n(r)] + E_{XC}[n(r)] \tag{2.15}$$

where,

$$T_{KS}[n(r)] = \sum_{n=1}^{N_e} \left\langle \phi_n^{KS} \middle| -\frac{1}{2}\nabla^2 \middle| \phi_n^{KS} \right\rangle \tag{2.16}$$

$$E_H[n(r)] = \frac{1}{2}\int n(r)V_H(r)dr = \frac{1}{2}\int \frac{n(r)n(r')}{|r-r'|}dr \tag{2.17}$$

are the kinetic and the potential energy functional or the Hartree functional of the Kohn-Sham system. These two terms can be computed exactly and the third term is the energy associated to the external potential:

$$E_{ext}[n(r)] = \int V_{ext}(r)n(r)dr \tag{2.18}$$

which is also fixed by fixing the n (from the first Hohenberg-Kohn theorem). Thus, the only unknown is the last term, the exchange-correlation energy functional $E_{XC}[n(r)]$ that contains the effect of all the many-body interactions in the interacting system. By definition, it includes the exchange interaction to obey Pauli's exclusion principle and the electron-electron correlation effect due to electrostatic repulsion.

From the second Hohenberg-Kohn theorem [92], the ground state of the Kohn-Sham system can be obtained by minimizing the energy functional. Thus applying the variational principle with a constraint to conserve the total number of electrons N_e yields:

$$\begin{aligned} &\frac{\delta}{\delta n(r)}\left[E[n(r)] - \lambda\left(\int n(r)dr - N_e\right)\right] = 0 \\ \implies &\frac{\delta E[n(r)]}{\delta n(r)} = \lambda \end{aligned} \tag{2.19}$$

where the parameter λ is the Lagrange multiplier for the constraint. Substituting expression of $E[n(r)]$ from Eq. 2.15 leads to:

$$\begin{aligned} &\frac{\delta T_{KS}[n(r)]}{\delta n(r)} + \frac{\delta E_H[n(r)]}{\delta n(r)} + \frac{\delta E_{ext}[n(r)]}{\delta n(r)} + \frac{\delta E_{XC}[n(r)]}{\delta n(r)} = \lambda \\ &\frac{\delta T_{KS}[n(r)]}{\delta n(r)} + V_{KS}(r) = \lambda \end{aligned} \tag{2.20}$$

Thus, the Kohn-Sham potential is defined as:

$$V_{KS}(r) = V_H(r) + V_{ext}(r) + V_{XC}(r) \tag{2.21}$$

where the first two terms are the Hartree potential and the external potential as defined earlier and the last term is the potential corresponding to the exchange-correlation energy $E_{XC}[n(r)]$:

$$V_{XC}(r) = \frac{\delta E_{XC}[n(r)]}{\delta n(r)} \tag{2.22}$$

Thus, given the exact form of $E_{XC}[n(r)]$, the Kohn-Sham potential V_{KS} is known and the corresponding charge density, which is linked to the Kohn-Sham orbitals providing a new Kohn-Sham potential. These equations must be solved by *self-consistent field* (SCF) cycles. The SCF cycles should be iterated until the n and V_{KS} are converged within a certain tolerance level to get the desired accuracy.

2.2.3 *Exchange-correlation energy*

The Kohn-Sham formulation thus presents a practical approach to define the ground state in exact form, except the value of $E_{XC}[n(r)]$ that require approximation. The accuracy of most of the DFT implementations rely significantly on the efficiency to approximate this exchange-correlation part. Thankfully, several good approximations have been proposed, however none is universal and one has to choose an appropriate one based on the tradeoff between the desired accuracy and the computational cost.

Amongst them, the most crudest one is the local-density approximation (LDA) [81], in which a) the density is assumed to vary slowly such that the exchange-correlation at any point r only depends on the local density $n(r)$ and b) which is equal to the exchange-correlation energy of a homogeneous electron gas of the same density $n(r)$, i.e.:

$$E_{xc}^{LDA}[n(r)] = \int n(r)\epsilon_{xc}^{hom.}(n(r))dr \tag{2.23}$$

To be more precise, the spatial variation of the electronic density can also be incorporated, which is known as the generalized

gradient approximation (GGA) [81]. The exchange-correlation energy can then be written as:

$$E_{xc}[n(r)] = \int n(r) f(n(r), \nabla n(r)) dr \tag{2.24}$$

Then there is meta-GGA approximation that also includes the second derivative of the kinetic energy density [94]. The hybrid functional family [95] mix a term of Hartree-Fock exchange term to better reproduce the electronic band gap of materials but at an additional computational cost. There are several other methods to approximate the exchange-correlation term, but we will restrict ourselves to LDA and GGA for the scope of this thesis as they work well for covalent and metallic solids.

Regarding the accuracy, LDA is generally known to underestimate the lattice parameters as it results in binding the atoms relatively tightly [81]. On the other hand, GGA tends to underbind and results in an overestimation of the lattice parameter. The selection of one thus, depends on the error in other physical quantities like bulk modulus, cohesive energy, vacancy formation energy, etc. With all the ingredients, the ground state can be obtained by minimizing the energy functional in Eq. 2.15 with respect to the Kohn-Sham orbitals using SCF iteration. There exists numerous methods to achieve faster convergence for SCF cycles and a detailed literature can be found in Ref. [96, 97].

2.2.4 *Structural relaxation*

DFT total energy calculations provide the ground state of the system with a pre-defined atomic positions, which is utilized by the BO approximation. However, often the equilibrium atomic positions (minima of the total energy with respect to the atomic positions) are required to compute physical properties like cohesive energy, bond length, lattice parameter, etc [81, 98]. The minima can be obtained by geometry optimization (cell and the internal degrees of freedom of atoms) based on the forces and stresses computed by the Hellman-Feynman theorem [99] and the stress theorem [100], respectively.

According to the Hellman-Feynman theorem, the force on an atom κ in the direction α is related to the derivative of the total energy with respect to the displacement in that direction $R_{\kappa\alpha}$:

$$F_{\kappa\alpha} = \frac{\partial E_{tot}}{\partial R_{\kappa\alpha}} = \left\langle \Psi \middle| \frac{\partial H}{\partial R_{\kappa\alpha}} \middle| \Psi \right\rangle \tag{2.25}$$

Accordingly, the stress tensor $\sigma_{\alpha\beta}$ in the direction α upon the surface β can be written as the first derivative of the total energy with respect to the the corresponding macroscopic strain in that direction:

$$\sigma_{\alpha\beta} = \frac{1}{\Omega_0} \frac{\partial E_{tot}}{\partial \epsilon_{\alpha\beta}} = \left\langle \Psi \middle| \frac{\partial H}{\partial \epsilon_{\alpha\beta}} \middle| \Psi \right\rangle \tag{2.26}$$

Based on these forces and stresses, the energy minima can be obtained by a minimization scheme such as Broyden-Fletcher-Goldfarb-Shanno (BFGS) or Low memory BFGS (L-BFGS) [101]. Both these methods are quasi-newton methods targeted to solve non-linear optimization problems. The former is one of the most commonly used technique for structural relaxation, while the latter is a modified version of BFGS that uses less memory and often reach faster convergence, especially for large systems. The key difference is that unlike BFGS, L-BFGS remove old gradients after some iterations to leave more space for freshly computed gradients. This solves the problem of the memory, and it avoids the bias towards the initial gradient.

2.3 DENSITY FUNCTIONAL PERTURBATION THEORY

So far we have discussed the ground state calculations within DFT formalism and obtaining material properties from total energy (forces and stresses). Similar to the calculation of forces as a first derivative of total energy, the response of the system to a small perturbation can be studied formally by applying the perturbation theory within the DFT framework. This is known as the density functional perturbation theory (DFPT).

2.3.1 *Introduction*

The response of the system to perturbations of different order can provide useful material properties that are directly related to the successive derivatives of the total energy with respect to these perturbations. Material properties like the dielectric tensor and phonon frequencies harnessed using this method are in good agreement with the experimental data and thus became a standard technique in this domain [78, 102, 103]. In the next subsections, the basics of DFPT formalism will be presented, followed by the computation of the interatomic force constants and phonon frequencies.

2.3.2 *Response functions*

The successive derivatives of the total energy can be obtained either by the finite difference method using frozen phonon approach or using a perturbative approach like DFPT. The former method uses only the ground state calculations but several of them, with varying amplitude of collective displacements are needed, to obtain a good numerical accuracy. Moreover, this approach can not incorporate incommensurate perturbations or perturbations due to a homogeneous electric field and is restricted to a small cell size [103]. Thus one prefers to use DFPT, which is used in this work as well to compute material properties.

Let us consider a small perturbing potential $V_{ext}(\lambda)$ characterized by a dimensionless parameter λ that can take any value between 0 (no perturbation) and 1 (full perturbation). Using the perturbation theory, if the perturbation $\lambda \ll 1$, the external potential and thus all observables can be written as a perturbation series:

$$V_{ext}(\lambda) = V_{ext}^{(0)} + \lambda V_{ext}^{(1)} + \lambda^2 V_{ext}^{(2)} + ... \tag{2.27}$$

where the expansion coefficient can be written as:

$$V_{ext}^{n} = \frac{1}{n!} \frac{d^n V_{ext}}{d\lambda^n} \bigg|_{\lambda=0} \tag{2.28}$$

Thus, the change in the eigen states and eigen energies due to a perturbation in the Hamiltonian

$$H(\lambda) = H^{(0)} + \lambda H^{(1)} + \lambda^2 H^{(2)} + ... \tag{2.29}$$

can be written as:

$$\phi_i(\lambda) = \phi_i^{(0)} + \lambda \phi_i^{(1)} + \lambda^2 \phi_i^{(2)} + ... \tag{2.30}$$

$$E_i(\lambda) = E_i^{(0)} + \lambda E_i^{(1)} + \lambda^2 E_i^{(2)} + ... \tag{2.31}$$

The goal is to express the eigen energies and wavefunctions of the perturbed Hamiltonian in terms of those of the old unperturbed ones. The new perturbed Hamiltonian $H^{(o)}$ can then be written as:

$$H(\lambda) = H^{(0)} + V_{ext}(\lambda) \tag{2.32}$$

and the corresponding revised Schrödinger equation for the perturbed Hamiltonian is:

$$\begin{aligned} H(\lambda) \left|\phi_i^{(0)}\right\rangle &= E_i(\lambda) \left|\phi_i^{(0)}(\lambda)\right\rangle \\ [H(\lambda) - E_i(\lambda)] \left|\phi_i^{(0)}(\lambda)\right\rangle &= 0 \end{aligned} \tag{2.33}$$

which has to be solved with the orthonormalization constraint for the wavefunctions

$$\left\langle \phi_i^{(0)}(\lambda) \middle| \phi_i^{(0)}(\lambda) \right\rangle = 1 \tag{2.34}$$

The variable λ is supressed for brevity of equations, however the quantities still have explicit dependency on λ. Expanding the

first-order derivative of Eq. 2.33 and Eq. 2.34 results in Sternheimer equation

$$[H - E_i]^{(0)} \left|\phi_i^{(1)}\right\rangle + [H - E_i]^{(1)} \left|\phi_i^{(0)}\right\rangle = 0 \tag{2.35}$$

and the corresponding orthonomal constraint, respectively

$$\left\langle \phi_i^{(0)} \middle| \phi_i^{(1)} \right\rangle + \left\langle \phi_i^{(1)} \middle| \phi_i^{(0)} \right\rangle = 0 \tag{2.36}$$

The first-order Hamiltonian is the derivative of the operators, which are supposed to be known. The aim is to calculate the first-order wavefunction and the corresponding eigenenergies. Out of which, the latter can be obtained by projecting the Sternheimer equation (Eq. 2.35) in the subspace spaneed by the basis set $\left\langle \phi_i^{(0)} \right|$

$$\left\langle \phi_i^{(0)} \right| [H - E_i]^{(0)} \left|\phi_i^{(1)}\right\rangle + \left\langle \phi_i^{(0)} \right| [H - E_i]^{(1)} \left|\phi_i^{(0)}\right\rangle = 0 \tag{2.37}$$

Using the relation in Eq. 2.33, the first term of Eq. 2.37 vanishes and rearranging the second term gives the first-order eigenenergy

$$E_i^{(1)} = \left\langle \phi^{(0)} \middle| H^{(1)} \middle| \phi^{(0)} \right\rangle \tag{2.38}$$

This result is also the Hellmann-Feynman theorem [99] as derived earlier. Similarly, the second-order eigenenergy can be written as [102]:

$$\begin{aligned} E_i^{(2)} = \left\langle \phi^{(1)} \right| H^{(1)} \left|\phi^{(0)}\right\rangle + 2 \left\langle \phi^{(1)} \right| [H - E_i]^{(0)} \left|\phi^{(1)}\right\rangle \\ + \left\langle \phi^{(0)} \right| H^{(1)} \left|\phi^{(1)}\right\rangle + \left\langle \phi^{(0)} \right| H^{(2)} \left|\phi^{(0)}\right\rangle \end{aligned} \tag{2.39}$$

Note that in the above equation, only the zeroth-order and the first-order wavefunctions are required to calculate the second-order derivative of the total energy. The former is known from the Kohn-Sham-based DFT approach and the latter can be obtained from the self-consistent Sternheimer equation (Eq. 2.35).

Eq. 2.38 and 2.39 can be used to compute the dynamical matrix, the interatomic force constant, and phonon frequencies as described in the subsequent section. However, the description is limited to understand the calculations in the subsequent chapters of the thesis, for more details the reader can refer the appropriate literature [104–108].

2.3.3 *Interatomic force constants and phonon frequencies*

The total energy of a periodic system with a small perturbation can be expanded around its ground-state configuration in terms of atomic displacements [105]:

$$E_{tot}(\tau) = E_{tot}^{(0)} + \frac{1}{2}\sum_{\kappa\alpha,a}\sum_{\kappa'\beta,b}\frac{\partial^2 E_{tot}}{\partial R^a_{\kappa\alpha}\partial R^b_{\kappa'\beta}}\tau_{\kappa\alpha,a}\tau_{\kappa'\beta,b} + \ldots \tag{2.40}$$

where $\tau^a_{\kappa\alpha}$ is the displacement of atom κ along the direction α from its equilibrium position in the cell labeled as a (with coordinates R^a). Within harmonic approximation, the higher-order terms can be neglected. The derivative term is the interatomic force constant (IFC) between the atom κ in cell a and the atom $\kappa^{'}$ in cell b defined as:

$$C_{\kappa\alpha,\kappa'\beta}(a,b) = \left(\frac{\partial^2 E_{tot}}{\partial R^a_{\kappa\alpha}\partial R^b_{\kappa'\beta}}\right) \tag{2.41}$$

Assuming the translational invariance, the fourier transform of the IFC in the reciprocal (q) space can be written as:

$$\tilde{C}_{\kappa\alpha,\kappa'\beta}(q) = \sum_b C_{\kappa\alpha,\kappa'\beta}(0,b)e^{iq.R_b} \tag{2.42}$$

which is related to the dynamical matrix $\tilde{D}_{\kappa\alpha,\kappa'\beta}(q)$ as:

$$\tilde{D}_{\kappa\alpha,\kappa'\beta}(q) = \frac{\tilde{C}_{\kappa\alpha,\kappa'\beta}(q)}{\sqrt{M_\kappa M_{\kappa'}}} \tag{2.43}$$

The phonon frequencies can be obtained as solutions of the eigenvalue problem for the restoring force acting on an atom κ in a periodic cell a when is displaced $\tau_{\kappa\alpha}$ from its equilibrium position:

$$M_\kappa \frac{\partial^2 \tau^a_{\kappa\alpha}}{\partial t^2} = -\sum_{\kappa'\beta,b} C_{\kappa\alpha,\kappa'\beta}(a,b)\tau^b_{\kappa'\beta} \tag{2.44}$$

where M_κ is the mass of atom κ. Note that the displacement of atom κ in cell a is coupled with the displacement of atom κ' in cell b. For a periodic structure, the displacement can be written as a periodic oscillation in both time and space around the equilibrium position. The previous equation can then be written as:

$$\begin{aligned} M_\kappa \omega^2_{mq} U_{\kappa\alpha}(mq) e^{iq.R_a} &= \sum_{\kappa'\beta,b} C_{\kappa\alpha,\kappa'\beta}(a,b) U_{\kappa'\beta}(mq) e^{iq.R_b} \\ &= e^{iq.R_a} \sum_{\kappa'\beta} \tilde{C}_{\kappa\alpha,\kappa'\beta}(q) U_{\kappa'\beta}(mq) \end{aligned} \tag{2.45}$$

where ω_{mq} is the phonon frequency of mode m at point q and $U_{\kappa\alpha}(mq)$ is the corresponding amplitude of oscillation. Every atom has 3 such equations of motion, one for each Cartesian direction, i.e. a total of $3\times N_{atoms}$. This eigenvalue problem relates the spectrum of phonon frequencies to the IFC, which can be computed from the derivative of total energy as shown in Eq. 2.41. Once the IFC are computed then the phonon frequencies and amplitudes are simply the eigenvalues and the corresponding eigenvectors of the problem.

According to the acoustic sum rule (ASR), the crsytal energy is invariant under any global translation of the whole crystal, i.e.

$$\sum_{\kappa'\beta} \tilde{C}_{\kappa\alpha,\kappa'\beta}(q=0) = 0 \tag{2.46}$$

which suggests that 3 (acoustic) phonon modes (one for each Cartesian direction) have zero frequency at the zone center ($q =$

0). However, due to the use of real space grid for calculating the exchange-correlation energy, the acoustic modes are not exactly zero at $q = 0$ in computations. Thus in order to restore the ASR, all the phonon modes are corrected as:

$$\tilde{C}^{new}_{\kappa\alpha,\kappa'\beta}(q) = \tilde{C}_{\kappa\alpha,\kappa'\beta}(q) - \delta_{\kappa\kappa'} \sum_{\kappa''} \tilde{C}_{\kappa\alpha,\kappa''\beta}(q = 0) \tag{2.47}$$

Phonon frequencies can be used for material characterization (phonon frequencies can be obtained experimentally by Raman spectroscopy, inelastic neutron scattering and infrared measurements) as well as for computing their electrical and mechanical properties. In the next section, we will see how we can use phonon frequencies to compute the jump rate of a diffusing atom in a host lattice.

2.4 DIFFUSION

Up to this point, we have developed a sufficient understanding for studying the dynamics of electrons with respect to fixed nuclei positions by solving Kohn-Sham equations. The response of this system due to small perturbations in the nuclear positions owing to the external potential or an electric field can be studied by DFPT. This understanding has enabled us to calculate microscopic properties of anode materials like lattice parameters, Gibbs free energy, defect formation energy, and relate it to macroscopic properties like bulk modulus, specific heat, etc [81, 88]. Another important macroscopic property of an anode material is the rate of transfer (diffusion) of Li ions during charging and discharging of the battery [12, 14]. In this subsection, we will discuss how we can use electronic structure calculations to study diffusion.

2.4.1 *Introduction*

Diffusion plays a fundamental role in numerous materials science phenomena like phase transformations, nucleation and growth

kinetics, rate of chemical reactions, intermixing of phases, etc. The understanding of diffusion mechanism helps in designing materials for technological advancement for wide-ranging applications. Non-exhaustively, in designing better electrodes and electrolytes for batteries and fuel cells, in controlled hardening of steel by carburization process, in doping of semiconductors, in designing containers for nuclear waste, and also in clinical therapy such as diffusion magnetic resonance imaging (MRI) and studying atmospheric pollution [67]. Therefore, diffusion has been studied extensively from both experimental and theoretical points of view in various fields [62, 109–112]. In this thesis we will restrict the discussion related to atomic diffusion for understanding Li diffusion in Si and lithiated Li_xSi alloys.

The structure of this section is as follows: Sec. 2.4.2 discusses the driving force for diffusion followed by Sec. 2.4.3 briefly summarizing basic concepts of diffusion. Sec. 2.4.4 introduces the transition state theory (TST) followed by Sec. 2.4.5 outlining the quantum mechanical effects within the TST framework to study diffusion. Finally, Sec. 2.4.6 delineates methods to study the validation of harmonic approximation and including anharmonic effects in the diffusion coefficient.

2.4.2 *Driving force for diffusion*

The main driving force for diffusion follows from the extremum principle of Lagrangian formalism to minimize the Gibbs free energy. If we consider atomic diffusion, atoms diffuse in order to minimize the overall Gibbs free energy resulting in the change of concentration gradient. However, the minimization of Gibbs free energy and the resulting transfer of atoms do not always follow minimization of concentration gradient [113]. It can be explained in the following context.

Let us consider two blocks from the same solid solution A-B but with different concentrations that are joined together as illustrated in Fig. 2.1 a). The molar free energy curve of the system is as shown in Fig. 2.1 b). If the Gibbs free energy of the two blocks before mixing is represented by G_1 and G_2, then the initial Gibbs

free energy of the welded piece will be represented by point G_3 on the line joining G_1 and G_2. The position of G_3 on this line is defined by lever rule based on the composition of two pieces. Now, the joined piece is held at sufficiently high temperature to allow long-range diffusion across the two blocks. Thus, in order to minimize the Gibbs free energy, the minima G_4 is reached resulting in diffusion of atoms from region of higher concentration to that of lower concentration. However, this is not always the case.

Now, lets consider a similar situation but with the molar free energy curve having a miscibility gap as illustrated in Fig. 2.1 d). In this case, the atoms diffuse towards the region of high concentration but still decreasing the Gibbs free energy to G_4. Due to the miscibility gap, the curvature is negatve at points G_1 and G_2, which drives the atoms towards region of higher concentration to minimize the overall Gibbs free energy. Such transfer of atoms against the concentration gradient is known as *"up-hill"* diffusion.

Instead of concentration gradient, if we consider chemical potential as illustrated in Fig. 2.1 e) and f), the understanding is much clear. For both the cases, atoms diffuse from the region of higher chemical potential to that of lower chemical potential. Thus, chemical potential gradient is more accurate to represent as a driving force for diffusion. However, the miscibility gap can vanish at the high temperature and often the former *"down-hill"* diffusion case is encountered. Moreover, measuring concentration gradient is easier than measuring chemical potential. Thus, it is more convenient to relate diffusion process with concentration gradient. In the following subsections we will assume this approach though one should keep in mind this intricacy while studying diffusion. Moreover, as we proceed we will see that at atomic level we will redefine the driving force for diffusion. The following subsections briefly introduce the basic equations of diffusion.

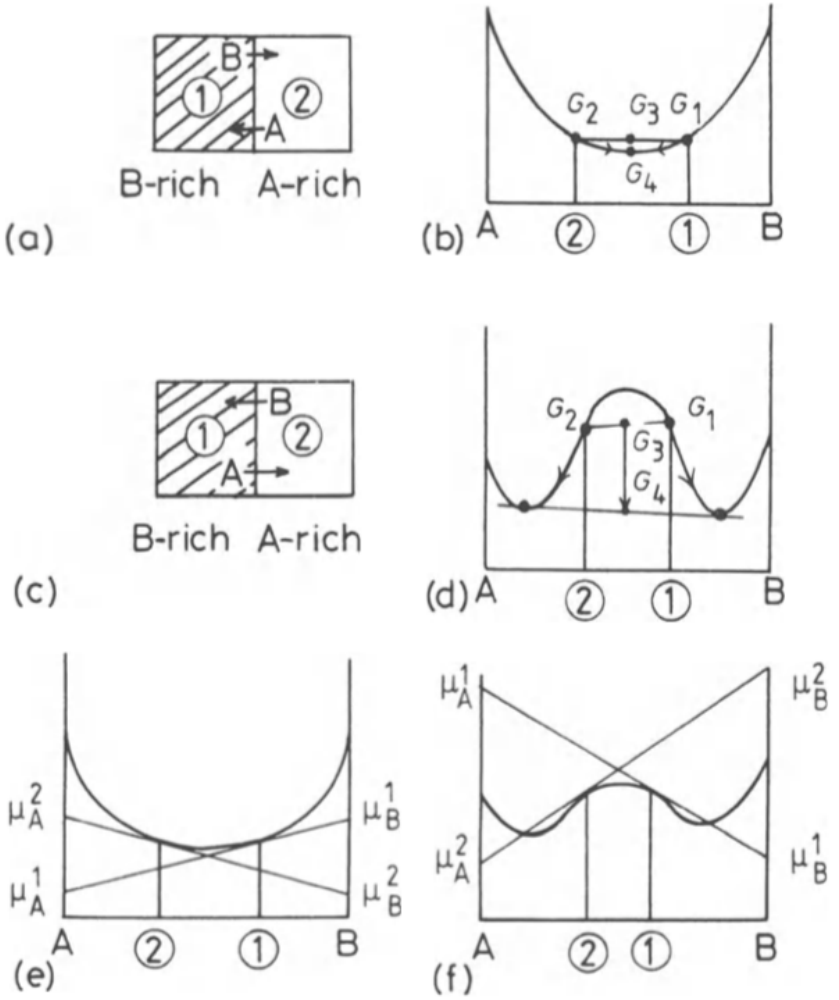

Figure 2.1: Gibbs free energy change (b) and (d) for “down-hill" diffusion (a) and “up-hill" diffusion (c), respectively. Corresponding chemical potential change are represented in (e) and (f). Reproduced with permission of Taylor &; Francis Group LLC - Books from Ref. [113]. Copyright 2008; permission conveyed through Copyright Clearance Center, Inc.

2.4.3 *Fundamental concepts of diffusion*

In this subsection, we will briefly introduce some fundamentals of diffusion followed by theoretical framework to study atomic diffusion from quantities obtained from first-principles calcu-

lations. These fundamental concepts are largely based on the books mentioned in Ref. [67, 113].

Diffusion processes are governed by a set of empirical laws deduced by Adolf Fick in 1855 and are known as Fick's laws [67]. Though these laws are purely phenomenological, numerous fundamental diffusion studies have not violated their validity till date.

Fick's first law

Fick introduced the concept of diffusion of particles (atoms, ions or molecules) based on the concentration gradient. In an isotropic medium, the diffusion flux can be written as:

$$\begin{aligned} J &\propto \nabla C \\ &= -D\nabla C \end{aligned} \tag{2.48}$$

where ∇C is the concentration gradient vector and the proportionality factor, D, is called the *diffusion coefficient* or the *diffusivity* of the particle in the medium. Fick's first law follows a similar intuition discussed in Sec. 2.4.2 that the flow of flux is directly proportional to the concentration gradient and the $-$ sign suggests that the direction of flux is from higher to lower concentration.

Equation of continuity

Generally, the total number of diffusing particles are fixed or conserved. For such a diffusion process obeying the conservation law, the total amount of flux coming inside a test volume ($\Delta x \Delta y \Delta z$) is equal to the amount of flux going out

$$J_{out} - J_{in} = \text{net accumulation or loss} \tag{2.49}$$

Expanding flux J with Taylor expansion for the infinitesimal volume ($\Delta x \Delta y \Delta z$)

$$-\left(\frac{\partial J}{\partial x} + \frac{\partial J}{\partial y} + \frac{\partial J}{\partial z}\right)\Delta x \Delta y \Delta z = \frac{\partial C}{\partial t}\Delta x \Delta y \Delta z$$
$$-\boldsymbol{\nabla} \cdot J = \frac{\partial C}{\partial t} \tag{2.50}$$

where the accumulation or loss of particles is denoted by the rate of change of concentration multiplied by the infinitesimal volume. Eq. 2.50 is the *continuity equation.*

Fick's second law

Applying the Fick's first law (refer Eq. 2.48) in the continuity equation yields the Fick's *second law*

$$\frac{\partial C}{\partial t} = \boldsymbol{\nabla} \cdot (D \boldsymbol{\nabla} C) \tag{2.51}$$

which is a non-linear partial differential equation (PDE). If there is a composition dependency on the diffusion coefficient, this equation holds and thus can not be solved analytically. However, if there is no explicit concentration dependency on the diffusion coefficient, which is the case with tracer diffusion or in solid state diffusion, D can be taken out of the divergence.

$$\frac{\partial C}{\partial t} = D \nabla^2 C \tag{2.52}$$

Note that the revised equation is a linear PDE and given the initial and boundary conditions, can be solved analytically. For detailed review on solutions of PDE in diffusion, refer the diffusion textbook by Mehrer [67]. As Fick's laws were deduced phenomenologically, it is interesting to understand their validity while studying diffusion from atomistic level that is covered in the subsequent subsections.

Atomic diffusion mechanisms

Based on the type of position occupied by the diffusing atom, there are two main diffusion mechanisms involved in atomic diffusion, namely interstitial diffusion and substitutional diffusion. Substitutional diffusion often occurs via vacancy mechanism whereas interstitial diffusion involves migration of interstitial atom between larger atoms. The latter is observed when the diffusing specie is much smaller in size than the host atoms. There are other diffusion mechanism such as divancy mechanism, ring diffusion, direct exchange mechanism, however for the relevance of this thesis we will restrict ourselves to these two types of diffusion mechanisms.

In substitutional diffusion, the substitutional atom usually oscillates about a given site surrounded by neighboring atoms. In case of vacancy diffusion, the substitutional atom jumps to the next available vacant site (assuming vacancy diffusion). Thus, the rate of migration depends on the rate at which it encounters a vacancy, which is directly related to the vacancy concentration.

Interstitial diffusion occurs when the solute atom is much smaller in size than the solvent atom and prefers to occupy one of the interstitial void as the most stable site. In face-centered cubic (FCC) and body-centered cubic (BCC), octahedral and tetrahedral voids are the prominent sites to occupy [67]. The interstitial atom can migrate through the gaps between the host atoms. Often the interstitial concentration is low such that an interstitial atom is always surrounded by vacant interstitial sites to which it can jump, provided it has sufficient vibrational energy to overcome the energy barrier. Having understood the basic mechanism of these two types of diffusion, let us derive the rate equations and see what ingredients can be calculated from electronic structure calculations.

Random-walk theory

At the microscopic level, diffusion occurs through Brownian motion. This phenomenon was observed by the Scottish Botanist Robert Brown in 1827, even before Fick introduced Fick's laws

of diffusion. He studied this phenomenon in the motion of granules from pollen in water. This line of thought gave way to the development of Random-walk theory in diffusion when Einstein and Smoluchowski, independently, came up with a relation between mean displacement of particles and the diffusion coefficient.

According to random-walk theory for diffusion in solids, the diffusing atom randomly jump to the next available site depending on the type of diffusion. These small elementary jumps results in the long range diffusion at the macroscopic level. These jumps are usually very rapid as compared to the average residence time of an atom on a lattice site and thus depends on two factors:

1. The frequency of such jumps that relates physical properties like jump distance, jump rate, available jump sites, etc.

2. Individual jump process and energy barrier

Let us consider a simplified model of an interstitial jump in a cubic lattice for understanding the concepts. The formalism remains the same for vacancy diffusion and/or any other lattice type. Imagine a cubic lattice with a low concentration of interstitial atoms and they jump randomly to the next available interstitial site. Considering one such jump of atoms from the atomic plane 1 to 2 with a jump distance of λ, the net flux in the absence of any other driving force can be written as:

$$J = \tau n_1 - \tau n_2 \tag{2.53}$$

where τ is the jump rate (number of jumps per unit time) and n_1 and n_2 are the number of interstitials per unit area in plane 1 and 2, respectively. Note that in the absence of a driving force, the forward and backward jump can happen with equal probability or in other words the same jump rate τ. Writing n_1 and n_2 in terms of concentration gradient, we get:

$$n_1 - n_2 = \lambda(C_1 - C_2) \tag{2.54}$$

Assuming a slow change of concentration gradient with respect to distance x in terms of interatomic distance, it can be expanded with Taylor expansion as:

$$C_2 = C_1 + \lambda \frac{\partial C}{\partial x} \tag{2.55}$$

Substituting Eq. 2.54 and 2.55 in Eq. 2.53 gives:

$$J = -\lambda^2 \tau \frac{\partial C}{\partial x} \tag{2.56}$$

and by comparing from Fick's first law, the diffusion coefficient is:

$$D = \lambda^2 \tau \tag{2.57}$$

However, this relation is just for one-dimensional diffusion along the x axis on a cubic lattice. In the following subsections we will generalize this relation for any type of lattice with different coordination numbers.

Einstein-Smoluchowski relation

Following the approach of random-walk theory, the change in the concentration gradient can also be expanded with respect to time. Expanding the change in the concentration with respect to a small time δt up to the second derivative gives [67]:

$$\frac{\partial C}{\partial t} = \frac{\langle R \rangle}{\delta t} \frac{\partial C}{\partial r} + \frac{\langle R^2 \rangle}{6\delta t} \frac{\partial^2 C}{\partial r^2} \tag{2.58}$$

In the above equation, $\langle R \rangle$ is the mean displacement of the diffusing atom and $\langle R^2 \rangle$ is the mean-squared displacement. The first term corresponds to the change in concentration due to an external driving force or drift. In the absence of this driving force, first term can be dropped and the Fick's second law is reproduced

$$D = \frac{\langle R^2 \rangle}{6\delta t} \tag{2.59}$$

In 1905 Einstein and Smoluchowski, independently, derived this equation at the same time and is commonly known as *Einstein-Smoluchowski* relation [67]. This relation is often used in molecular dynamics study to calculate the diffusion coefficient of a particle from the mean-squared displacement of its trajectory.

According to the random-walk theory, the diffusing atom on a lattice can have discrete diffusion steps and thus the mean-squared displacement can be written as:

$$\langle R^2 \rangle = \langle n \rangle d^2 \tag{2.60}$$

where $\langle n \rangle$ is the mean number of jumps with a jump length of d. For such a lattice jump with z possible jump sites, the jump rate can be defined as

$$\tau = \frac{\langle n \rangle}{z\bar{\tau}} = \frac{\langle R^2 \rangle}{d^2 z\bar{\tau}} \tag{2.61}$$

Substituting Eq. 2.61 in Eq. 2.59 yields the diffusion coefficient as:

$$D = \frac{1}{6} z d^2 \tau \tag{2.62}$$

which directly relates diffusivity to the jump rate τ, which can be computed by the transition state theory (TST) as explained in the next section.

2.4.4 *Classical transition state theory*

The TST framework was developed simultaneously by Eyring [114] and by Evans and Polanyi [115] that relates the reaction rate of a reaction in terms of the free energy change. According to TST, the jump rate can be written as:

$$\tau = \frac{kT}{h} e^{-\Delta F/kT} \tag{2.63}$$

where ΔF is the change in the free energy between the initial state and the transition state of a reaction at a given temperature

T. Other variables are the Boltzmann constant k and the Plank's constant $\hbar$. Similarly, the diffusing atom jumps from one stable position to another stable position via a transition state and the rate of this jump can thus be written in terms of the free energy difference between the initial and the transition state.

From thermodynamic relation, the change in the free energy can be written as:

$$\Delta F = \Delta U - T\Delta S \tag{2.64}$$

where ΔU and ΔS are the free energy change and the entropy change, respectively. Going forward in this thesis, the energy difference in terms of diffusion always refer to the difference between the initial state and the transition state, unless stated otherwise. The free energy can be expressed in terms of the partition function $Z(T)$, using Boltzmann statistics [98]

$$F(T) = -kT \ln Z(T) \tag{2.65}$$

$$\tag{2.66}$$

Employing the classical expression of partition function within the harmonic approximation for the lattice vibrations [98]:

$$\begin{aligned} Z(T) &= e^{-E_0/kt} \sum_i e^{-E_i/kT} \\ &= e^{-E_0/kt} \sum_{i=1} e^{-h\nu_i/kT} \end{aligned} \tag{2.67}$$

The total free energy including the ground-state energy E_0 of the static lattice where atoms are in their mean position can then be written as:

$$F_C(T) = E_0 + kT \ln \left(\prod_{i=1} \frac{h\nu_i}{kT} \right) \tag{2.68}$$

$$\Rightarrow \Delta F_C(T) = \Delta E + kT \ln \left(\frac{\prod_{i=1}^{N-1} \frac{h\nu_i^S}{kT}}{\prod_{i=1}^{N} \frac{h\nu_i^0}{kT}} \right) \tag{2.69}$$

where ν_i is the vibrational frequency of the ith mode with $h\nu_i$ being the quantum of energy of the harmonic oscillator. The superscripts S and 0 denote the initial point and the saddle point, respectively, while the subscript Q and C represent the quantum and classical expression, respectively. The summation in the saddle point case runs only till $N-1$ because there is one degree of freedom less corresponding to the imaginary frequency associated with the negative curvature at the saddle point [98]. The first term is the ground-state energy difference between the initial point and the saddle point configuration (migration energy barrier) and the second term is the vibrational free energy, i.e.

$$\Delta F_C^{vib}(T) = kT \ln \left\{ \frac{\prod_{i=1}^{N-1} \left(\frac{h\nu_i^S}{kT}\right)}{\prod_{i=1}^{N} \left(\frac{h\nu_i^0}{kT}\right)} \right\} \tag{2.70}$$

Then the vibrational entropy (phonon entropy) difference can be calculated by differentiating Eq. 2.70 with respect to T:

$$\begin{aligned} \Delta S &= -\frac{\partial \Delta F}{\partial T} \\ \Rightarrow \Delta S_C^{vib} &= -k \ln \left[\frac{kT}{h} \frac{\prod_{i=1}^{N-1} \nu_i^S}{\prod_{i=1}^{N} \nu_i^0} \right] - k \end{aligned} \tag{2.71}$$

Substituting Eq. 2.69 in Eq. 2.63, yields the jump rate as:

$$\tau_C = \frac{\prod_{i=1}^{N} \nu_i^0}{\prod_{i=1}^{N-1} \nu_i^S} e^{-\Delta E/kT} \tag{2.72}$$

which when substituted to Eq. 2.62 provides the diffusivity value as:

$$D_C = \frac{1}{6} z d^2 \frac{\prod_{i=1}^{N} \nu_i^0}{\prod_{i=1}^{N-1} \nu_i^S} e^{-\Delta E/kT} \tag{2.73}$$

This diffusivity relation was derived thanks to the TST framework. However before the development of TST, a similar expres-

sion has been derived empirically that follows Arrhenius equation and can be written as:

$$D_{Arr} = D_0 e^{-\Delta E_m / kT} \tag{2.74}$$

where D_0 is the pre-exponential factor or simply prefactor and E_m is the migration energy barrier. Since it was developed empirically, the physical meaning of D_0 and E_m remained unclear until the development of TST that provided the physical meaning to these parameters. Comparing Eq. 2.74 to Eq. 2.84, the parameters reads as:

$$D_0 = \frac{1}{6} z d^2 \frac{\prod_{i=1}^{N} \nu_i^0}{\prod_{i=1}^{N-1} \nu_i^S} \tag{2.75}$$

$$\Delta E_m = \Delta E \tag{2.76}$$

As there is no explicit temperature dependence in either of these parameters, the natural logarithm of diffusivity goes linearly with the inverse of the temperature as per the Arrhenius law.

All the ingredients of Eq. 2.84 can be computed from first-principles-based DFT calculations. Phonon frequencies can be computed within the DFPT framework as shown in the previous section and the energy barrier ΔE can be computed by finding the minimum energy path (MEP) for the diffusing atom. This can be obtained either by the nudged elastic band (NEB) method [116] or by the climbing image NEB (CI-NEB) method [117], provided the initial and final points are known *a-priori*.

Given an arbitrary number of images between the initial and the final point configuration, the NEB method obtains the MEP by optimizing these intermediate images while maintaining equal spacing between the images. This constrained optimization is performed by using a spring constant along the band connecting images and by projecting out the normal component of the force due to the potential. Each image is thus relaxed to its lowest energy state by moving perpendicular on the band while maintaining equal distance. The accuracy of this method relies on the number of images required to mimic the MEP within a certain level of accuracy, which can be very large for some

cases depending on the potential energy surface and the jump distance.

The CI-NEB method can partially overcome this limitation of NEB method to obtain the exact saddle point. In order to find an accurate MEP, one must increase the number of intermediate images. However, most of the time, we are interested in finding the saddle point configuration and not the whole MEP (as in the present case for calculating ΔE). In CI-NEB, the tangential component of the force on the highest energy image is inverted and cancel the spring force. Thus the highest energy image climbs to the top of the energy barrier while relaxing in other directions, unless it reaches the maximum where the tangential force is zero. The modification to climb the highest energy image to the top of the barrier gave this method the name, climbing-image NEB.

This description of diffusivity is based on the classical expression of the partition function within the TST framework that reproduces the Arrhenius behavior. The quantum mechanical definition of the partition function uses the same ingredient but incorporates the effect of zero-point motion and is valid over a larger temperature range, which we will see in the next subsection. Moreover, we will also introduce approximations to include quantum tunneling corrections.

2.4.5 *Quantum mechanical effects in TST*

The classical TST-based diffusion coefficient follows the Arrhenius behavior, i.e. the log of diffusivity goes linear to the inverse of the temperature. Most of the experimental studies exploit this relation to obtain the diffusion barrier and the prefactor [61, 62, 112]. However, some experimental diffusion studies have shown that the curve deviates upwards from the Arrhenius behavior due to higher diffusivity values in the low temperature range as compared to the linear approximation [68, 118]. This deviation is due to the quantum mechanical effects, which are more pronounced in the low temperature range and become negligible at high temperature [68, 119, 120]. Thus, in principle, the diffusion coefficient follows a non-Arrhenius type behavior [121].

Quantization of phonon vibrations

The quantum mechanical corrections can be incorporated to the classical TST approach in different ways. The first one is to include the discretization of the vibrational energy levels within the harmonic approximation, and the second one is to include the quantum tunneling corrections. Firstly, to include the quantized vibrations, the partition function can be re-defined with the quantum mechanical expression as [98]:

$$Z = e^{-E_0/kt} \prod_{i=1} \frac{1}{2\sinh(h\nu_i/2kT)} \tag{2.77}$$

Substituting this expression for the partition function in the definition of vibrational free energy (Eq. 2.65) gives:

$$F_Q^{vib}(T) = kT \sum_i \ln\left\{2\sinh\frac{h\nu_i}{2kT}\right\} \tag{2.78}$$

$$= \sum_i \left\{\frac{1}{2}h\nu_i + kT\ln\left[1 - e^{-h\nu_i/kT}\right]\right\}. \tag{2.79}$$

whose classical limit is given by [70]:

$$F_C^{vib}(T) = kT \sum_i \ln\left(\frac{h\nu_i}{kT}\right). \tag{2.80}$$

Thus, the change in the vibrational free energy ΔF_Q^{vib} can be written in terms of the vibrational frequencies at the saddle point (S) and at the initial point (0) as:

$$\Delta F_Q^{vib}(T) = \sum_i^{N-1}\left\{\frac{1}{2}h\nu_i^S + kT\ln\left[1 - e^{-h\nu_i^S/kT}\right]\right\} - \sum_i^{N}\left\{\frac{1}{2}h\nu_i^0 + kT\ln\left[1 - e^{-h\nu_i^0/kT}\right]\right\}, \tag{2.81}$$

with the classical limit given by [70]:

$$\Delta F_C^{vib}(T) = kT\left\{\sum_i^{N-1} \ln\left(\frac{h\nu_i^S}{kT}\right) - \sum_i^{N} \ln\left(\frac{h\nu_i^0}{kT}\right)\right\} \tag{2.82}$$

Substituting the expression for ΔF_Q^{vib} from Eq. (2.81) in Eqs. (2.62), the diffusion coefficient can be written as:

$$D_Q(T) = \frac{1}{6} z R^2 \frac{kT}{h} \frac{\prod_i^N 2\sinh\left(\frac{h\nu_i^0}{2kT}\right)}{\prod_i^{N-1} 2\sinh\left(\frac{h\nu_i^S}{2kT}\right)} e^{-\Delta E/kT}, \tag{2.83}$$

This expression for the diffusion coefficient correctly approaches the classical limit given by the TST at the high and low temperature [68, 122]:

$$\begin{aligned}\lim_{T\to\infty} D_Q(T) &= D_C(T) = D_{TST}(T) \\ &= \frac{1}{6} z R^2 \frac{\prod_{i=1}^N \nu_i^0}{\prod_{i=1}^{N-1} \nu_i^S} e^{-\Delta E/kT}, \end{aligned} \tag{2.84}$$

$$\begin{aligned}\lim_{T\to 0} D_Q(T) &= D_{TST+\Delta ZPE}(T) \\ &= \frac{1}{6} z R^2 \frac{kT}{h} e^{-(\Delta E+\Delta ZPE)/kT}, \end{aligned} \tag{2.85}$$

where ZPE is the zero-point energy, defined as the low temperature limit of Eq. (2.78) so that

$$\Delta ZPE = \lim_{T\to 0} \Delta F_Q^{vib}(T) = \sum_{i=1}^{N-1} \frac{h\nu_i^S}{2} - \sum_{i=1}^{N} \frac{h\nu_i^0}{2}. \tag{2.86}$$

The diffusion equation taking into account the quantum approximation (Eq. (2.83)) can also be written in the Arrhenius form [68]:

$$D_Q(T) = D_{QA}^*(T) e^{-\Delta E_{QA}(T)/kT}, \tag{2.87}$$

where the temperature-dependent pre-factor and the energy barrier are given by:

$$D^*_{QA}(T) = \frac{1}{6} z R^2 \frac{kT}{h} \frac{\prod_i^N \sinh\left(\frac{h\nu_i^0}{2kT}\right) \exp\left[\sum_{i=1}^{N-1} \frac{h\nu_i^S}{2kT} \coth\left(\frac{h\nu_i^S}{2kT}\right)\right]}{\prod_i^{N-1} \sinh\left(\frac{h\nu_i^S}{2kT}\right) \exp\left[\sum_{i=1}^{N} \frac{h\nu_i^0}{2kT} \coth\left(\frac{h\nu_i^0}{2kT}\right)\right]} \tag{2.88}$$

$$\Delta E_{QA}(T) = \Delta E - kT \sum_{i=1}^{N} \frac{h\nu_i^0}{2kT} \coth\left(\frac{h\nu_i^0}{2kT}\right) + kT \sum_{i=1}^{N-1} \frac{h\nu_i^S}{2kT} \coth\left(\frac{h\nu_i^S}{2kT}\right) \tag{2.89}$$

The above equations present the correct high and low temperature limits, such that Eq. (2.87) approaches Eqs. (2.84) and (2.85), respectively.

The second correction to the TST, i.e. the effect of quantum tunneling, can also be incorporated based on the type of tunneling mechanism being studied. The next subsection briefly introduces the type of tunneling mechanisms and approaches to incorporate the quantum tunneling effects in diffusion studies.

Quantum tunneling corrections

There are two types of tunneling mechanisms, each dominating in different temperature regime in addition to the classical over-barrier jump given by the TST framework. They are:

- **Coherent tunneling:** In this tunneling mechanism, the diffusing atom moves freely without any barrier similar to the Bloch-like states. It has not yet been observed for experimentally reachable low temperature limit, so we will neglect it. However, it has been observed for the diffusion of muons in metals [123].

- **Incoherent tunneling:** Incoherent tunneling is similar to the classical over-barrier jump where the tunneling of the diffusing atom is thermally activated. This is a more common approximation to include the quantum mechanical

tunneling effects [68, 119, 120] and we will briefly explain a couple of models often used for studying incoherent tunneling. Going forward, the quantum tunneling effects refers to the one due to incoherent tunneling, unless stated otherwise.

The effect of quantum tunneling (incoherent tunneling) can be included either by the Flynn and Stoneham [119] approach or by the Fermann and Auerbach [120] method. The former treats the quantum mechanical tunneling as an individual diffusion mechanism with its own diffusion coefficient while the latter treats them as a multiplicative correction factor.

Flynn and Stoneham [119] have suggested to consider quantum tunneling as a distinct diffusion process with its own diffusion coefficient calculated as Eq. (2.62). The jump rate for this diffusion process between two neighboring sites p and p' is given by [68, 119]

$$\tau^{FS} = \left(\frac{\pi}{4\hbar E_c kT}\right)^{\frac{1}{2}} J_{pp'}^2 e^{-\frac{E_c}{kT}}, \tag{2.90}$$

where $J_{pp'}$ and E_c are the tunneling matrix element and coincidence energy, respectively. Calculating these quantities is computationally demanding and often approximations are made to reduce this cost [68].

Fermann and Auerbach proposed another method to include the quantum tunneling effects as a correction factor Γ to provide the overall diffusion equation as:

$$D_{Q+\Gamma} = D_Q \Gamma, \tag{2.91}$$

where Γ is a dimensionless multiplying factor incorporating the effect of thermally activated incoherent tunneling to the diffusion equation. The factor Γ is defined as [120]

$$\Gamma(T) = \frac{e^{\Delta E/kT}}{1 + e^{2\pi\Delta E/h|\nu^{\ddagger}|}} + \frac{1}{2}\int_{-\infty}^{\pi\Delta E/h|\nu^{\ddagger}|} e^{h|\nu^{\ddagger}|\theta/\pi kT}\,\mathrm{sech}^2\,\theta\,d\theta, \tag{2.92}$$

in which $\nu^{\ddagger}$ is the imaginary frequency associated with the curvature at the saddle point. The above expression for Γ must be evaluated by using numerical integration with a sufficient lower limit for $-\infty$. At low temperature, Γ becomes proportional to $e^{\Delta E/kT}$ [120]:

$$\lim_{T\to 0}\Gamma(T) \to e^{\Delta E/kT}e^{-2\pi\Delta E/h|\nu^{\ddagger}|}\left(1 + \frac{2\pi kT}{h|\nu^{\ddagger}|}\right), \tag{2.93}$$

thus cancelling the temperature dependence term $e^{-\Delta E/kT}$, resulting in a non-zero diffusion coefficient as known from both theoretical and experimental results. While at high temperature, it goes as [120]:

$$\Gamma(T) = 1 + \sum_{n=1}^{\infty}\frac{1}{n!}\left(\frac{h|\nu^{\ddagger}|/kT}{\pi}\right)\left[\frac{\theta_0^n}{1 + e^{2\theta_0}} + \frac{1}{2}\int_{-\infty}^{\theta_0}\theta^n\,\mathrm{sech}^2\,\theta\,d\theta\right], \tag{2.94}$$

where $\theta_0 = \pi\Delta E/h|\nu^{\ddagger}|$. This expression tends to 1 as T increases, thus the diffusion coefficient converges to the classical diffusion equation, Eq. (2.84). Therefore, this quantum tunneling correction shows the correct high and low temperature limits.

As all the ingredients required for calculating Γ (ΔE and ν_i) are already available in evaluating Eq. (2.83), we used this approach to include the quantum tunneling correction. It should

be noted that in the original study [120], the correction factor Γ was multiplied by the diffusion coefficient obtained by the classical TST approach, while in the present work, the expression based on the quantum-mechanical approximation, according to Eqs. (2.87) is used.

The classical as well as the quantum mechanical expression of TST framework has so far been discussed within the harmonic approximation and ignoring higher-order terms. These higher-order terms might become important at high temperature resulting in significant deviation from the harmonic approximation [72, 109, 124]. Thus, the validity of harmonic approximation should be analyzed and the effect of anharmonicity must be computed quantitatively to estimate their significance. The next section briefly introduces couple of methods to study anharmonic effects.

2.4.6 *Anharmonic effects*

The anharmonic effects due to the volume expansion can be studied consistently using the quasiharmonic approximation. In this approach, the diffusion barrier is not constant and is defined as a function of the volume V, at a given temperature T, i.e. $\Delta E(T) = \Delta E(V(T))$, where $V(T)$ is determined by minimizing the free energy curve vs volume for a given T using the quasiharmonic approximation (QHA) [71, 125, 126].

In the QHA all the phonon frequency shifts are associated to the volume change so that phonon frequencies are explicitly volume dependent and are temperature dependent only through the thermal expansion. Although this approach is a common practice in the literature to incorporate anharmonic effects, it does not include the anharmonic effects caused by phonon-phonon interactions or in other words explicit temperature dependence.

The cBΩ model proposed by Varotsos and Alexopoulos [127, 128] incorporates both the volume and phonon-phonon temper-

ature dependence, approximately, by defining the diffusion energy barrier as:

$$\Delta E(T) = cB(T)\Omega(T) \tag{2.95}$$

where $B(T)$ is the isothermal bulk modulus, $\Omega(T)$ is the mean volume per unit atom, and c is the dimensionless constant with respect to temperature and pressure. The constant c can be obtained by fitting the Eq. (2.95) with the diffusion energy barrier (ΔE) estimated from the experimental data or with the one calculated from first-principles at $T = 0$.

The quantum-mechanical treatment and the incorporation of anharmonic effects provide an accurate description of the diffusion coefficient, which is valid for a wide temperature range and can be compared directly with the experimental data. However, it is limited to only one type of jump, which might not be the case in most diffusion studies [129–131], for example Li diffusion in c-LiSi. However, one can use methods like kinetic monte carlo (KMC) simulations [132, 133] to get the effective diffusion coefficient from multiple types of jumps [129, 130]. The next subsection briefly introduces the KMC algorithm and its implementation to obtain the effective diffusion coefficient in the presence of multiple jumps.

2.4.7 *Kinetic Monte Carlo method*

The KMC method treats each jump as an independent process, i with a jump rate τ_i defined as [114, 122]

$$\tau_i = \gamma_i e^{-\Delta E_i/kT}, \tag{2.96}$$

where γ_i is the attempt frequency, ΔE_i is the energy barrier obtained by NEB calculation, k is the Boltzmann constant and T is the temperature. Substituting Eqs. (2.83) and (2.84) in Eq. (2.63), the jump rate (τ_i) can be obtained with the quantum and classical approximations, respectively. The main steps of KMC simulation are mentioned below, for a detailed review of KMC algorithm we refer the reader to the literature [134–136]:

Step 1: Identify all the events (q) that can take place in the current atomic configuration.

Step 2: Determine rates (k_i) of all the possible events. The jump rate τ_i for an event i is given by the transition state theory [114, 122] as:

$$\tau_i = \gamma_i e^{-\Delta E_i / kT}, \tag{2.97}$$

where γ_i is the attempt frequency, ΔE_i is the energy barrier, k is the Boltzmann constant and T is the temperature associated with event i. For all the events, the attempt frequency was calculated using the phonon vibration modes and energy barriers by the NEB method. For classical approximation, the attempt frequency (γ_i) is the ratio of phonon frequencies for initial and saddle point within the classical transition state theory framework, and is temperature invariant. For the quantum approximation it varies with temperature and is given by:

$$\gamma_i = \frac{kT}{h} \frac{\prod_{i=1}^{N} 2 \sinh\left(\frac{h\nu_i^0}{2kT}\right)}{\prod_{i=1}^{N-1} 2 \sinh\left(\frac{h\nu_i^S}{2kT}\right)}. \tag{2.98}$$

Step 3: Generate a uniform random number between 0 and 1 (r_1) to select the event p out of all the q events to take place as:

$$\sum_{i=1}^{p-1} k_i < r_1 k_{tot} \leqslant \sum_{i=1}^{p} k_i, \tag{2.99}$$

where k_{tot} is the cumulative sum of rates of all the possible events.

Step 4: Reconfigure the system according to the selected event.

Step 5: Since, selecting an event randomly is a type of Poisson process, the time evolution for each KMC step can be evaluated as [137]:

$$t \rightarrow t - \ln(r_2)/k_{tot}, \tag{2.100}$$

where r_2 is a second random number between 0 and 1.

Step 6: Update new positions of Li atoms and vacancy, update the time according to Step 5.

Step 7: Return to step 1.

The process need to be repeated for sufficiently large number of times. The diffusion coefficient can then be calculated as the time-weighted average of the diffusion coefficients for each site i [136]

$$D = \sum_i D_i \Delta t_i / t, \tag{2.101}$$

where D_i is the diffusion coefficient calculated for each site i over time Δt_i, and t is the total time for the entire KMC simulation, and the expression

$$D_i = \langle [r(t_i) - r(t_0)]^2 \rangle / 2d\Delta t_i, \tag{2.102}$$

gives the diffusion coefficient of each site i. The vectors $r(t_i)$ and $r(t_0)$ represents the final and initial position of the vacancy, respectively. The variable d denotes the dimensions of the simulation and the $\langle .. \rangle$ denotes the average over all particles.

It should be noted that the effective diffusion coefficient thus obtained are discrete data points for a particular temperature T unlike the continuous curve obtained by TST. The overall diffusion equation can then be obtained by fitting these data points.

Now, we are equipped with calculating the diffusion barrier and the phonon frequencies with DFT calculations including quantum mechanical effects and anharmonic effects for single or multiple diffusion process. The next section briefly introduce the classical potential based methods, which are more suitable to

deal with large simulation cells at the expense of limited range of applicability.

2.5 CLASSICAL POTENTIALS

First-principles methods indeed provide an accurate description of material properties with good reproducibility [138–140]. These methods are computationally expensive and are often limited to a few hundreds of atoms. For applications involving large number of atoms, empirical-potentials or force-field-based methods are often helpful. Most of these empirical potentials are based on an empirical model of the interatomic interaction taking into account bond angles, dihedral angles, Coulomb repulsion, van der Waals forces, etc and thus often known as interatomic potentials as well [141–143]. These interatomic potentials are parameterized using experimental or first-principles results [144, 145], thus providing an ad-hoc functional to obtain quantum mechanical effects without solving the computational extensive Schrödinger equation again. However, one has to be careful with the window of validation based on the parameterization and the theoretical constraint of the potential. For instance, in Lennard-Jones type pair potentials, the cohesive energy (E_{coh}) scales linearly with the coordination number (Z) because one bond is unaffected by the presence of another. However, in reality the strength of an additional bond is not the same but rather decreases with Z ($E_{coh} \propto -Z^{1/2}$) resulting in a slower decrease of cohesive energy (E_{coh}) [146]. Thus, these potentials should be validated before trying any simulations.

For system containing just silicon atoms, several empirical potentials have been developed in the past that accurately describe the properties of silicon atoms. Not exhaustively, some important Si potentials are Tersoff [141, 147], Stillinger-Weber (SW) [142], and Modified Embedded Atom Method (MEAM) [143, 148]. Out of which, the last one was able to be modified for including interactions with other atoms e.g. Li, Fe, O, etc. Another class of classical potentials capable of dealing with interactions of Si with other atoms are called Reactive force-field

(Reaxff) [149, 150]. Reaxff is a bond order based potential that allows bond formation and bond dissociation during MD simulations. However, the number of energy terms involved in the definition make it a tedious process to optimize this potential and also limits the transferability. The MEAM potential is based on the idea of Embedded Atom Method (EAM) proposed by Daw and Baskes [148, 151] in 1983. In this approach, the energy of an atom is computed by embedding an atom in the local electron density created by the remaining atoms, resulting in a better relation of cohesive energy with coordination number. The total energy in EAM is defined as:

$$E = \sum_i \left[F_i(\bar{\rho}_i) + \frac{1}{2} \sum_{j(\neq i)} \phi_{ij}(R_{ij}) \right] \tag{2.103}$$

where F_i is the embedding function that defines the energy required to embed an atom i in a local electron density ϕ_i at site i. The parameter ϕ_{ij} denotes the pair interaction energy between two atoms R_{ij} distance apart. Later on Baskes proposed a Modified EAM (MEAM) [143], which was more suitable to study metals, and diamond structure of Si. However, Lee *et al.* [152] pointed out that it is not predicting the most stable crystal structure of Li at room temperature and proposed a 2NN MEAM. In 2NN MEAM the energy per atom can be obtained from a universal equation of state, which made it quite popular. In this Chapter we will compare two different parameterizations of this 2NN MEAM to select one for studying delithiation. For more details about EAM or MEAM potential formulation, the reader can go through these references [143, 146, 148, 151–154]. The next section briefly introduce a relatively new tool to characterize the local environment of individual species, which has been used in this thesis.

2.6 CHEMENV TOOL

Chemenv uses the Voronoï tessellation method [155] to find the best possible local environment for any site in a crystal struc-

ture [156]. It has already been tested to accurately find local environments of several oxides [157–159]. The two important parameters in this Voronoï tessellation is the cutoff values for the dihedral angle and the distance cutoff, above which the edge is considered in the tessellation and the neighbour is counted (see Fig. 2.2). For more details, the reader can go through the original paper by Waroquiers *et al.* [156]. This tool has been used in this thesis for analysing local environments of Si and Li.

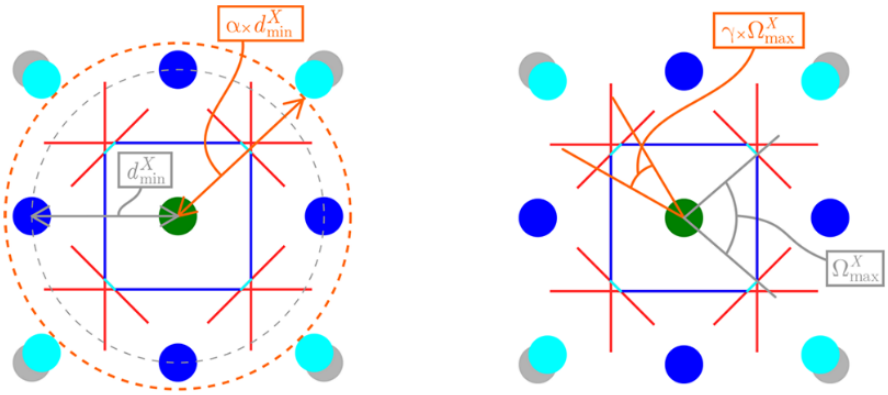

Figure 2.2: A 2-dimensional schematic representation of the distance and angle cut- offs used in the Voronoï procedure for determining the neighbors of a given atom. a) Distance cutoff α. Any atom with a distance smaller than or equal to the distance cutoff α times the minimum neighbour distance d^X_{min}, is considered as a neighbour. b) Angle cutoff γ. Any neighbour forming the solid angle greater than or equal to γ times the largest solid angle Ω^X_{max} is considered as a neighbour. Reprinted with permission from Ref. [156]. Copyright 2017 American Chemical Society.

Equipped with tools and techniques to perform first-principles calculations as well as classical molecular dynamics and to characterize resulting structures, the next chapters provide the applications of these techniques to study Li dynamics in silicon-based materials.

3

DIFFUSION OF LI IN BULK SI AND CRYSTALLINE LISI

3.1 INTRODUCTION

The practical application of silicon-based anode materials in Li-ion batteries (LIB) has been limited primarily due to the huge volume change they experience. Silicon-based anodes expand up to 300 % during charge/discharge cycles [40, 160] resulting in electrode disconnection, irreversible capacity loss and mechanical failure of electrodes [14, 27, 161]. This is primarily due to the structural transformation silicon undergoes during Li insertion and removal [162]. Unlike Li intercalating between graphitic layers, in case of silicon it can form several lithiated Li-Si phases during lithiation [31].

Over the years, nanostructure engineering has significantly reduced the problem of volume expansion and consequent pulverization [48, 50, 163–166]. The engineering of nanostructures provides great control in anode design to accomodate the volume expansion and increase the mechanical strength by coating [47, 50, 167]. Although these approaches have improved the electrochemical cycling performance, intrinsic challenges such as stress generation and phase transformation remain largely unsolved due to a lack of critical knowledge about the dynamics of lithiation [129]. Furthermore, as silicon forms lithiated Li-Si phases upon lithiation [57, 168], the lithiation/delithiation dynamics as well as the phase transformations are largely governed by the Li diffusivity within these Li-Si phases and at the interface region with pristine Si [129, 169]. Thus, in order to understand the structural changes, it is paramount to investigate the kinetics of Li in both bulk Si and in various lithiated phases.

Several experimental methods such as potentiostatic and/or galvanostatic intermittent titration technique (PITT, GITT) [62], nuclear magnetic resonance (NMR) [170], electrochemical strain mapping (ESM) [63], and electrochemical impedance spectro-

scopy (EIS) [171] have been used to estimate Li diffusion coefficients in Si-based anode materials. Nevertheless, an accurate quantitative measurement of the Li diffusion coefficient in lithiated Si is still a challenging task, because of phase transformations upon lithiation, precise sample preparation and controlling other experimental parameters. Consequently, there is a large discrepancy in the experimentally reported values of Li diffusivity in lithiated Li_xSi ($x \geqslant 1$), spanning 4 orders of magnitude from 10^{-8} to 10^{-12} cm^2/s in room temperature values [62, 63, 65, 66, 171].

First-principles methods based on Density functional theory (DFT) have been very successful in providing an atomic-level description of diffusion mechanisms as well as overall diffusivity values. Such DFT studies have shown that Li occupies the tetrahedral (T_d) site in the Si lattice during the initial phase of lithiation and jumps to the adjacent T_d site via the hexagonal (H_x) transition site [60]. The diffusion barrier calculated from first-principles (0.59 eV) [60, 172, 173] is in a reasonable agreement with the experimental value of 0.655 ± 0.01 eV [61]. While on the other hand, Li diffusion barrier in a-Si is much more tricky to study using NEB method. Tritsaris *et al.* [172] have obtained a series of energy barriers ranging from 0.1 eV to 2.4 eV, where a high energy barrier and centrality of the site can act as a bottleneck in long range diffusion . However, most of these first-principles studies have been limited to the calculation of the diffusion barrier while the diffusion coefficient is at most estimate.

In order to study the kinetics, DFT-based *ab-initio* molecular dynamics (AIMD) simulations have been used frequently to compute the diffusion coefficient. Despite the overall success of such simulations in particular for electrolytes [23], the technique is limited to fast diffusion processes. It is indeed computationally expensive and sometimes even infeasible to get the desired convergence, especially in dilute doping limits. Consequently, the diffusion coefficients of Li in Li_xSi ($x \geqslant 1$) calculated from AIMD simulations at 300 K show a variation of 5 orders of magnitude spanning from 10^{-9} to 10^{-14} cm^2/s [174–178]. In fact,

AIMD simulations are generally conducted at high temperature to accelerate the diffusion process and the diffusion coefficient is then extrapolated to room temperature. The discrepancy in the reported values can be due to small errors due to convergence, which are then amplified by the extrapolation to room temperature. Additionally, the diffusion mechanism at high temperature may be qualitatively different than at room temperature and the extrapolation of the diffusion coefficient might not be a plausible approximation, especially if there is a phase change and a consequent change in the diffusion mechanism.

Recently, Moon *et al.* [129] studied Li diffusion in Si and various Li_xSi alloys using the Kinetic Monte Carlo (KMC) method based on the energy barriers calculated from first-principles. They found a diffusion coefficient of Li in LiSi in the range of 10^{-11}-$10^{-12}\,cm^2/sec$ at 300 K with an effective barrier of 0.306 eV. Although their results are in good agreement with the experimental data at 700 K, it is not clear whether they used classical or quantum approximations in calculating the diffusion prefactor for the KMC studies. The treatment of atomic nuclei as pointlike classical particles may lead to inaccuracies in the description of Li atoms. A few studies have suggested the presence of quantum effects in studying Li atoms in FePO [179] and graphite [70] but it has not yet been studied explicitly for the Li-Si system.

An approach to obtain a non-classical description of diffusion based on the transition state theory (TST) has been proposed [68, 70]. The suggested method is computationally cheaper and yet it provides a comparable accuracy to expensive path integral (PI) based on AIMD methods. This approach has been successfully tested for hydrogen diffusion in metals [68], Li diffusion in graphite [70], self diffusion of Si [180], and many more systems [181–183]. This method is often used with harmonic approximation for computing the phonon frequencies, and it is important to estimate the effect of anharmonicity in the system that might become significant at high temperature.

The literature on anharmonicity in diffusion discusses mainly two types of effects: 1) those due to the change in the lattice parameter owing to thermal expansion at high temperature [184,

185], and 2) those due to the phonon-phonon interactions [72, 186]. The first effect, i.e. the volume change, is often studied through the quasiharmonic approximations (QHA) that provides a first-order anharmonic correction [187]. However it can underestimate the phonon frequency change when the phonon-phonon interactions contribute significantly in phonon softening at high temperature [72]. In order to address both effects, Varotsos and Alexopoulos [127, 188] proposed the cBΩ model that connects the Gibbs free energy (for defect formation or for migration) to the isothermal bulk modulus (B) and the volume per atom (Ω), changing as a function of temperature. The model gives slightly better agreement with the experimental data as compared to a similar model proposed earlier by Wert and Zener that connects the gibbs free energy of formation to the shear modulus, μ of the material [111, 189, 190].

In the present Chapter, the methodology based on TST is followed and its limitations are discussed along with a measure of anharmonic effects in calculating the diffusion coefficient. We examine Li interstitial diffusion in bulk Si, as well as Li diffusion in the crystalline lithiated phase LiSi. The LiSi phase is selected as it is difficult to observe its formation in room temperature experiments due to the slow kinetics of formation and narrow temperature range of stability [191, 192]. Thus, it is often not considered in studying Li-Si system [62, 193]. However, it is a stable phase below 600 K and it can be synthesized at a pressure of 1−2.5 GPa and a temperature range of 773 K−993 K (500−700°C) [31, 194]. Thus our study on Li diffusion in LiSi might reduce the gap in the literature of LiSi alloy. The effect of anharmonicity is estimated by the cBΩ model and compared with the quasiharmonic approximation. For this purpose, we compute from first principles the temperature-dependent primitive cell volume and bulk modulus for the LiSi phase, which had not yet been computed or measured, to the best of our knowledge.

3.2 COMPUTATIONAL DETAILS

The first-principles total energy calculations were performed with DFT as implemented in the ABINIT code [195–198] using a plane-wave basis set within the generalized-gradient approximation (GGA-PBE) [199]. The converged plane-wave cutoff energy was 32 Ha (~871 eV) and 12 Ha (~327 eV) for bulk Li and Si, respectively. For bulk Si doped with Li and for LiSi structure, a cutoff energy of 32 Ha (~870.76 eV) was used. The optimized norm conserving pseudopotentials (ONCVPSP) pseudopotentials [200] from the PseudoDojo project [201] were used with 1s and 2s electrons as valence electrons for Li while, for Si, 3s and 3p electrons were treated as valence electrons.

A supercell of 96 Si atoms (2×3×2 of the conventional unit cell) was used for studying bulk Si, then adding one interstitial Li atom, and a supercell of 128 atoms (2×2×2 of the primitive unit cell) was considered for the c-LiSi structure, then depleted of one Li atom. For sampling the Brillouin zone, a 2×2×2 Monkhorst-Pack k-point mesh was used. The kinetic energy cutoff and the k point sampling were obtained from convergence studies with a tolerance level of 0.5 mHa/atom (~14 meV/atom). The self consistent field (SCF) cycles for the total energy calculations were converged until the difference in forces between the two consecutive cycles was less than 10^{-7} Ha/Bohr (0.005 meV/Å) twice in a row. The structural relaxations were performed using the (BFGS) minimization until the forces on each atom were smaller than 5×10^{-6} Ha/Bohr (0.3 meV/Å). For metallic systems, a Gaussian smearing of 0.01 Ha (0.23 eV) was used for the occupation of states [202].

In the case of Li diffusion in bulk Si, the most stable position for a single Li atom is the tetrahedral (T_d) interstitial site. Li atoms diffuse by jumping to the next vacant T_d site via an hexagonal (H_x) site [60, 203]. The corresponding jump distance, i.e. the distance between two T_d sites in a diamond lattice, is $a\sqrt{3}/4$. The energy barrier for Li diffusion was calculated by the NEB method [117]. In order to find the diffusion barrrier profile, at least 7 images were used with 2 fixed (initial and final images)

and 5 dynamic images. All the images were relaxed until the absolute energy difference was less than 10^{-5} Ha (0.27 meV). The effective diffusion coefficient of Li in LiSi was obtained through KMC simulations. In order to obtain better statistics, each KMC simulation was run for 10,000 steps and averaged over 40,000 sites, an approach suggested in previous KMC studies [130, 136].

The TST formalism requires to compute the phonon frequencies only at the Γ point. This is what was done in calculating the diffusion coefficient for computational efficiency. However, the full phonon band structures of smaller cells were also produced for illustration purposes. All these calculations were performed using the density functional perturbation theory (DFPT) as implemented in the ABINIT code [104, 105, 204].

For computing the volume expansion using the QHA, the phonon contribution of the free energy has been calculated at three volumes, i.e. at the equilibrium point as well as for 1% and 6% volume expansion at temperatures from 10 K to 1000 K with a step of 10 K, and fitted with a quadratic expression for each temperature. The total energy was calculated at 34 points starting from a structure with 3% lower volume to the one with 30% higher volume than the equilibrium structure and fitted with a fourth-order polynomial, appropriate in that range. The summation of the total energy and the phonon free energy gives the free energy curves at a temperature interval of 10 K. The equilibrium volume is thus obtained by minimizing the free energy curves and the isothermal bulk modulus, $B(T)$ is obtained as [205]:

$$B(T) = \frac{\partial^2 F}{\partial V^2}\bigg|_{V(T)} V(T) \tag{3.1}$$

The volume dependent diffusion barrier in the QHA was obtained by computing first the energy barrier calculated at 0 K and at an increased volume corresponding to high temperature

(T_h), say 1000 K, then performing a linear interpolation of the volume-dependent energy between these two values

$$\Delta E(T) = \Delta E_0 + \frac{\Delta E_{T_h} - \Delta E_0}{V_{T_h} - V_0}(V(T) - V_0) \tag{3.2}$$

where ΔE_0 and V_0 are the diffusion barrier and mean volume per atom calculated at 0 K from first principles, ΔE_{T_h} and V_{T_h} represents the diffusion barrier and the associated mean volume per unit atom calculated at a high temperature T_h, respectively, and $V(T)$ represents the mean volume per unit atom at a given temperature T. In the case of bulk Si, the data from Ref. [71] have been used to calculate $V(T)$ and $B(T)$, while for LiSi, these thermodynamic quantities has been calculated from DFPT as implemented in ABINIT [104, 105] with the above-mentioned computations.

3.3 LI DIFFUSION IN BULK SI

3.3.1 *Li insertion into bulk Si*

In bulk Si, the most stable position for a single Li atom is the tetrahedral (T_d) interstitial site [60]. The optimized lattice parameters for our pristine 96-atoms Si supercell are 10.93, 10.93, and 16.41 Å, which increase to 10.94, 10.94, and 16.41 Å after the addition of 1 interstitial Li atom. It is less than 0.1% increase in the lattice parameters. The corresponding formation energy per Si atom for 1 Li interstitial was computed as ~0.002 eV, which is in line with known positive formation energy in dilute doping limits [206]. Fig. 3.1 shows the effect of one Li atom addition on the electronic density of states (DOS) of bulk Si (16 atom supercell, for illustration purposes) in an energy window corresponding to the valence and conduction states spanning the interval [-15 eV,5 eV] around the Fermi energy. Upon Li addition, the DOS is almost unchanged. However, the peak heights near the conduction bands are modified since the 2s electron of the interstitial Li is added to the conduction band. Consequently the Fermi energy moves into the conduction band making it a metal-

lic system. The Fermi energy increases by 0.34 eV upon addition of one Li atom to the 16-atom supercell.

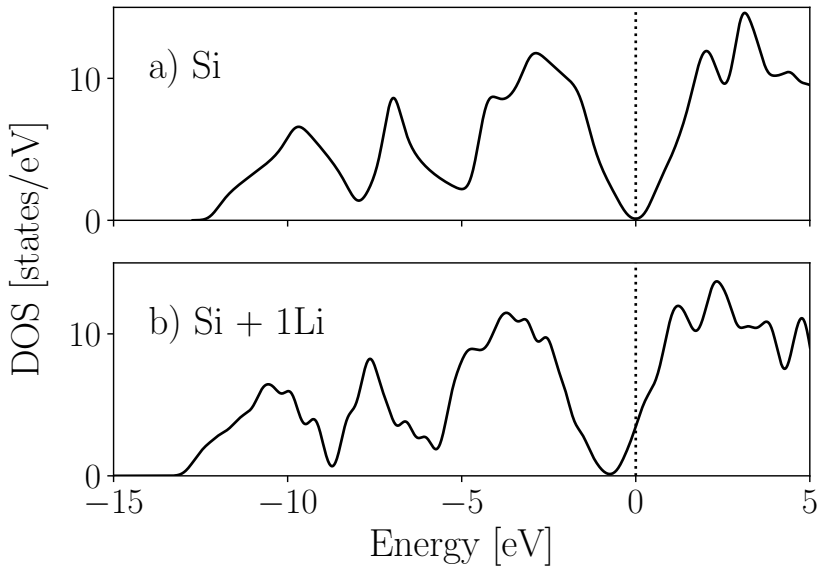

Figure 3.1: Electronic density of states of a) bulk Si and b) bulk Si with 1 Li atom at the T_d interstitial site. The Fermi energy is set to zero on the x-axis (dotted line). A 2×2×2 supercell with 16 Si atoms has been used to simulate bulk Si. These small-cell results are shown for illustration purpose only.

Fig. 3.2 shows the effect of Li addition on the vibrational properties of bulk Si (16-atom cell, for illustration purpose). First of all, after Li addition, three new high energy vibrational modes are observed. These three modes represent the vibrational frequency of the light Li atom in the three spatial dimensions. In order to check the convergence with respect to the supercell size, supercells of 54 atoms (3×3×3 of the primitive unit cell) and 96 Si atoms (2×3×2 of the conventional unit cell) were also considered. The corresponding diffusion barriers and diffusion coefficients are included in the Appendix A (see Fig. A.1). Convergence tests confirmed that a supercell of 96 Si atoms is large enough to avoid any inter-atomic interaction across periodic bound-

aries and thus the 96 atom supercell was used to study bulk and doped Si.

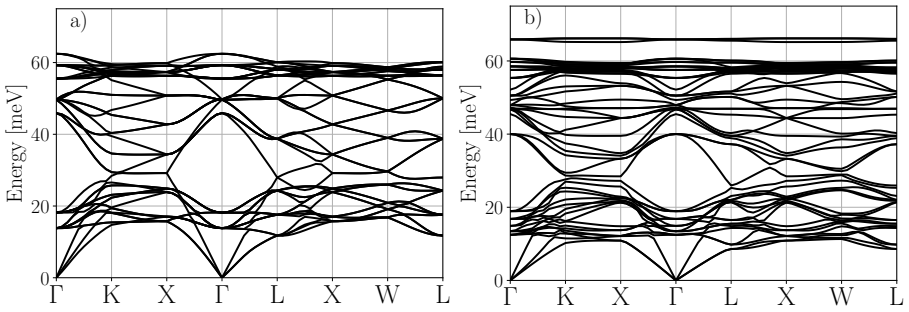

Figure 3.2: Phonon band structures of a) bulk Si and b) bulk Si with 1 Li atom at the T_d interstitial site. The three extra Li modes are clearly seen around 65 meV in the latter. A 2×2×2 supercell with 16 Si atoms has been used to simulate bulk Si. These small-cell results are shown for illustration purpose only.

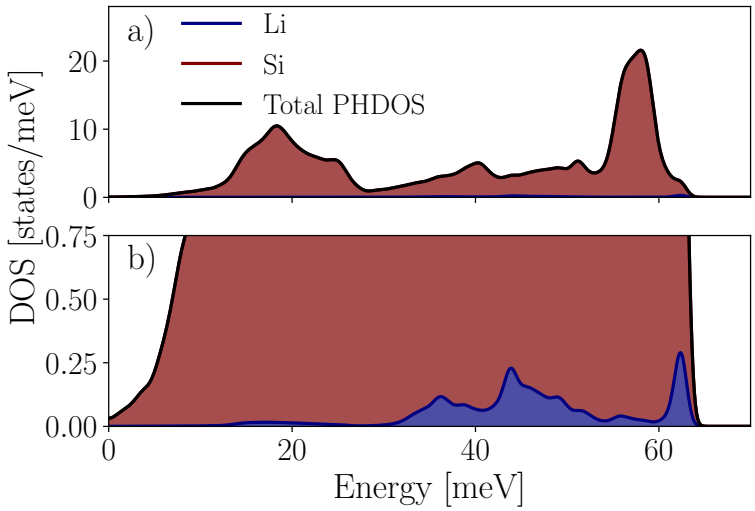

Figure 3.3: Partial phonon density of states (PPDOS) of a) 96-atom supercell with 1 Li atom and b) a zoomed-in image of the same PPDOS showing the the partial contribution of Li atoms overlapped with those of Si atoms.

The partial phonon density of states (PPDOS) from this 96 atom supercell (Fig. 3.3) allows us to identify the three modes predominantly associated with localized vibrations of the interstitial Li atom in the three cartesian directions. Moreover, these modes also involve significant Si displacements, i.e. the interstitial Li atom can not vibrate freely without affecting the neighboring Si atoms. Despite this collective behavior, we shall call such modes “Li modes" in this work. These coupled vibrations are due to the partial charge transfer between the interstitial Li and the neighboring Si atoms that inhibit the free movement of the Li atom like a neutral interstitial atom [60]. Thus, unlike in the case of hydrogen diffusion in metals (metals are heavier than Si) [68], here it is not possible to assume that the light Li atoms move freely in the host lattice. Therefore, all the phonon modes have to be considered for calculating the diffusion coefficient. After analyzing the effect of Li insertion into bulk Si, in the following section, the diffusion of this interstitial Li atom in bulk Si is discussed.

3.3.2 *Diffusion mechanism: Interstitial diffusion*

The energetically favorable diffusion pathway for a single Li atom is $T_d \rightarrow H_x \rightarrow T_d$ as suggested by previous studies [60]. The diffusion barrier computed by the NEB method is 0.59 eV (Fig. 3.4), which is in good agreement with previous experimental and theoretical studies [60, 61, 206]. As expected, the diffusion path is symmetric across the barrier.

Figs. 3.5 a and 3.5 b show the phonon density of states for the initial (Li at T_d site) and saddle (Li at H_x site) point configurations, respectively. The initial point configuration shows three Li modes coupled with Si as mentioned in the previous section. For the saddle point configuration, two of these Li modes become degenerate at 80 meV and the remaining one is an unstable mode with an imaginary frequency 32 meV (represented as negative in Fig. 3.5 b). The degeneracy of the two high-energy Li modes comes from the crystal symmetry, and the unstable mode from the displacement in the direction that connects the two local min-

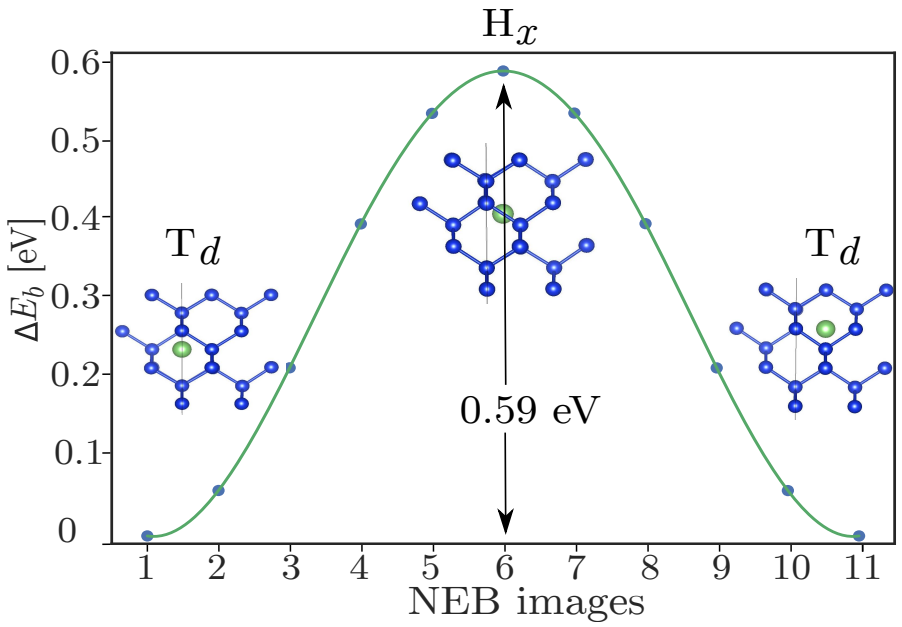

Figure 3.4: Diffusion barrier calculated by the NEB method for one Li atom diffusing in bulk Si.

ima. However, similar to the initial state, all three Li modes are still coupled with Si. The hardening of the doubly degenerate mode can be understood from the proximity of the Li atom to Si atoms at the saddle point, causing faster increase of the potential felt by the Li atom when vibrating perpendicular to the transition path direction.

Fig. 3.6 shows the difference in vibrational free energy ΔF_C^{vib} and ΔF_Q^{vib} calculated adopting the classical and quantum approximations as described in Chapter 2. At 0 K, the quantum ΔF_Q^{vib} has a finite value of 16 meV, while the classical approximation reaches zero. The difference between both approximations reduces to ~7 meV at room temperature as they converge to the same value at high temperature.

These vibrational energies were then used to calculate the diffusion coefficient with the classical and quantum approximations. The jump distance is the distance between two tetrahedral voids in a diamond lattice, i.e. 2.368 Å. The calculated diffusion coefficient was plotted on a logarithmic scale vs 1000/T (Fig. 3.7),

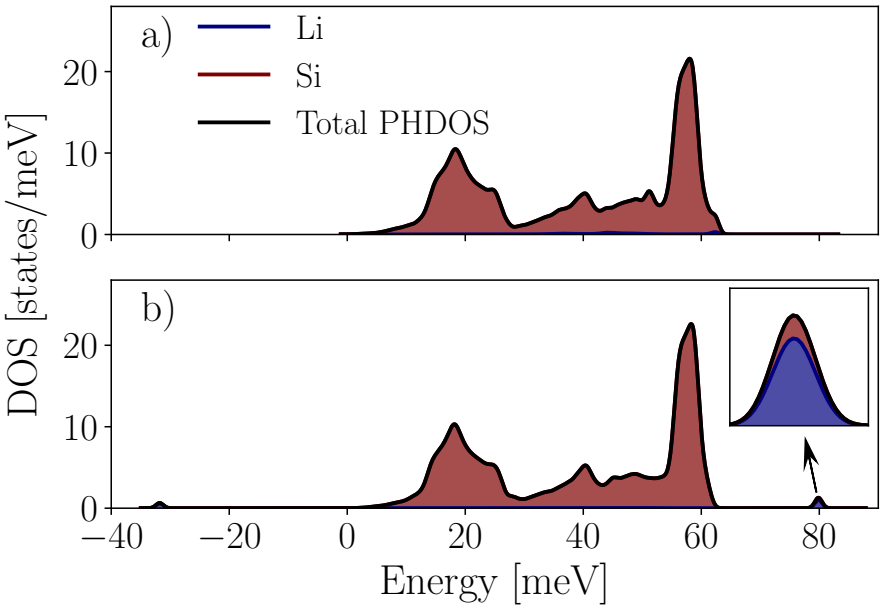

Figure 3.5: Partial phonon density of states (PPDOS) of bulk Si (96 atoms) with one Li a) at the T_d site (minimum energy geometry) and b) at the H_x site (saddle point geometry). At the saddle point, two Li modes become degenerate at higher vibrational frequency (at 80 meV) and the third one shifts to an imaginary frequency (at -32 meV) represented as negative for illustrating purposes, corresponding to the vibration in the direction of propagation at the saddle point.

showing an Arrhenius-like behavior for both the quantum (blue) and classical (red) theories. Their ratio is also shown in Fig. 3.8: it is close to one at high temperature (> 1000 K), while it can be significantly smaller at lower temperature, e.g. 0.6 near room temperature. Both approaches are in reasonable agreement with the experimental data of Pell *et al.* [61] and the theoretical calculation of Fedorov *et al.* [207], specially at high temperature given the usual uncertainties, and rapid changes with temperature of such quantities. The pre-factor of 1×10^{-3} cm^2/s calculated for Li diffusion in bulk Si, is in a reasonable agreement with the experimental value of $2.3\pm0.2\times10^{-3}$cm^2/s. However, the other values

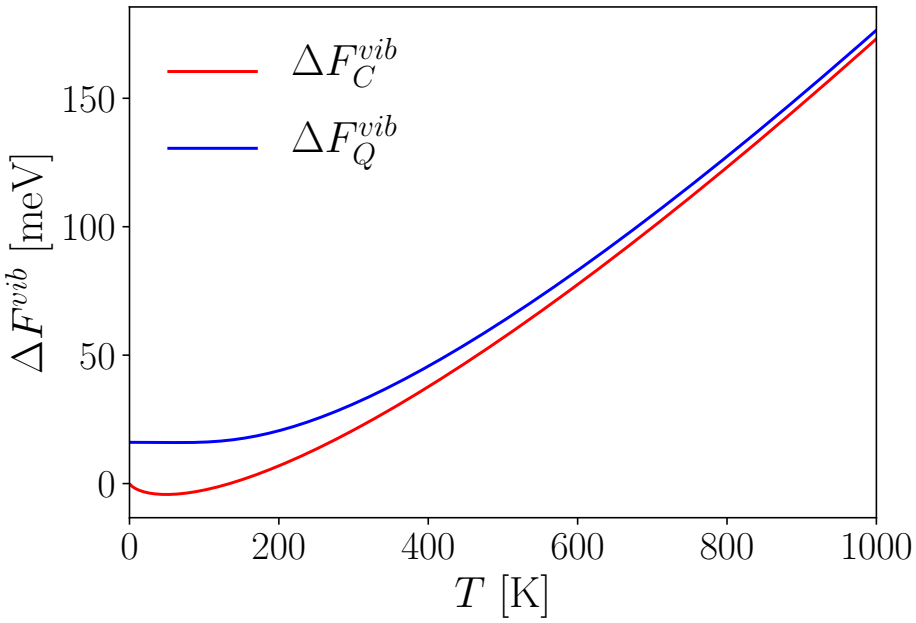

Figure 3.6: Temperature dependence of the change in vibrational free energy between the initial and the saddle point with classical (red) and quantum (blue) approximations.

reported in literature (Ref. [63, 66, 178]) at room temperature are at least 3 to 4 orders of magnitude higher.

Johari *et al.* [178] studied Li diffusion by the means of AIMD during the mixing of Li and Si atoms, where the host lattice transforms from c/a-Si in the beginning to a-Li_xSi phase. We know that Li diffuses at least one order of magnitude faster in Li_xSi phases as compared to bulk-Si [62], which justifies a higher value. Balke *et al.* used a value of $\sim 10^{-8} - 10^{-10}$ cm^2/sec to study diffusion of Li-ion by means of ESM in a-Si, where Li diffusivity is expected to be higher as compared to c-Si [178, 207]. Moreover, it was not a direct measurement of Li diffusivity and they also reported some problems during probing the sample, which they suggested was either due to a higher or lower Li-ion mobility than they assumed. The result of Yoshimura obtained with silicon thin film *et al.* [66] ($2\times10^{-11}cm^2/sec$) is the closest, among these three, to the values reported by Pell *et al.* [61] for single

crystal at room temperature. They suggested that a lower density ($1.2\,g/cm^{-3}$) of the thin film as compared to that of single crystal results in a comparatively loose structure and consequently a higher Li diffusivity. Moreover, they were not sure if it was without any alloy formation of Li_xSi during polarization, which will also attribute to a higher diffusivity value.

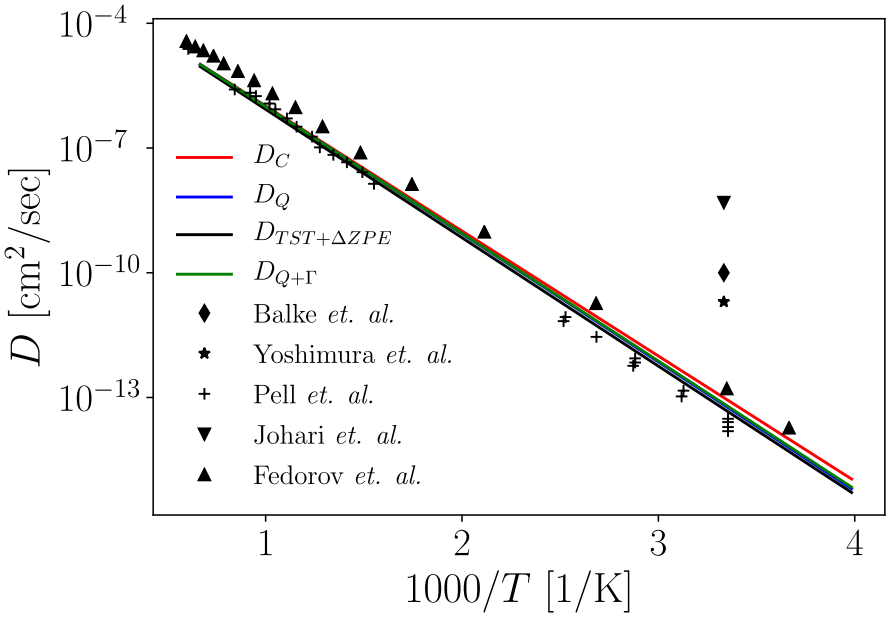

Figure 3.7: Temperature dependence of the diffusion coefficient calculated for Li in bulk Si. Blue and red lines represent the diffusion coefficient calculated with quantum and classical approximations, respectively. The black line shows the classical approximation with ZPE correction only and the green line represents the quantum approximation with quantum tunneling correction. The markers represent the values reported in the Ref. [63, 66, 112, 178, 207].

3.3.3 *Effect of quantum mechanical approximation*

The diffusion equation in the Arrhenius form with the quantum mechanical approximation has a temperature-dependent energy barrier (ΔE^*_{QA}) instead of a constant energy barrier with the clas-

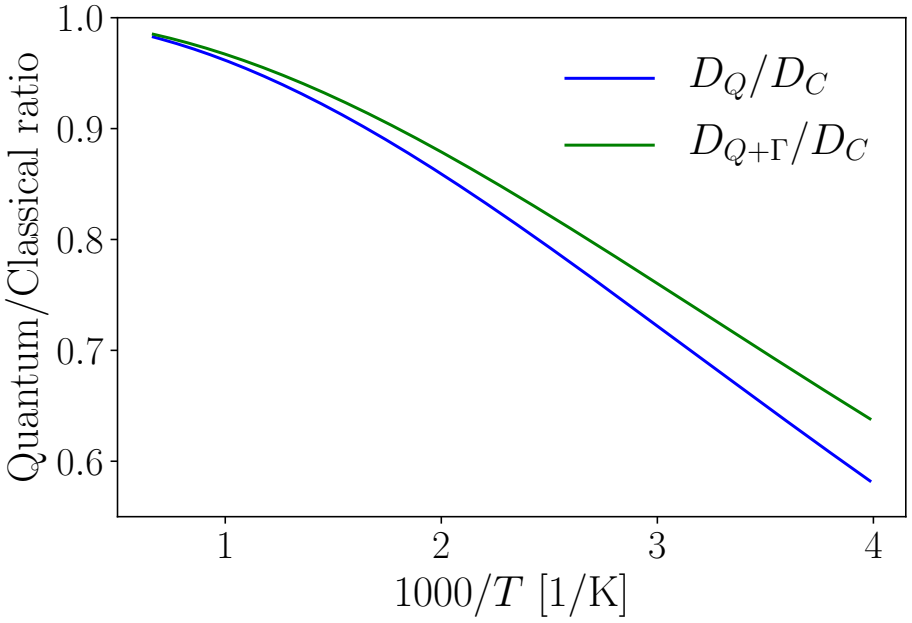

Figure 3.8: Temperature dependence of the effect of quantum corrections on the diffusion coefficient measured as a ratio of D_Q/D_C (blue). The ratio $D_{Q+\Gamma}/D_C$ (green) shows the added effect of quantum tunneling corrections that slightly increases the diffusion coefficient in the low temperature regime.

sical approximation. Fig. 3.9 a shows this temperature dependence of the energy barrier along with the constant barrier from the classical TST framework. The effective activation barrier increases in the lower temperature range to reach a maximum and then decreases tending to converge to the classical limit at high temperature. At 0 K, the effective energy barrier is higher than the classical limit because of the zero-point energy (Δ ZPE).

Similarly, the effective diffusion pre-factor (D^*_{QA}) increases in the low-temperature regime to reach a maximum and then decreases to tend to the classical limit in the high-temperature regime (Fig. 3.9b). However, it is worth noting that due to a significant contribution from quantum tunneling effects (Γ) in the low-temperature range (Fig. 3.10), the corrected diffusion pre-factor ($D^*_{QA}.\Gamma$) does not reach a maxima but rather diverges at low temperature. This exponentially increasing value of ($D^*_{QA}.\Gamma$)

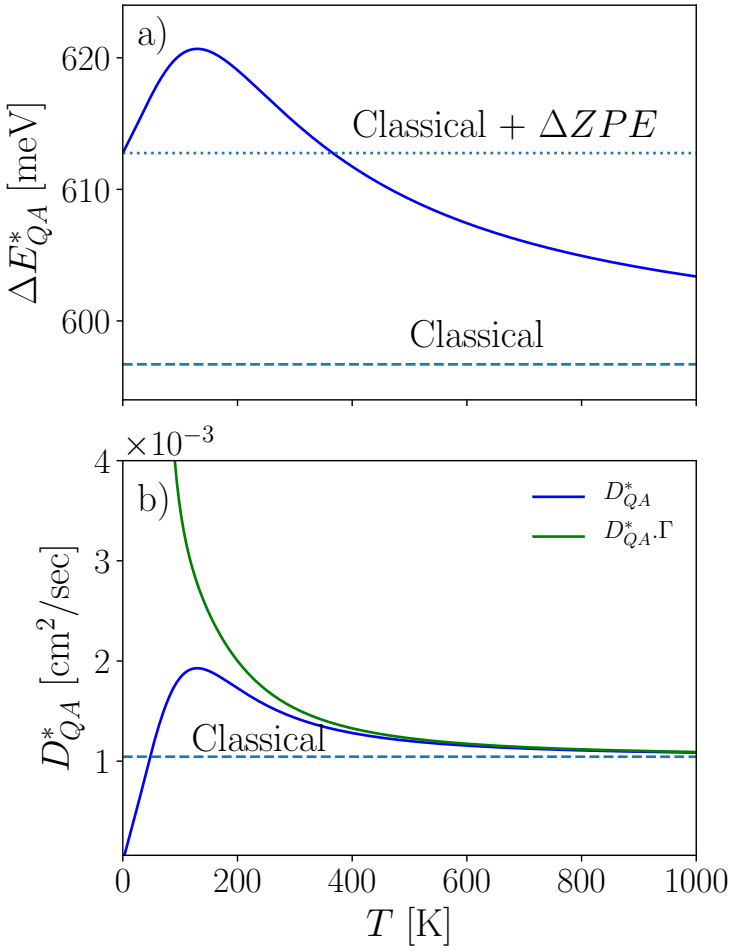

Figure 3.9: Temperature dependence of a) the effective activation barrier (ΔE_{QA}) and b) the effective diffusion prefactor (D^*_{QA}), in blue, along with the quantum tunneling corrected prefactor ($D^*_{QA}.\Gamma$), in green. These parameters of Arrhenius-like diffusion equation tend to their temperature-invariant classical limits, ΔE_m and D_0, respectively (dashed line), at high temperature.

cancels out the Arrhenius exponential temperature dependence in Eq. (2.87), thus resulting in a finite value of the diffusion coefficient in the low-temperature range [120]. The inclusion of quantum tunneling corrections slightly increases the diffusion coefficient ratio from 0.6 to 0.66 (Fig. 3.8) owing to an additional

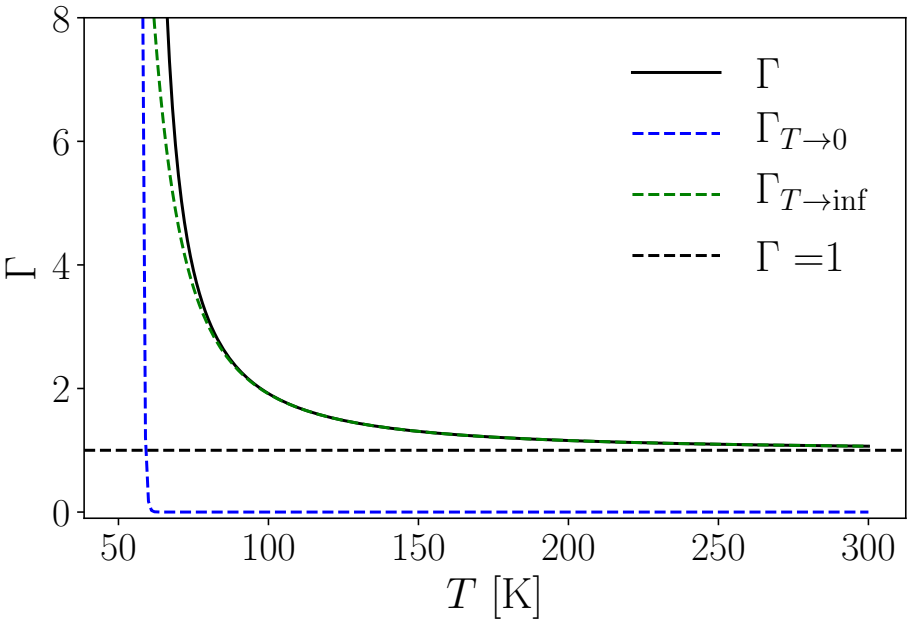

Figure 3.10: Temperature dependence of the tunneling correction factor (Γ) for Li diffusion in bulk Si. Dashed green and blue curves are high- and low-temperature limits, respectively. At high temperature, Γ converges to 1, represented by the dashed black line.

diffusion pathway. The effect is very small as tunneling effects are more prominent in the low temperature range. At high temperature, Γ converges to 1 as expected since the quantum tunneling corrections become less important and the classical barrier jump is the dominating mechanism governing the overall diffusion coefficient.

The quantum mechanical approximation for the diffusion coefficient converges to the classical limit at high temperature. It differs significantly from it only at low temperature. The effects observed in the Li-Si system are the same as for the H-metals system, however lower in magnitude. Thus, in order to clarify whether this suppression is due to the larger mass of Li or to the difference in chemistry of Li-Si, we have performed a mass rescaling analysis in the following section.

3.3.4 *Effect of mass rescaling*

In this mass rescaling analysis, the quantum mechanical effects on the diffusion coefficient were compared with the ones obtained if the lithium mass is replaced by the hydrogen mass, for which quantum effects are clearly seen even at room temperature in their diffusion in metals.

Due to such mass rescaling, there is a significant increase of the phonon frequencies of the vibrations that have a high participation ratio of the light atom (Li with H mass): the mass ratio being about seven, the vibration frequency ratio is approximately $\sqrt{7}$ for Li- dominated modes. The quantum modification of the vibrational free energy is much more pronounced as shown in Fig. 3.11. At 0 K, the classical limit is absolutely zero so the mass rescaling has no effect. For the quantum approximation, the zero-point energy slightly increases due to the scaling of frequencies and tends to the classical limit at high temperature. At high temperature, both approaches show lower values of the free energy difference due to the mass rescaling. After the mass rescaling, there is a significant quantum effect not only at room temperature but even at high temperature (near 1000 K).

The classical (and quantum) decrease of the free energy with mass rescaling is a consequence of the higher vibrational frequency of the mode along the transition path in the initial geometry. The contribution from this mode is only present in the last term of Eq. (2.70) and Eq. (2.78), i.e. in the initial point configuration. This extra mode is stretched to higher energy by the frequency ratio resulting in a higher vibrational free energy difference (ΔF^{vib}) between the initial point and the saddle point configurations. Since all three Li modes overlap with the Si modes (see Fig. 3.3 b), the latter are also affected by the mass rescaling, especially the two lateral high-frequency modes seen in Fig. 3.2 b, that are higher at the saddle point geometry than at the initial point geometry. The global qualitative picture of the mass rescaling effect at high temperature is nevertheless dominated by the removal of the phonon mode rescaled in the saddle point configuration as compared to the initial point configuration.

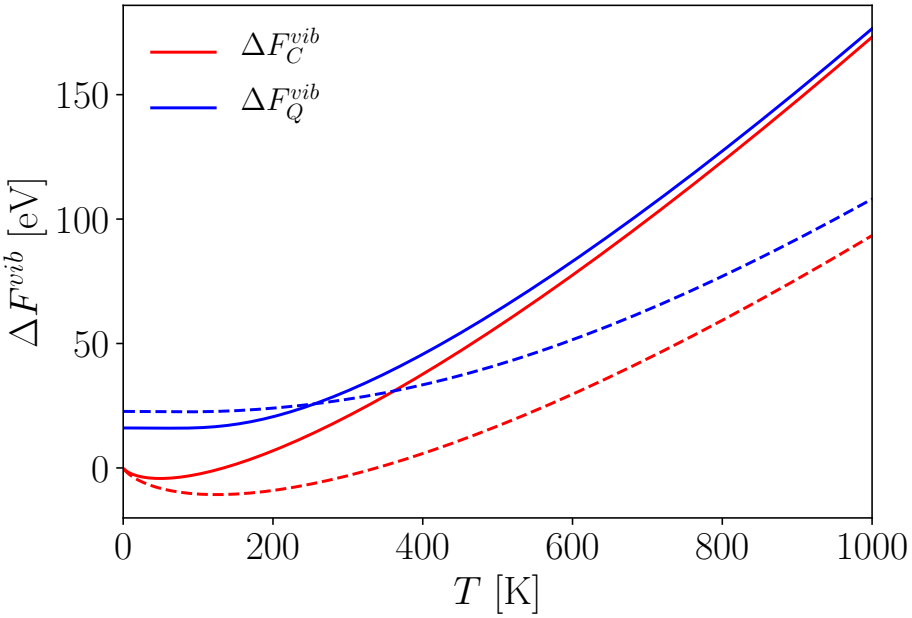

Figure 3.11: Temperature dependence of the change in vibrational free energy with classical (red) and quantum (blue) approximation, when the Li mass is replaced by the H mass (rescaling), in view of separating the mass effect from the quantum/classical effect. Solid lines show the results obtained with the unchanged mass of Li atom, dashed lines show results with the rescaled mass of the Li atom.

This increase in the phonon frequencies due to mass rescaling shifts the diffusion coefficient upwards as shown in Fig. 3.12. However, in the low temperature range, it is shifted downwards for the quantum case (D_Q) due to higher ΔF^{vib} after mass rescaling. Similar to what was obtained before mass rescaling, the quantum value after mass rescaling D_Q^r is lower than its classical counterpart D_C^r near room temperature but it increases at lower temperature as the quantum tunneling correction becomes dominant and eventually tends to flatten out surpassing D_C^r. Fermann *et al.* [120] defined this temperature as the tunneling crossover temperature (T_x) below which the quantum tunneling is dominant. According to their definition, it is the temperature where the two linear sections could hypothetically intersect,

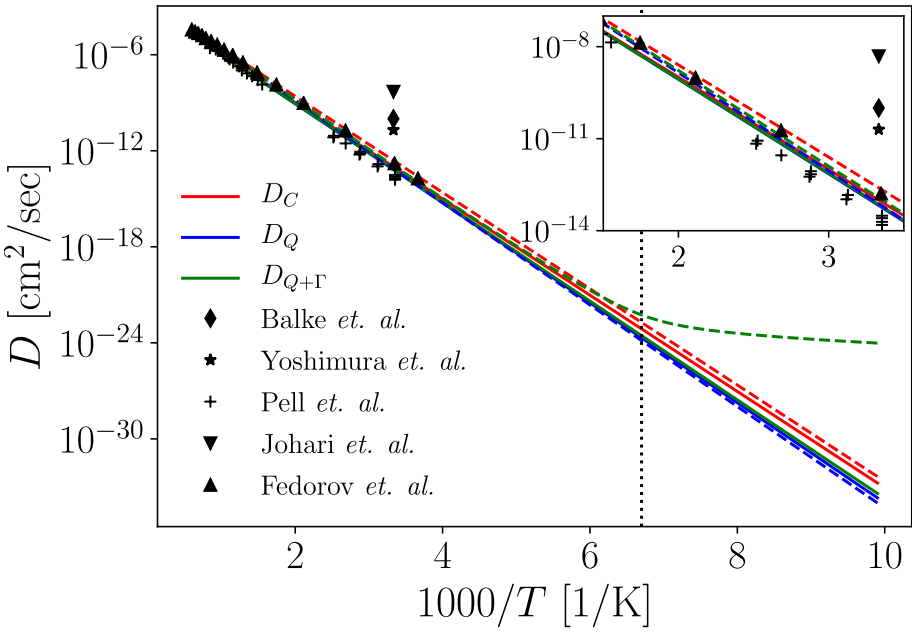

Figure 3.12: Temperature dependence of the diffusion coefficient calculated using classical (red) and quantum (blue) approximations with quantum tunneling correction (green). Mass-rescaled values (see text) are represented by dashed lines. The corresponding room temperature values are shown in the inset. The dotted line marks the tunneling crossover temperature, T_x, for the mass rescaled case. Markers represent the values reported in Ref. [63, 66, 112, 178, 207]. This crossover temperature is much lower when the mass is not rescaled, and out of the temperature range shown here.

which in the present case is ~150 K. This tunneling crossover temperature is roughly three times larger than the one before mass rescaling (~50 K).

Fig. 3.13 shows the difference between the two approaches (classical and quantum), which is obviously much more pronounced near room temperature (and at lower temperature) after mass rescaling. The ratio between the quantum and classical approximations at room temperature increases from ~30% to around 50% and 66% with ($D_{Q+\Gamma}/D_C$) and without (D_Q/D_C) tunnelling correction, respectively (see inset of Fig. 3.12). The

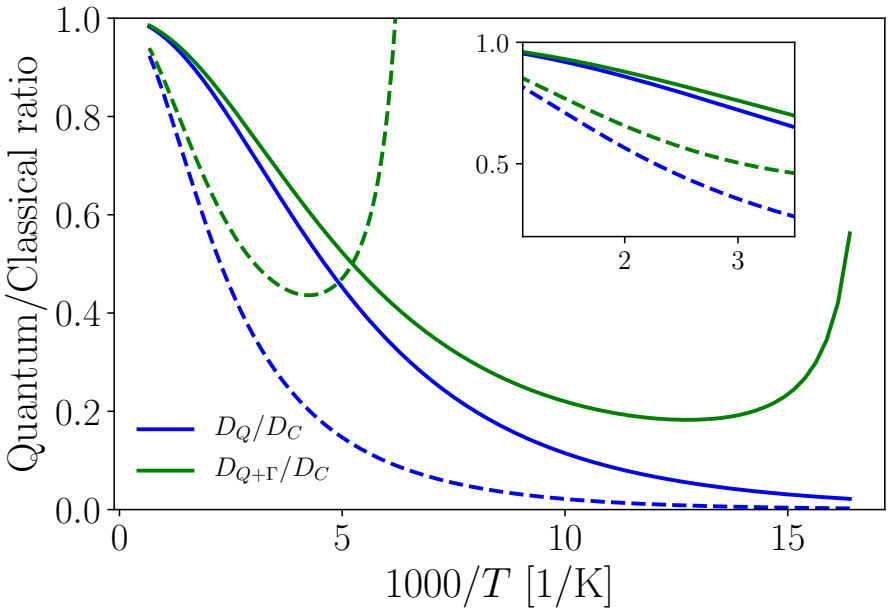

Figure 3.13: Effect of mass rescaling on quantum corrections with respect to their classical counterpart is plotted as a ratio against the inverse of the temperature (1000/T). Dashed lines represent the mass-rescaled values. Corresponding plots near room temperature are also shown in the inset.

inflection point in the $D_{Q+\Gamma}/D_C$ ratio curve represents the temperature above which tunneling corrections start becoming significant, resulting in a comparative increase of the diffusion coefficient with further lowering of temperature and eventually surpassing D_C above T_x. Moreover, the D_Q/D_C ratio shows that without this tunneling correction, the diffusion coefficient tends to o faster than its classical counterpart, which contradicts theoretical and experimental results [120].

In order to disentangle the effect of the quantum tunneling correction, the ratio of $D_{Q+\Gamma}/D_Q$ was plotted against the inverse of temperature along with the mass-rescaled one (dashed line in Fig. 3.14). After the mass rescaling, the effect of quantum tunneling corrections increases significantly: it reaches ~ 50% even near room temperature while it was less than ~7% before mass

rescaling. This analysis of mass rescaling shed light on how the heavier atomic mass of Li reduces quantum effects. However the local chemical environment might also play an important role, complementing the understanding brought by the effective activation barrier and the effective diffusion pre-factor analysis in Fig. 3.8. Note that the current approach is based on the harmonic approximation, and to go one step beyond, the next section discusses the effect of anharmonicity on the diffusion coefficient.

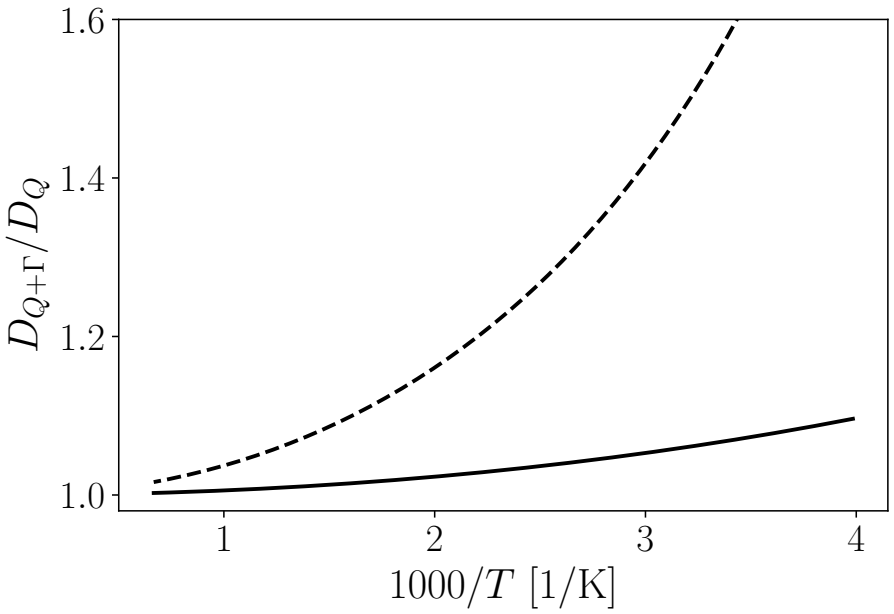

Figure 3.14: Effect of including quantum tunneling corrections on the diffusion coefficient as measured by the ratio $D_{Q+\Gamma}/D_Q$ plotted as a function of the inverse of the temperature (1000/T). Dashed lines represent the corresponding ratio after mass-rescaling.

3.3.5 *Effect of anharmonicity*

Fig. 3.15 compares the temperature dependence of the diffusion barrier ΔE calculated by the cBΩ model and the QHA along with the values obtained by NEB calculation at two dif-

ferent volumes. The diffusion barrier decreased by ~35 meV at higher volume as compared to the equilibrium volume at 0 K. The temperature associated with this volume has been obtained as 853.65 K from the V(T) curve (Appendix A). The QHA only includes the explicit volume dependence by means of thermal expansion. Thus the temperature dependence of ΔE comes from the linear interpolation of the values at 0 K and at an elevated temperature (853 K in this case) using the temperature dependence of the volume curve as outlined in Eq.(3.2).

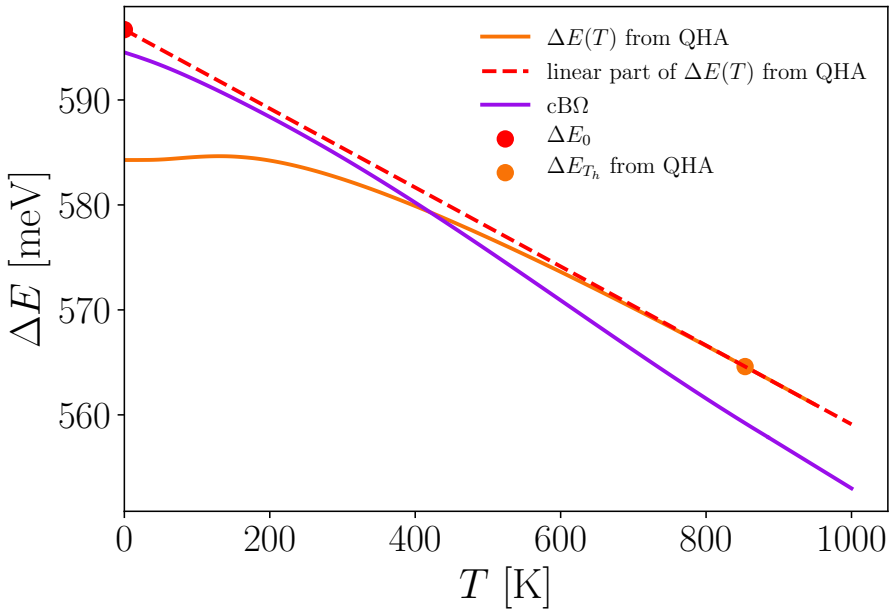

Figure 3.15: Temperature dependence of the diffusion barrier obtained from the cBΩ model (purple curve) and the QHA (orange curve). Filled circles mark the values calculated using NEB calculations and dotted line shows the linear interpolation of the high temperature limit of the QHA.

The cBΩ model includes (approximately) both the explicit volume dependence and the phonon-phonon temperature dependence by employing the temperature dependence of the volume and bulk modulus, respectively. The temperature dependence of the volume and the bulk modulus of silicon were obtained from

Ref. [71] and can be found in Appendix A. The curves (orange and purple) are adjusted for the ZPE resulting in a deviation from the value obtained at 0 K without phonon contribution (red filled circle). The cBΩ model and the QHA differ by about 10 meV in the low temperature regime, but stay within ~5-8 meV above 200K and up to 1000K, which gives some confidence that both allow us to include the dominating trend due to anharmonic effects. These energy barriers were then used to replace ΔE in Eq.(2.89) to give the overall temperature dependence of the diffusion coefficients. Fig. 3.16 shows these additional diffusion coefficient curves obtained with the cBΩ model (purple curve) and with the QHA (orange curve).

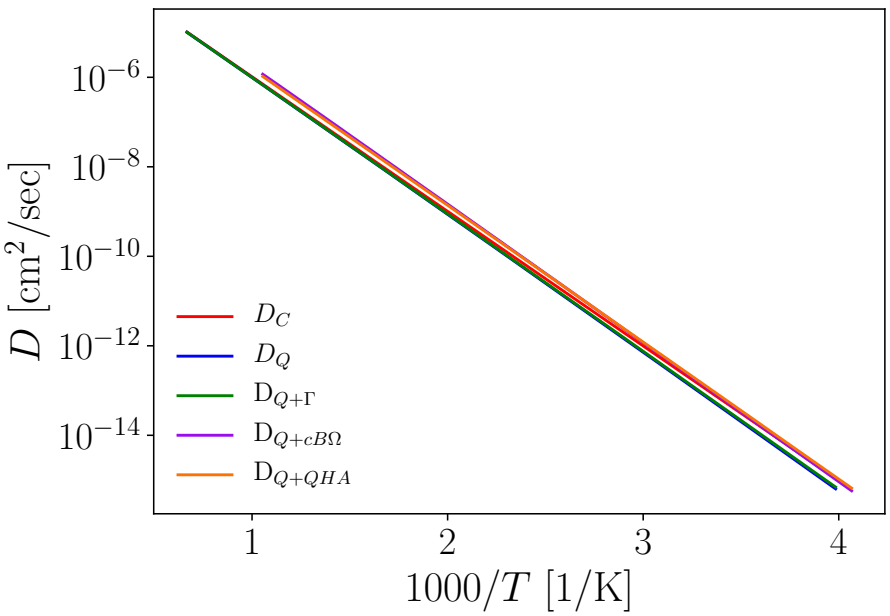

Figure 3.16: Temperature dependence of the diffusion coefficient calculated for Li in bulk Si including anharmonic effects. The orange curve shows the diffusion coefficient obtained with QHA and the purple curve represents the one obtained with the cBΩ model.

At high temperature, no severe deviation from the Arrhenius equation are observed. This suggests that the anharmonic effects

are not very strong. Though, both the approximations show a lateral shift towards higher values of the diffusion coefficient for the entire temperature range. In order to get a better comparison of the two anharmonic models, the ratio of diffusion coefficients are plotted w.r.t. to the one obtained with the harmonic approximation (Fig. 3.17).

The comparative ratios in Fig. 3.17 show roughly a 60-70% increase in the diffusion coefficient by including anharmonic effects by means of either model. This increase is more important than the one obtained by including the quantum approximation (~ 33% in Fig. 3.8). The cBΩ model suggests a shift of roughly 70% at high temperature and tends to stay constant at ~60%. While the QHA shows an initial shift of ~55%, it keeps increasing with temperature as compared to the harmonic approximation.

3.3.6 *Discussion*

The results presented in previous sections demonstrate the application of quantum mechanical framework within the TST framework to study Li diffusion in bulk Si. Moreover, the QHA and the cBΩ model provide useful insight on the validity of harmonic approximation. These results are based on several assumptions and approximations: (i) low concentration of the impurity Li atoms, i.e. there is no interaction between the impurity atoms; (ii) the diffusion process is described by the TST framework assuming every diffusing specie that reach the transition state must also cross it; (iii) there are no correlated multiple jumps; (iv) only thermally activated incoherent quantum tunneling effects are included and coherent tunneling effects are negligible in the studied temperature range; (v) assessment of anharmonic effects is limited, because they depend on the validity of the QHA and the cBΩ model; (vi) electronic energies and phonon frequencies for both the ground state and the transition state has been obtained from DFT with GGA-PBE functional.

Within the framework of these approximations, several effects have been analyzed to estimate the sensitivity of the results, namely (i) the effect of quantum mechanical approximation;

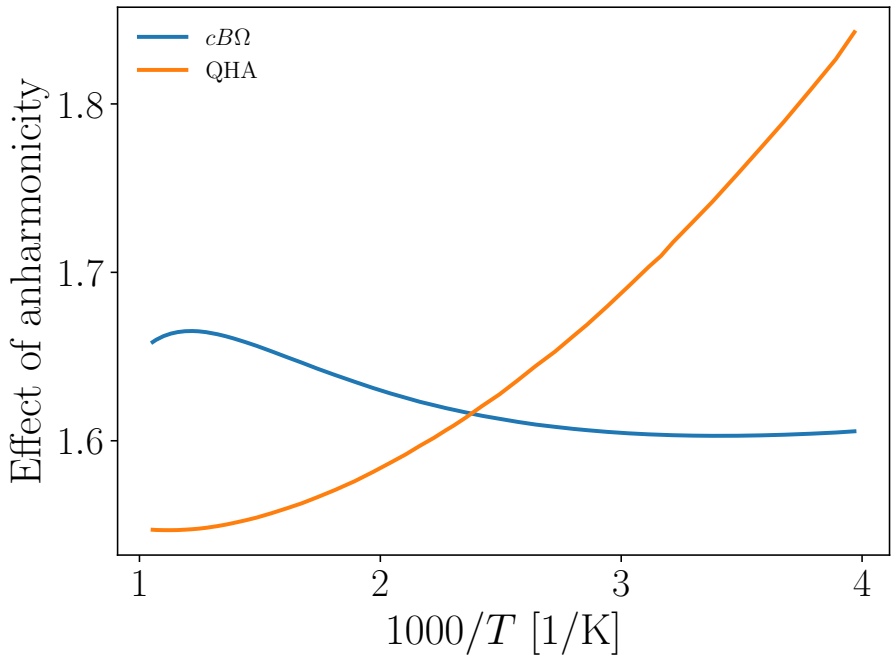

Figure 3.17: Temperature dependence of the effect of anharmonicity on the diffusion coefficient measured as a ratio of the diffusion coefficient obtained with the cBΩ model (violet) and the QHA (orange) w.r.t. the one obtained with the harmonic approximation (D_Q).

(ii) the effect of quantum tunneling corrections; (iii) the effect of mass rescaling; and (iv) the effect of anharmonicity. The analysis shows that the diffusivity of Li in bulk-Si decreases by roughly 30% by including quantum mechanical approximation as compared to the classical TST framework.

The decrease in the diffusion coefficient is in agreement with the increase in the effective diffusion barrier as compared to the classical one (refer Fig. 3.8). On the other hand, the pre-exponential factor (D^*_{QA}) is slightly higher than the classical one. Globally, the increase in the barrier height dominates and lowers the overall diffusion coefficient as expected in an Arrhenius type equation. The effective diffusion barrier written in Eq. (2.87) is another form of Eq. (2.63) that relates the diffusion barrier to the

change in the vibrational free energy ΔF^{vib} and a temperature independent term ΔE. Therefore, a higher value of ΔF_Q^{vib} than its classical counterpart increases the diffusion barrier and results in a lower diffusion coefficient. The value of ΔF_Q^{vib} at 0 K corresponds to the ZPE and converges to its classical limit (ΔF_C^{vib}) at high temperature. However, it is different than simply adding the ZPE to the classical equation because a simple shift rectifies the low temperature limit but overestimates the high temperature limit [68, 208].

The solubility of Li in Si is very low at room temperature [192, 209], which justifies the assumption of low concentration of the diffusing Li atom. Moreover, unless two Li atoms are in the adjacent tetrahedral void (<6 Å apart), there is no effect on the diffusion barrier [206]. Thus with a supercell with lattice parameters >10 Å, it is safe to assume no interaction between Li atoms in the adjacent cells.

Now we turn to the discussion of the TST framework for studying diffusion. In the original work of Eyring [114], a factor c accounts for the recrossing when the activated complex jumps over the barrier and comes back to the initial state without decomposing. This factor is known as the dynamical-correction factor in the literature and decreases the overall diffusion coefficient. It was implicitly set as 1 by Eyring [114], and later some researchers have investigated this correction factor and discussed the complexity in estimating its value [210, 211]. However, in most of the diffusion studies, it is considered a good assumption to neglect any recrossing, i.e. $c = 1$ is a reasonable approximation [179, 187].

The correlation factor (f) associated with the correlation in multiple jumps is another factor, which is not considered in the present work. The value of this correlation factor is $\leqslant 1$ and depends on the diffusion mechanism and lattice geometry [67]. Thus, if these correlations are present, it will decrease the diffusion coefficient. Blöch *et al.* [212] have showed that this factor is negligible for H diffusion in Si. Moreover, in case of dilute interstitial diffusion (as in the present case), the diffusing atom does not have an interaction from a neighboring interstitial atom and

thus there is no correlation between multiple jumps resulting in $f = 1$ [67]. Thus we can neglect the correlation factor in this case without any loss of generality.

Quantum tunneling corrections have been included only by the means of thermally activated incoherent tunneling mechanisms. The coherent tunneling is only active at a very low temperature, near 0 K, and thus has never been observed experimentally, even for hydrogen diffusion [213, 214]. Thus, it is safe to neglect it in the temperature range of interest, between 50 K to high temperature.

The only remaining concern is the validation of harmonic approximation and the applicability of models used to estimate the anharmonicity in the system. With either of the models, the diffusion coefficient increases by 60-70% as compared to the harmonic approximation. This effect is roughly double than the one observed after including the quantum mechanical effects, which decreased the diffusion coefficient by ~30%. Regarding the accuracy, the QHA estimation of the diffusion constant depends on the precision of NEB calculations and the volume curve. The former was converged till the average energy tolerance was $\leqslant 1 \times 10^{-5}$ Ha (~27 meV) and the latter had a very good agreement with the experimental data [71]. The cBΩ model has an additional dependence of bulk modulus, which is a second-order derivative of the volume and can be sensitive to small errors in the volume curve. The literature [127, 186] suggests to fit the factor c to the experimental data. However in the present work, the energy barrier calculated at 0 K is used to adjust c to avoid any accumulation of fitting error. Although it shows a reasonable agreement with the QHA as well as the 0 K NEB result (Fig. 3.15), it is a simplistic model incorporating both the V and the T dependency without including the phonon-phonon interaction, which might be important at high temperature.

The GGA-PBE functional that has been used for all the computations slightly overestimates the lattice parameter by <0.7% and shows a very good agreement with the experimental data for the total energy as well as phonon calculations for silicon [139].

In the future, one could perform a comparative study of diffusion coefficients calculated with different functionals.

3.4 LI DIFFUSION IN LISI

3.4.1 *Bulk LiSi and Li vacancy effect*

Li diffusion in Li_xSi is at least one order of magnitude faster than in bulk Si [62]. LiSi is the first stable crystalline phase in terms of increasing Li:Si ratio and has a higher symmetry (space group: $I4_1/a$) than other Li_xSi phases, with a regular Si network. Three-fold coordinated Si atoms form rings of 8 atoms (S8) as shown by Evers. *et al.* [215] and Li atoms occupy the voids in the chain as shown in Fig. 3.18. The Si and Li sublattices are topologically equivalent, forming tetrahedral clusters. The presence of Li atoms distorts the Si network and the Si-Si bond distance increases from 2.368 Å in bulk Si to 2.418 Å and 2.497 Å which is in good agreement with the previous first-principles calculations [129] and the experimental data [194, 215]. The primitive cell of LiSi consists of 8 Si and 8 Li atoms where each Si atom gets one electron from the Li atom to satisfy the octet rule [31]. The calculated lattice parameters of the fully relaxed primitive LiSi structure studied in this work are: $a = b = c = 14.40$ Å, with the angles $\alpha = \beta = 99.15°$ and $\gamma = 133°$. The conventional standard structure contains 16 Si and 16 Li atoms with the lattice parameters: $a = b = 9.367$ Å, $c = 5.743$ Å with the angles $\alpha = \beta = \gamma = 90.00°$, which is in good agreement with the experimental XRD data ($a = b = 9.354$ Å, $c = 5.746$ Å) reported by Stearns *et al.* [194].

Four Li atoms in LiSi structure form a slightly distorted tetrahedron with Li-Li bond distance of 2.935 Å and 2.944 Å. Each Li atom in this tetrahedral network is connected to three other Li atoms within the same tetrahedra and to three Li atoms (from two other tetrahedra) by three paths (see Fig. 3.18): one at a distance of 2.683 Å and the other two at a distance of 3.052 Å (one in each tetrahedron). In total, each Li atom is connected to 6 Li atoms: 3 Li atoms within the same tetrahedron and 3 Li atoms

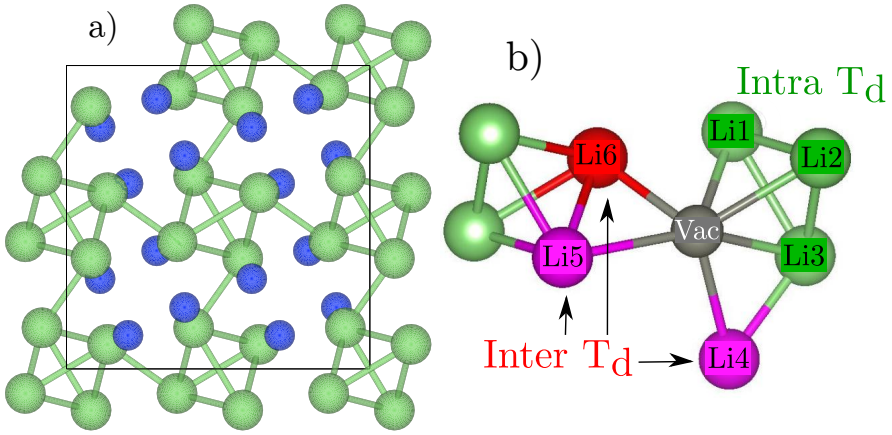

Figure 3.18: a) Conventional unit cell (32 atoms) of LiSi structure, showing three-fold coordinated Si and tetrahedral Li clusters (Si atoms in blue, Li atoms in green). b) Zoomed in image of the same structure centered on one Li vacancy and showing possible jumps to the neighboring Li atoms. Green jumps are intra-tetrahedral jumps and pink/red are inter-tetrahedral jumps.

from other tetrahedra, which is consistent with the experimental data [215].

A previous study by Moon *et al.* [129] has shown that vacancy diffusion is the most energetically favorable mechanism for Li diffusion in LiSi. Since all Wyckoff sites of Li atoms are identical, any Li atom can be removed to create a Li vacancy without loosing generality. After removing one Li atom, the volume decreases slightly and the lattice parameter reduces to 14.392 Å (i.e. a decrease of ~0.05%) and angles remain unchanged. The vacancy formation energy for this supercell, calculated with:

$$E_v = E_{N-1} - \frac{N-1}{N} E_N \tag{3.3}$$

was 1.51 eV, which is in good agreement with the previous theoretically reported value of 1.2 eV. The energy terms E_{N-1} and E_N in Eq. 3.3 represents the total energy of the system with and

without 1 Li atom vacancy, respectively, and N is the total number of atoms present in the starting structure. Similar to the addition of 1 Li atom in bulk Si, the removal of 1 Li atom from LiSi does not affect much the valence band, except for the removal of two 1s core electrons. The peaks in the conduction band change due to the removal of the 2s electron. Accordingly, in a 16-atom primitive cell, removing a Li atom yield a Fermi energy decrease by 0.62 eV and consequently moves it to the valence band as shown in Fig. 3.19. In the next section, different types of possible vacancy jumps have been studied for calculating the diffusion coefficient.

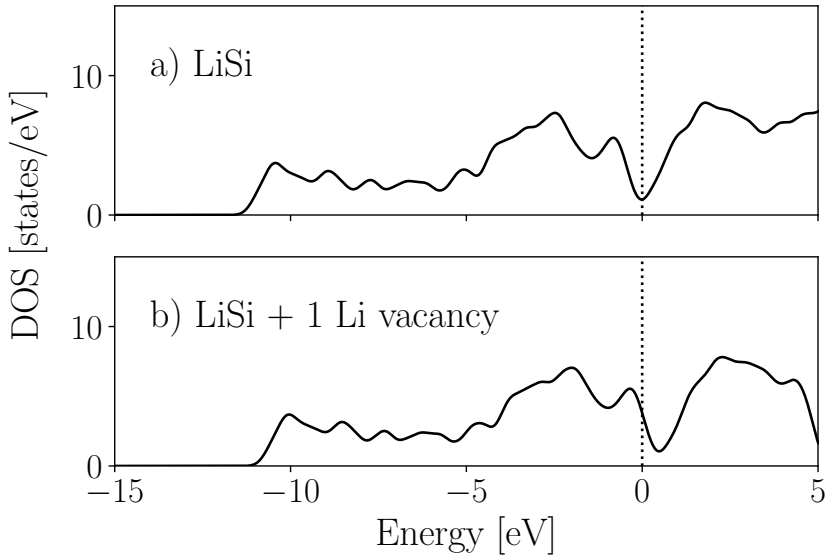

Figure 3.19: Electronic density of states of a) primitive LiSi cell (16 atoms) with b) one Li vacancy. The Fermi energy is set to zero on the x-axis (dotted line). These small-cell results are shown for illustration purpose only.

3.4.2 *Migration path and energy barrier*

As discussed above, each Li atom can jump to 6 neighboring Li sites within a radial distance of 3.5 Å. Beyond this distance, the

calculated migration barriers are very high (>1 eV), and thus will have a negligible contribution in Li diffusion [129]. Out of these 6 jumps, there are 3 intra-T_d jumps (Vac-Li1, Vac-Li2, Vac-Li3) and 3 inter-T_d ones (Vac-Li4, Vac-Li5, Vac-Li6) (see Fig. 3.18b). Out of them, there are 2 pairs of identical jumps: Vac to Li4 and Li5 and Vac to Li1 and Li3 jumps and remaining two unique jumps from Vac to Li6 and Vac to Li2, leaving a total of 4 different types of jumps. The convergence study with respect to the size of the cells was conducted on supercells of size 32 atoms (*c*-LiSi), 64 atoms (2×1×1 of *c*-LiSi), and 128 atoms (2×2×2 of *p*-LiSi) for individual energy barriers and the overall diffusion coefficient calculated by KMC simulations (see Figs. A.2 and A.3 in Appendix A). Although the 64-atom cell was well converged, the biggest supercell of 128 atoms was used in the study for better accuracy. Table 3.1 outlines the calculated jump distances and the migration energy barriers for these 4 types of jumps along with the first-principles calculations of Ref. [129]. Fig. 3.20 shows the corresponding energy profiles. The agreement is very reasonable given that the present study relies on GGA while Ref. [129] uses the local density approximation (LDA), which is known to underestimate the lattice parameters and hence Li-Li distances.

Table 3.1: Calculated Li migration jump distances and energy barriers compared with the values reported in literature [129].

Jump	Distance(Å)		E_b(eV)	
	This work	Ref. [17]	This work	Ref. [17]
Vac-Li1	2.935	2.900	0.247	0.252
Vac-Li2	2.944	2.911	0.261	0.235
Vac-Li4	3.056	3.003	0.430	0.466
Vac-Li6	2.695	2.644	0.252	0.272

The two types of pathways connecting different tetrahedra are Vac-Li4 and Vac-Li6 with energy barriers of 0.430 and 0.252 eV, respectively. In order for Li atoms to diffuse in the LiSi structure, they have to go through one of these inter-tetrahedral paths, therefore these jumps are rate-limiting. Comparing both energy barriers, the latter is roughly half of the former and thus it is

more likely to control the effective Li diffusion at room temperature and above.

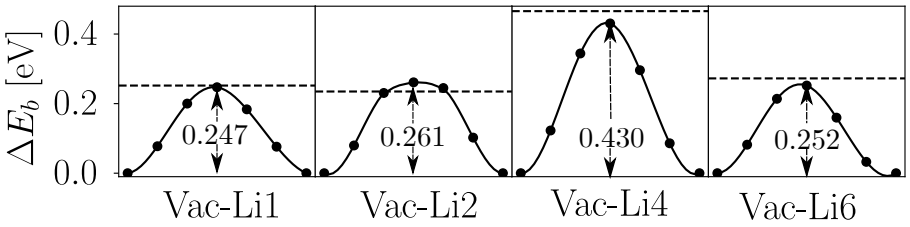

Figure 3.20: Minimum energy paths for lithium vacancy diffusion for four types of jumps. The energy barrier height is indicated by the peak height inside the graph (in eV). (Refer to Fig. 3.18 and Table 3.1 for the nomenclature associated with the type of jump). The horizontal dashed line indicates the value reported in Ref. [129]

3.4.3 *Phonon calculations*

Fig. 3.21 shows the vibrational energy calculated from phonon frequencies at the initial and saddle point configurations with the quantum and the classical approximations using Eqs. (2.78) and (2.70), respectively. As noticed in bulk Si case, the ZPE correction due to quantum approximation is small and only significant below room temperature. The classical vibrational free energy (F_C^{vib}) goes to zero at 0 K as shown in Eq. (3.4), and the limit of the quantum vibrational free energy (F_Q^{vib}) has a finite value as shown in Eq. (3.5):

$$\begin{aligned} \lim_{T\to 0} F_C^{vib} &= \lim_{T\to 0} kT \sum_i \ln\left(\frac{h\nu_i}{kT}\right) = 0, \\ \lim_{T\to 0} \Delta F_C^{vib} &= 0, \\ \lim_{T\to 0} F_Q^{vib} &= \sum_i \left(\frac{h\nu_i}{2}\right), \end{aligned} \tag{3.4}$$

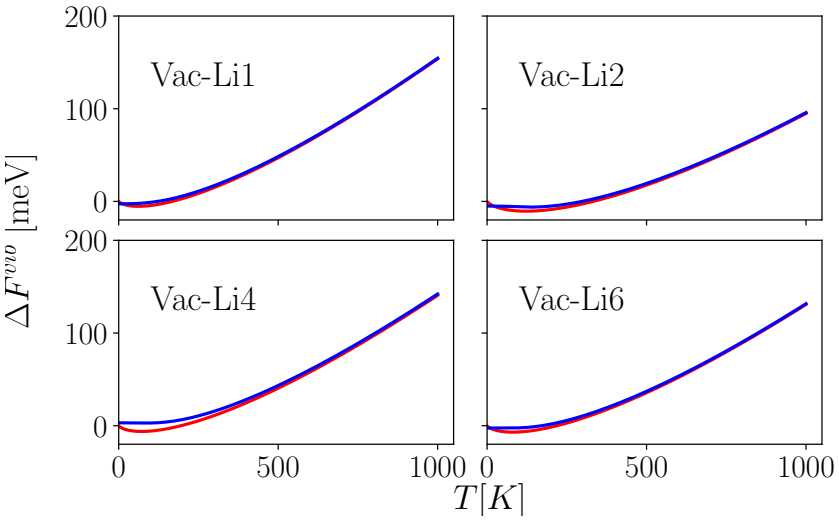

Figure 3.21: Temperature dependence of the vibrational free energy for different types of vacancy jumps (refer Fig. 3.18 for nomenclature). The red and blue curves indicate the results obtained using the classical and quantum approximations, respectively.

$$\lim_{T\to 0} \Delta F_Q^{vib} = \sum_i^{N-1} \left(\frac{h\nu_i^S}{2}\right) - \sum_i^{N} \left(\frac{h\nu_i^0}{2}\right). \tag{3.5}$$

Instead of only one type of jump in the case of bulk Si, there are six possible vacancy jumps in LiSi. Consequenty, there will be six diffusion equations, one for each corresponding jump and thus the overall diffusion coefficient of Li in LiSi can not be computed directly. Therefore, a KMC simulation is used to estimate the effective diffusion coefficient due to all these jumps using the DFT data (refer Chapter 2 for more details about KMC method).

3.4.4 *Effective diffusion coefficient: KMC*

KMC simulations were performed on a conventional LiSi lattice with a single Li vacancy through which Li atoms will dif-

fuse with the above calculated energy barriers. The diffusion coefficient for each one of the six jumps was calculated with the quantum and the classical approximations using Eqs. (2.83) and (2.84). Similar to bulk Si, the quantum tunneling correction shows a very small effect on the diffusion coefficient near room temperature. The ratio of $D_{Q+\Gamma}/D_Q$ for all four jumps (Fig. A.4 in Appendix A) is less than 1.05 (i.e. less than 5% change) near room temperature and it increases for lower temperature. But unlike bulk Si, the overall diffusion coefficient of Li in LiSi is calculated at discrete temperature values which are at or above room temperature. Moreover, we have already seen in section (3.3.4) that the heavy mass of Li, as compared to H, significantly diminishes the quantum effect. Thus, it was safe to ignore the quantum tunneling corrections in the KMC study for the LiSi case.

Fig. 3.22 shows the distribution of the diffusion coefficients D_i obtained from KMC simulations at different temperature from 40,000 sites with 10,000 steps each, based on the jump rates determined from the classical approximation. Because the selection of an event in the KMC algorithm gives a Poisson's distribution [130], we also show a Poisson distribution fit (red curve) as a guide for the eyes. The good agreement between the distribution obtained from the KMC study (histograms) and the Poisson fit (red curve) suggests that the KMC simulations provide sufficiently converged results.

The effective diffusion coefficient of this distribution has been calculated by using Eq. (2.101) as suggested in Refs. [130, 134]. Similarly an effective diffusion coefficient was also calculated based on the jump rate calculated from the quantum approximation. Fig. 3.23 shows the Arrhenius fit for these values obtained for the classical and quantum approximations, and a comparison with the experimental data [62] and previous KMC simulations performed by Moon *et al.* [129]. Due to the scarcity of experimental data for the LiSi phase, the diffusion data from Wen *et al.* [62] on other Li_xSi phases was used as a rough estimate for the diffusion of Li in LiSi, Moon *et al.* [129] also used the same reference.

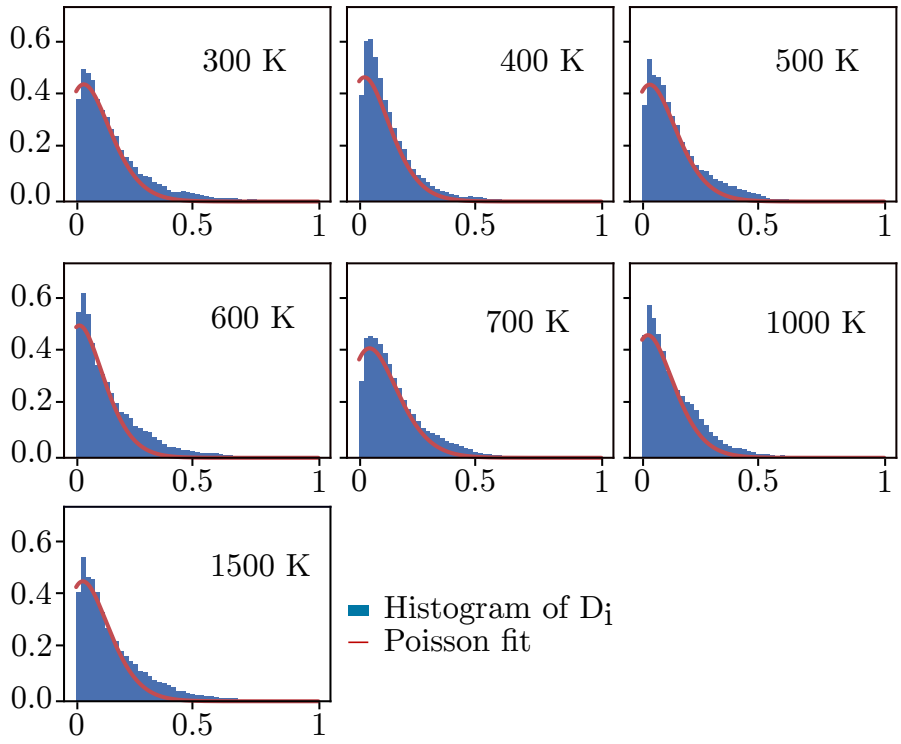

Figure 3.22: Statistics showing the distribution of the diffusion coefficients (D_i for each of the 40,000 runs) obtained from KMC simulation for each temperature. The solid line (red) is obtained by fitting a Poisson distribution. The data is normalized ($|D_i| = D_i/\max(D_i)$) and binned into 50 bins for curve fitting over the distribution. The y-axis represents the probability of the Poisson distribution.

The diffusion coefficients obtained from both approximations provide a good fit for the Arrhenius equation with an effective barrier of 0.27 eV and a diffusion pre-factor of $2.81 \pm 0.5 \times 10^{-5}\,cm^2/s$. Quantum effects have a marginal role in the diffusion coefficient of Li in LiSi, providing the same diffusion barrier of 0.27 eV and a prefactor of $3.14 \times 10^{-5}\,cm^2/s$. The diffusion coefficients obtained from both approximations are in close agreement with the experimental data [62] at 700 K. The filled markers in the plot represent other theoretical values of the diffusion coefficients obtained from *ab-initio* molecular dynamics studies at high temperature.

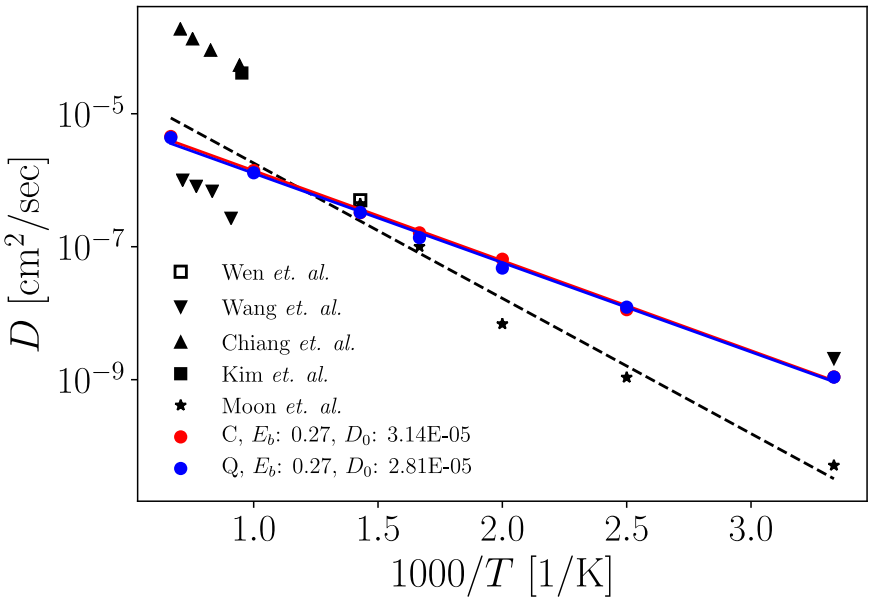

Figure 3.23: Temperature dependence of the effective diffusion coefficient (D) obtained from KMC simulation. Dots in red and blue indicate values obtained with classical and quantum approximations of attempt frequencies, respectively. Solid lines show the fitted Arrhenius plot to get the effective pre-factor and the effective energy barrier. Experimental data point is shown by the empty square (black) and results from previous theoretical investigations [62, 129, 174, 176, 177] are indicated by filled markers (black).

3.4.5 *Effect of anharmonicity*

Similar to the bulk Si case, the effect of anharmonicity on the diffusion of Li in LiSi is studied by the means of QHA and the cBΩ model using the temperature-dependent volume and bulk modulus. Figs. 3.24 and 3.25 show these quantities calculated from first principles.

Because of the slow kinetics of formation, the LiSi phase is difficult to form at room temperature and normal pressure (NP) and thus, there are limited experimental data on its structural properties [192, 194]. Stearns *et al.* [194] have synthesized c-LiSi

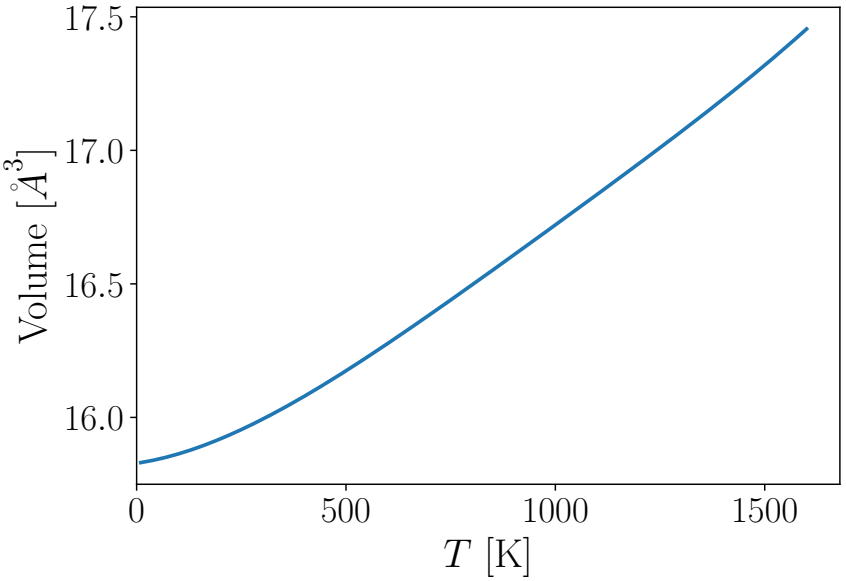

Figure 3.24: Temperature dependence of the LiSi primitive volume from first principles.

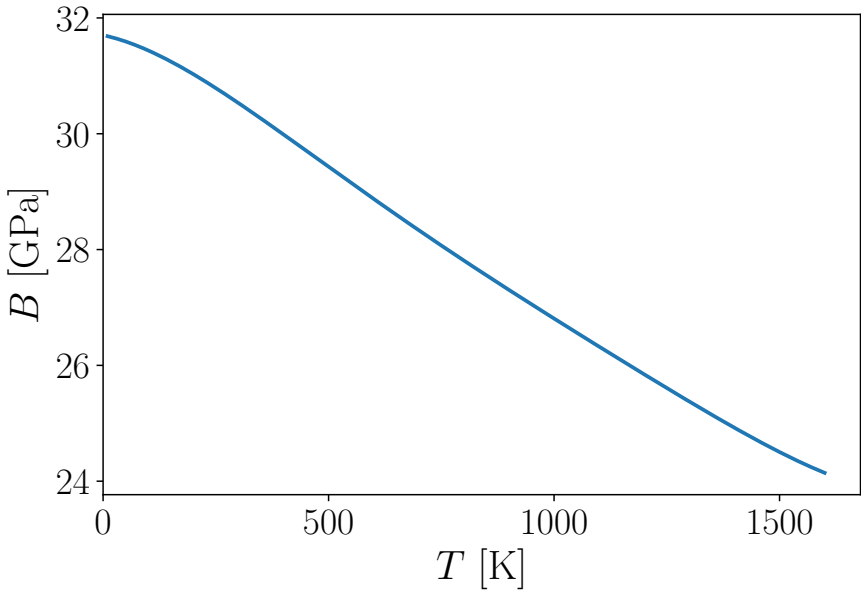

Figure 3.25: Temperature dependence of the LiSi bulk modulus from first principles.

in laboratory at high temperature and high pressure (HP), and reported a volume of 15.75 $Å^3$/atom from X-ray diffraction data by Rietveld refinement. Our zero point corrected volume at zero temperature (15.83 $Å^3$/atom) is 0.08 $Å^3$/atom higher than their value as shown in Fig. 3.24. At the time of writing we are not aware of any experimental data for elastic properties of c-LiSi phase.

A previous DFT (with the LDA functional) calculation by Taubert *et al.* [216] has reported a value of 56.8 GPa for the bulk modulus of LiSi at zero temperature. This is roughly 55% higher than our calculated value of 32 GPa shown in Fig. 3.25. There is a well-established general tendency of GGA-PBE to underestimate the bulk modulus [138], while LDA can present errors of both signs, i.e. higher as well as lower [139].

Fig. 3.26 shows the temperature dependence of the diffusion barriers for all four types of vacancy jumps calculated with the cBΩ model and the QHA according to Eqs. 2.95 and 3.2, respectively. The cBΩ model shows the same overall trend for all the four jumps as expected. The temperature varying ingredient, the volume per unit atom (Ω) and the bulk modulus, remains the same for all the four types of jumps, and thus resulting in the same curve scaled to a different energy level corresponding to each jump.

The overall decreasing trend is due to the lattice softening with the thermal expansion, which in most cases decreases the diffusion barrier. This ability of cBΩ model to incorporate the anharmonic effects in a simple model by the means of volume and bulk modulus makes it a promising approach to study anharmonicity and has shown good results in studying diffusion in several semiconductors and metal oxides [190]. However, in the case of the Vac-Li1 jump, according to the QHA, the diffusion barrier increases with temperature. Thus in this case, the cBΩ model and the QHA approach disagree. The QHA uses an additional information about the diffusion barrier at an elevated temperature (920 K in this case) and thus it treats more accurately the volume dependence, but the lack of treatment of the phonon-phonon interaction prevents us to conclude it is better

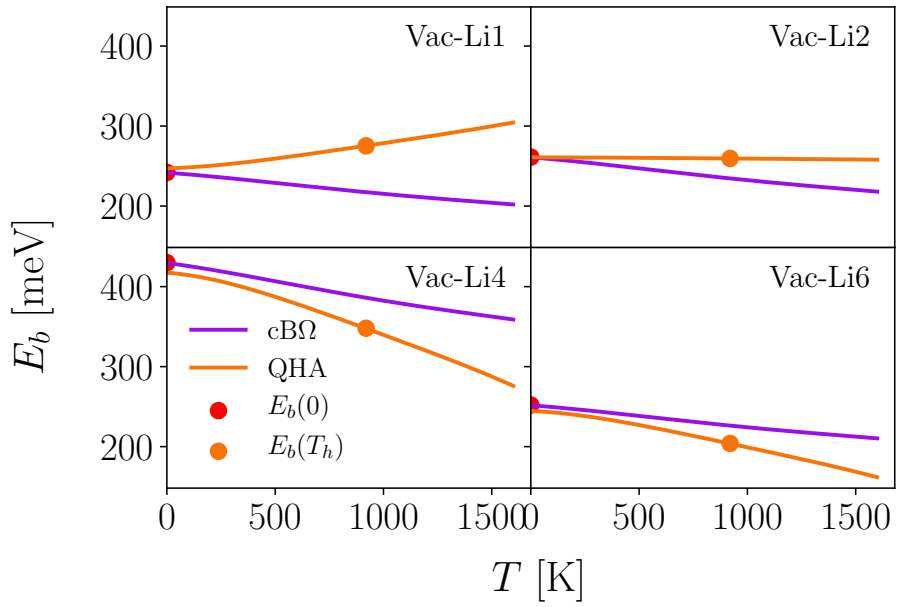

Figure 3.26: Temperature dependence of the diffusion energy barrier calculated with the cBΩ model (violet) and with the QHA (orange) for all the 4 jumps. Red and orange dots are the values obtained from NEB calculations at 0 K and 920 K, respectively.

than the cBΩ model. We can simply note that while both approaches agree on the decrease of the barrier energy with temperature for three out of four types of jump, they disagree for the Vac-Li1 jump. Similar to what was done in the harmonic approximation, the KMC simulation was used to calculate the effective diffusion coefficient for Li vacancy jump for both these models to study the anharmonic effects.

Fig. 3.27 shows the effective diffusion coefficients obtained with the KMC simulation at discrete temperatures using the individual vacancy diffusion coefficient calculated with the cBΩ model (violet) and the QHA (orange). The individual points fit very well with the Arrhenius equation with a R^2 value of 0.99 in all the cases. The corresponding values of diffusion pre-factor D_0 and the diffusion barrier E_b are within an error range of

$\pm 0.6 \times 10^{-5}$ and ± 0.01 eV, respectively. The diffusion coefficient obtained from the cBΩ model shows a similar curve as the harmonic approximation. Although the QHA shows a slightly lower value of the diffusion coefficient, the difference is within the error limits of the KMC simulation.

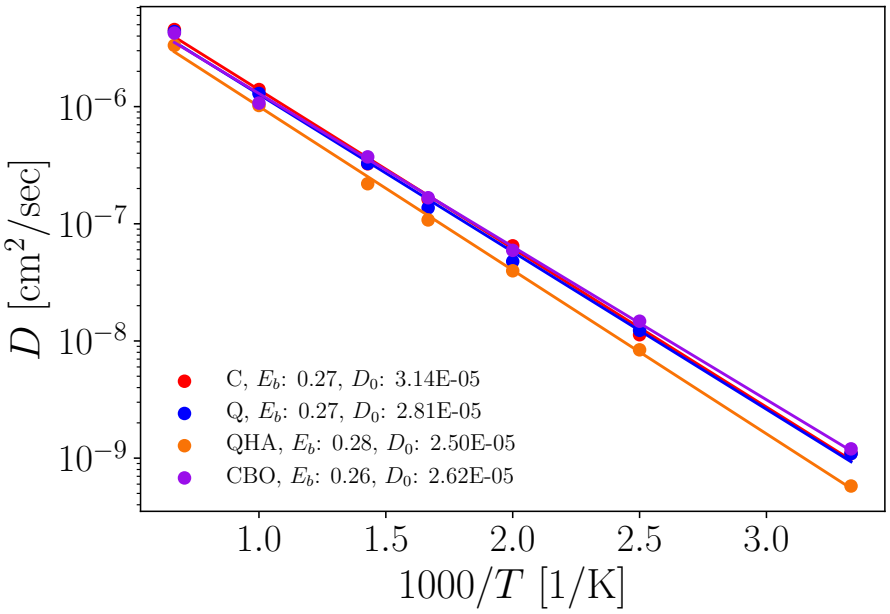

Figure 3.27: Temperature dependence of the Li diffusion coefficient in LiSi obtained from the KMC simulations. The harmonic classical (red) and quantum (blue) approximations are plotted along with the cBΩ model (violet) and with the QHA (orange) to study anharmonicity in the system. The error (variance) in the values of E_b and D_0 are ± 0.01 eV and $\pm 0.6 \times 10^{-5}$, respectively.

In order to have a better comparison, the effective diffusion coefficients from both the approximations are plotted in Fig. 3.28 as a ratio with respect to the harmonic approximation with quantum mechanical corrections (D_Q). The effect of quantum mechanical corrections are also plotted on the secondary axis as ratio of D_Q vs D_C for comparison.

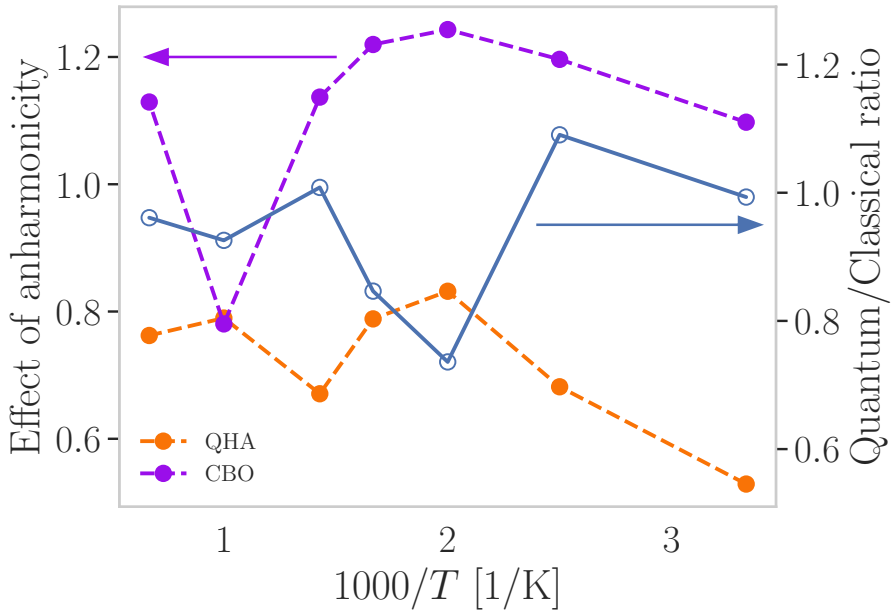

Figure 3.28: The effect of anharmonicity is shown as a ratio of the diffusion coefficient obtained with the QHA (orange) and the cBΩ model (violet) with respect to the one obtained with the harmonic approximation (D_Q) at each temperature using KMC. The ratio of D_Q/D_C is also plotted on the secondary axis with the same scale for comparison.

3.4.6 *Discussion*

In this subsection, all the results obtained for Li diffusion in LiSi via the vacancy mechanism are discussed and compared with the reported literature. The values of the effective diffusion coefficient obtained in the KMC study is in good agreement with the experimental data at 700 K [62] (see Fig. 3.23). In a previous KMC study, Moon *et al.* [129] also reported a similar value at 700 K. However, their low temperature diffusivity values are at least one order of magnitude smaller than our results. The least square fit of their reported values gives an effective barrier of 0.40 eV. Nonetheless, they reported an effective barrier of 0.306 eV for Li diffusion in LiSi, which is close to the value obtained in our study (0.27±0.01 eV). Moreover, an effective barrier

of 0.40 eV is much higher than the smallest inter T_d barrier of 0.27 eV and close to the higher energy inter T_d jumps (0.47 eV) (refer Table 3.1). These high energy jumps are unlikely to contribute significantly at room temperature and thus the effective barrier should be close to the smallest one and not to the largest one. The discrepancy can be due to insufficient statistics of the KMC calculation and error bars.

AIMD studies conducted by Chiang *et al.* [176] reported a higher diffusion coefficient (filled triangle) of the order of $10^{-4}cm^2/s$ with an effective barrier of 0.38 eV in the high temperature range. It is one order of magnitude higher than the values obtained in this study. Their extrapolated value at 700 K is also roughly an order of magnitude higher than the experimental data. A similar AIMD study by Kim *et al.* [177] (filled square) also showed a similar value of diffusion coefficient at 1050 K. However, both these studies were performed with liquid LiSi phase, in which diffusion is expected to be slightly higher than the corresponding solid phase. Thus, the room temperature extrapolation is not an accurate description of diffusion in the c-LiSi phase.

In another study, Wang *et al.* [174] calculated the Li diffusion coefficient (upside down filled triangle) during lithiation of Si to form LiSi in a similar temperature range. However, unlike Chiang *et al.* [176], they started with the room-temperature structure of solid Si to form LiSi instead of a liquid/amorphous one. Their reported values are in a better agreement with the experimental data and their room temperature value is also in close agreement with our results. The discrepancy in the above mentioned two sets of AIMD studies carried out in a similar temperature range shows roughly a difference of 2 orders of magnitude between the solid and liquid LiSi phase and thus one has to be careful about the phase while doing the AIMD studies at elevated temperatures.

Regarding the validation of the harmonic approximation in LiSi case (refer Fig. 3.28), both approximations (cBΩ model and QHA), separate at high temperature (except at 1000 K). For instance the cBΩ model increases the diffusion coefficient, while the QHA decreases it. The divergence in the two approxima-

tions might be due to the discrepancy in the estimated diffusion barrier for one of the four inter-tetrahedral jumps (Vac-Li1) as shown in Fig. 3.26. Additionally, the QHA can underestimate the anharmonicity as it does not include the phonon-phonon interaction that can play a significant role at high temperature [72, 126]. Although, in the low temperature range, the overall trend from both the approximations shows an increase in the diffusion coefficient with an increase in temperature, none of them provide a convincing proof of having significant anharmonic effects on the diffusion of Li in LiSi.

3.5 CONCLUSION

In this study, we have performed a first-principles-based study of Li diffusion in bulk Si and c-LiSi phase, within the transition state theory framework and also taking into account nuclear quantum approximations and anharmonic effects. As compared to the classical approach, the addition of quantum effects for Li diffusion in Si lowers the value of the room temperature diffusion coefficient by 33% because of a higher effective energy barrier. The cBΩ model and the quasi-harmonic approximation suggest an increase in the diffusion coefficient by 60% in case of bulk Si by including anharmonic effects. However, they fail to give a compelling evidence of the sign of the anharmonicity effect in case of LiSi.

The obtained results are in good agreement with previous experimental and theoretical studies. For Li diffusion in bulk Si, we obtained an energy barrier of 0.59 eV with a diffusion pre-factor of $1\times10^{-3}\text{cm}^2/\text{s}$. In the case of LiSi, our calculations are in better agreement with the experimental data than previous *ab-initio* molecular dynamics studies conducted at higher temperatures. We obtained an effective diffusion barrier of 0.27 ± 0.01 eV with a pre-factor of $2.8\pm1.1\times10^{-5}\text{cm}^2/\text{sec}$ for Li diffusion in LiSi. Closeness in results with both classical and quantum approximations suggests that quantum approximations only play a marginal role for Li diffusion in LiSi. Moreover, we propose that one

of the inter tetrahedral jump with an energy barrier of 0.25 eV is the rate limiting step for long range Li diffusion in LiSi.

The main advantages of using the current approach over molecular dynamics are: 1) unlike molecular dynamics, this approach can be used for slow diffusion processes near room temperature; 2) it gives a better understanding of the different diffusion mechanisms involved and thus it is helpful in designing new materials with the desired diffusion properties. This makes it a potential approach in studying even more complex systems, for instance Li diffusion in lithiated Li_xSi phases with defects. Based on our results, this approach can be used in studying room temperature Li diffusion in different anode materials and can possibly increase our understanding in designing next-generation batteries.

4

DELITHIATION OF C-$LI_{13}SI_4$ BY FIRST-PRINCIPLES

This chapter outlines a novel first-principles based delithiation scheme tested for the delithiation of c-$Li_{13}Si_4$.

4.1 INTRODUCTION

The process of delithiation with respect to LIB anodes refers to the removal of Li^+-ions from the anode. These Li^+-ions diffusing through the electrolyte combine with electrons at the cathode (discharging of a battery). Though it seems reverse of the lithiation (charging) process, it is not. Lithiation is thermodynamically favorable (at least after $x > 0.5$ in Li_xSi) [206] favoring a mixing of Li and Si atoms, while one has to apply external driving force for delithiation [27, 217]. Where lithiation of c-Si or a-Si has been studied extensively by theory and experiments [35, 74], delithiation is not yet fully understood [26, 217].

At room temperature, lithiation of c-Si forms a-Li_xSi via a two-phase reaction [51, 52, 168]. In-situ TEM results showed a clear phase boundary (approx 1 nm thick) between c-Si and a-Li_xSi during the lithiation of c-Si [52, 168], which was later observed for the a-Si case as well but with a thicker phase boundary [53, 168]. First-principles calculations also confirmed the stability of a two-phase region as compared to a single phase [76, 218], while at high temperature (above 415 °C), Si forms crystalline Li_xSi phases [62] upon lithiation. The formation of c-Li_xSi phases at room temperature is limited by kinetics with an exception of c-$Li_{15}Si_4$ [219], which can be avoided during room temperature lithiation if the voltage is kept above 70 mV [34, 171].

The delithiation of these lithiated a-Li_xSi phases results in a-Si with approximately 0.1-0.4 eV higher energy per Si atom as compared to starting c-Si phase, which is roughly the energy difference between the amorphous and crystalline phase of bulk silicon [37]. However, whether the a-Si after lithiation and delith-

iation, return to its original form is still not clear. Some empirical-potentials-based studies [76, 217] tried to answer this question, which is discussed in the next chapter with our comparison by using classical potential. In this chapter, we will focus on the first-principles based approaches.

Chevrier *et al.* [75] suggested a lithiation and delithiation protocol that has been used successfully to obtain the formation energies as well as the voltage profile (explained in the next section) within an accuracy of ± 0.1 V as compared to experiments [37, 220]. The delithiation part of the method involves step-by-step random removal of Li atoms followed by volume scaling and constant volume relaxation. One can in principle control the delithiation rate by varying the number of Li atoms removed at a time. Although the volume rescaling ($\sim$14 Å^3) per Li atom is in line with the experimental evidence of average volume occupied by a Li atom, restricting relaxation under fixed cell parameters might result in artifacts. This limitation was also mentioned in their original work but due to the instability of relaxation routines (cell and ionic) they chose this approach. This scheme has also motivated the development of similar methodologies with improvements to study lithiation and delithiation from first-principles [221, 222].

In this work, we have also proposed a small modification in the method to incorporate the full cell relaxation followed by a few steps of AIMD simulations. We hope this will provide a more robust method to study delithiation with experimentally comparable results. Moreover, we hope that our analysis on the evolution of local environment of Si will enhance the limited understanding on the structural evolution of Si during lithiation and delithiation [37, 222, 223].

4.2 COMPUTATIONAL DETAILS

The first-principles total energy calculations were performed with DFT as implemented in the ABINIT code [195–198] using a plane-wave basis set within the generalized-gradient approximation (GGA-PBE) [199]. The converged kinetic energy cutoff for plane-

waves was 32 Ha (~871 eV) as obtained for calculations in the previous chapter with ONCVPSP pseudopotentials [200, 201] having 1s and 2s valence electrons for Li while, for Si, 3s and 3p electrons were treated as valence electrons.

The primitive cell of $Li_{13}Si_4$ consisting of 26 Li atoms and 8 Si atoms, was used for testing the algorithm. One might perhaps perform a systematic study with larger supercells that will give a more discrete step size for the concentration change. For sampling the Brillouin zone, a $3\times3\times3$ Monkhorst-Pack k-point mesh was used. As it is a metallic system, a Gaussian smearing of 0.01 Ha (0.23 eV) was used for obtaining the occupation of states [202]. The convergence criteria for k-points grid, total energy cutoff and SCF cycles are the same as mentioned in the previous chapter. The Broyden-Fletcher-Goldfarb-Shanno (BFGS) and the Low-memory BFGS (L-BFGS) minimization algorithms were used for structural relaxation until the forces on each atom were smaller than 5×10^{-6} Ha/Bohr (0.3 meV/Å).

4.2.1 *Delithiation protocol*

The delithiation method adopted in this study is inspired by the one suggested by Chevrier *et al.* [75] for step-by-step removal of Li atoms to mimic delithiation. However, unlike a constrained search for relaxed atomic positions for a scaled volume, we modified the protocol to include complete cell relaxation in between consecutive steps of delithiation as illustrated in Fig. 4.1. The complete structural relaxation of cell parameters and atomic positions will allow the system to traverse the closest valley in the energy-configuration landscape. This will essentially help in reproducing the experimental delithiation process of Si anodes. Similar approaches have been proposed by Cubuk *et al.* [222] allowing a full structural relaxation at each step of Li insertion in a-Si, and by Chan *et al.* [37] removing the Li atom that provides the lowest energy configuration followed by a full structural relaxation. In this work we build up on this idea of full structural relaxation in between two consecutive delithiation step in addition with few steps of molecular dynamics to assist structural

relaxation. The process was automated by using the Abipy workflow manager to efficiently run the whole procedure. The important steps of the delithiation workflow are:
Delithiation scheme:

1. Relax the atomic positions of the structure.
2. Perform complete structural relaxation.
3. Calculate the total energy of the structure.
4. Perform 50 molecular dynamics steps.
5. Randomly remove a Li atom.
6. Return to step 1 until there is no Li atom to remove.

In principle, instead of random removal, one can first make a test to select the Li atom that minimizes the total energy upon

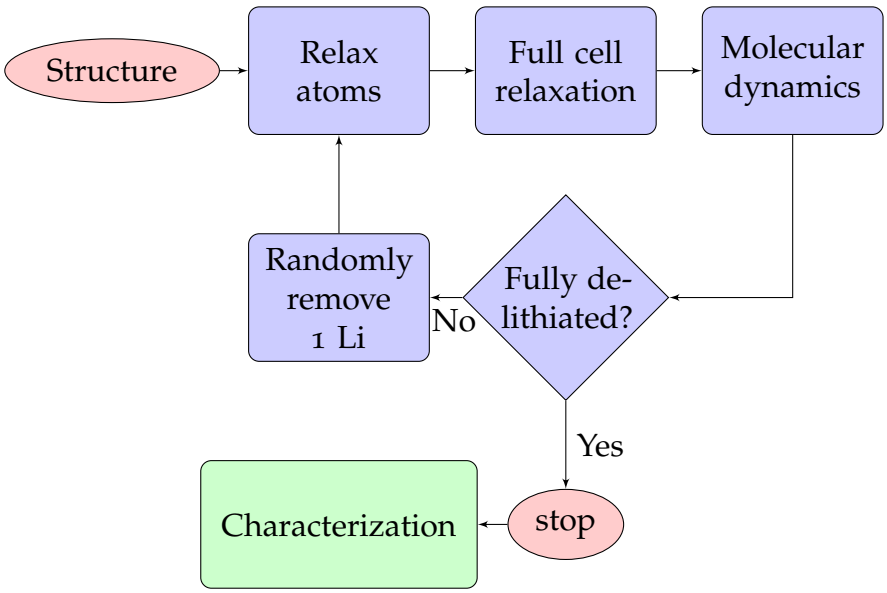

Figure 4.1: Illustration of the workflow of the proposed delithiation scheme. It is inspired from the original routine of Chevrier *et al.* [75] with a complete structural relaxation step, instead of fixed volume scaling and constant volume ion relaxation.

removal. However, the advantages do not outweigh the added complexity and the computational cost. Moreover, it has been shown that the final energy after structural relaxation is independent of the site selection [37, 75].

4.2.2 *Characterization:*

In literature, there are two definitions of formation energies, one defined as per total number of atoms and the other as per Si atom. In this Chapter we have adopted the definition of per Si atom, simply for comparison purposes with the literature. This is defined as:

$$E_f(x) = E_{Li_xSi} - (xE_{Li} + E_{Si}) \tag{4.1}$$

$$\tag{4.2}$$

where x is the number of Li atoms per Si atom and E_{Li_xSi} is the total energy of Li_xSi per Si atom, E_{Li} is the total energy of one Li atom in body-centered cubic structure and E_{Si} is the energy per unit Si atom in a diamond cubic structure.

The chemical potential can be written in terms of the Gibbs free energy change by using the Nernst equation [193, 224] as:

$$V(x) = -\frac{\Delta G}{\Delta q} = -\frac{\Delta G}{\Delta x} \tag{4.3}$$

where ΔG is the Gibbs free energy change combined for the reactions at cathode and anode and Δq is the amount of charge transferred, which is also equal to Δx as one electron is transferred per Li atom. The Gibbs free energy can be written in terms of entropy and internal energy term as:

$$V(x) = -\frac{\Delta E + P\Delta V + T\Delta S}{\Delta x} \approx -\frac{\Delta E}{\Delta x} \tag{4.4}$$

At low temperature the entropy and pressure terms can be neglected, and the Gibbs free energy can be approximated to the internal energy change ($\Delta G \approx \Delta E$) that can be computed from

DFT calculations [224]. Thus, if the energies are expressed in eV, the potential can be defined as a function of lithium content:

$$V(x) = -\frac{\partial E_f}{\partial x} \tag{4.5}$$

This approximation is a common practice in the field to compute the potential change from the total energy calculations and have been successfully tested for a variety of electrode materials [37, 193, 223, 224]. Nonetheless, being the first-order derivative of the total energy, the quantity becomes sensitive to small fluctuations in the energy curve. Appropriate smoothing of the energy profile should be done before computing the derivatives.

The local structure evolution of Si atoms during delithiation is studied by using the chemenv tool provided under Pymatgen library. Based on several trials, we obtained 0.7 and 1.6 as a suitable set of values for the angle and distance cutoff parameters for Chemenv, respectively. For more details about the limitations and theoretical details, reader can go through the original paper by Waroquiers *et al.* [156]. This local environment is used in computing the coordination number, average number of Li and Si neighbours as well as analysing the local environments of Si atoms in fully delithiated Si structure.

4.3 STRUCTURE OF $LI_{13}SI_4$

The primitive cell of c-$Li_{13}Si_4$ was selected as the test case to test our suggested delithiation protocol. It is the most lithiated crystalline phase with Si-Si bonding, as above this lithiation level, Si atoms are isolated in a sea of Li atoms [31]. Fig. 4.2 shows the crystal structure of the primitive $Li_{13}Si_4$ containing 26 Li atoms and 8 Si atoms. There are 7 different Wyckoff sites for Li atoms and 2 for Si atoms as outlined in Tab. 4.1 along with the lattice parameters. The optimized lattice parameters are in good agreement with the published literature [31, 177]. The 2 different Wyckoff sites for Si can be observed in the crystal structure with 4 Si atoms forming dimers as one type and 4 remaining isolated Si atoms as another type. The corresponding local environment

observed for these two sites are triagonal bipyramidal (T:5) and square planar (S:4), respectively, as shown in Fig. 4.3.

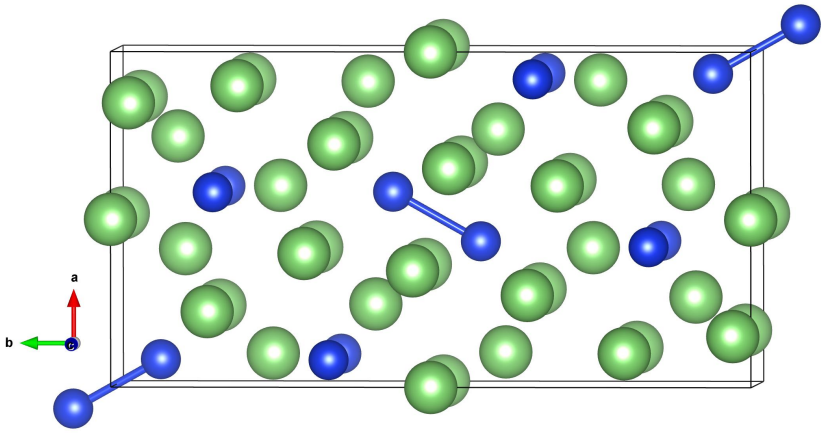

Figure 4.2: Crystal structure of primitive $Li_{13}Si_4$ cell showing 8 Si atoms (blue) and 26 Li atoms (green).

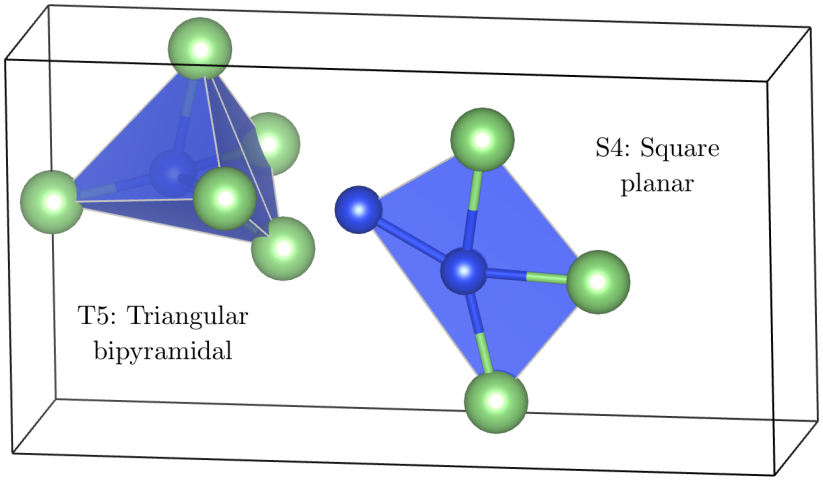

Figure 4.3: Illustration of triagonal bipyramidal (T:5) and square planar (S:4) local environments for Si in c-$Li_{13}Si_4$. Other atoms are suppressed for easy visualization of the selected atoms.

The evolution of the local environment of these two types of Si atoms can provide some useful insight in the structural transformation during delithiation.

Table 4.1: Optimized coordinates of Wyckoff sites for $Li_{13}Si_4$ crystal structure [31]. The optimized lattice parameters obtained in this work using GGA-PBE are: $a = 7.9004$, $b = 15.1141$, $c = 4.4403$Å, $\alpha = \beta = \gamma = 90^\circ$ with the space group Pbam (# 55).

	Wyckoff site	x	y	z
Li1	2c	0	1/2	0
Li2	4g	0.0965	0.1942	0
Li3	4g	0.2708	0.3461	0
Li4	4g	0.1529	0.0258	0
Li5	4h	0.2596	0.0952	1/2
Li6	4h	0.4098	0.2564	1/2
Li7	4h	0.0969	0.3939	1/2
Si1	4g	0.4175	0.1603	0
Si2	4h	0.4284	0.4318	1/2

4.4 VOLUME AND FORMATION ENERGY

The fractional volume change has been used as the first validation criteria of our delithiation protocol. Fig. 4.4 shows the plot of fractional volume change versus Li concentration as the delithiation proceeds. Overall our delithiation protocol follows a similar volume change curve as compared to the experimental Atomic Force Microscopy (AFM) data [225] as well as the previous *ab-initio* calculation [75], except that the starting lithiated structure is more highly packed. This is expected as we started with a relaxed c-$Li_{13}Si_4$ structure as compared to a-Li_xSi formed during lithiation experiments or in case of Chevrier *et al.* [75], obtained during several lithiation and delithiation cycle of c-Si.

Fig. 4.5 shows the formation energy per Si atom ($E_f(x)$ as per Eq.(4.1)) plotted at each delithiation step as a function of Li concentration (x) in Li_xSi. The delithiation scheme was repeated

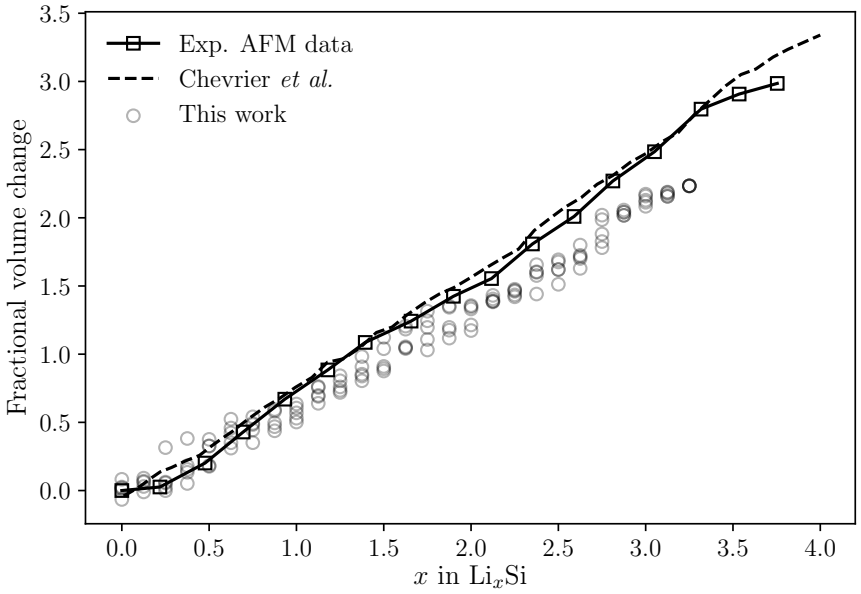

Figure 4.4: Fractional volume change with respect to crystalline-bulk Si vs. lithium concentration (hollow circles). Experimental AFM data (hollow squares with solide line) [225] and the data from Chevrier *et al.* (dashed line) [75] has also been plotted for comparison.

5 times from the same starting structure of $Li_{13}Si_4$ to gather statistics. Literature data from the original method of Chevrier *et al.* [75] for lithiation-delithiation cycles of 5-8 Si atoms cells are also plotted for comparison along with the *ab-initio* and experimental values for crystalline Li_xSi phases.

Only the smooth spline of the formation energy has been shown for the data of Chevrier *et al.* [75], the original data points spread within a range of ± 0.1eV. The calculated formation energies in this work lie within that range with a slight shift on the upper side, expecially for Li concentration (x) < 2. This kink around $x \sim 2$ is in agreement with a previous study suggesting a change in the local environment of Si atoms above a Li concentration level of approx. 2.25 [226]. In the vicinity of this concentration, there are some delithiated structures close to the experimental value of Li_7Si_3, but none of them has the same

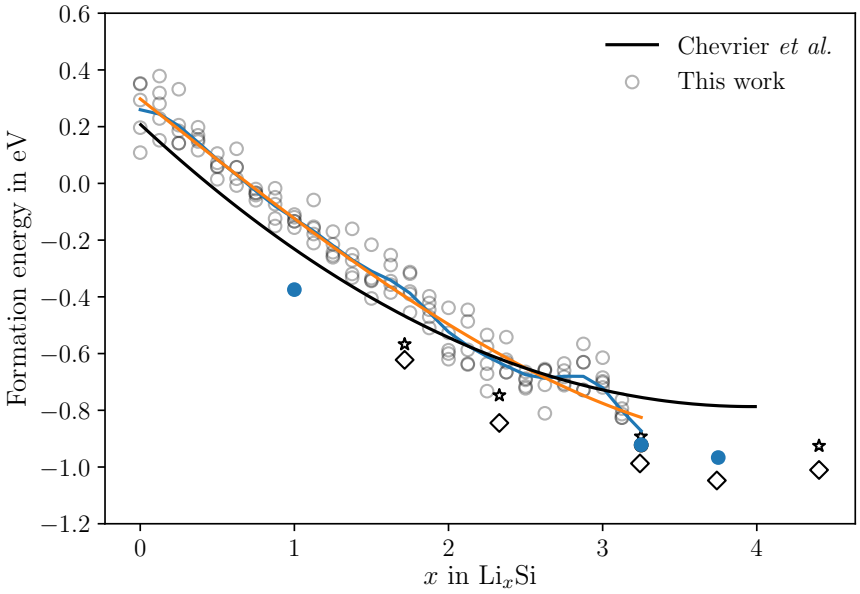

Figure 4.5: Computed formation energies (open circles) plotted as a function of delithiation stage for 5 different runs along with gaussian smoothing (blue) with $\sigma = 1$ and cubic spline (orange). Solid (black) line represents the delithiation data reported by Chevrier *et al.* [75]. Open markers represent the experimental (star) [62] and the *ab-initio* data (diamond) calculated with PAW [193] for crystalline Li_xSi phases. Filled markers are the formation energies calculated in this work.

space group and symmetries. Moreover, due to the concentration step chosen in this work, the Li concentration associated with Li_7Si_3 (2.33) falls in between two consecutive concentration steps (2.28 and 2.40).

Overall the formation energy curve is in good agreement with their data showing a similar slope, except with a jump near the start corresponding to $x \sim 3.0$. The jump in the formation energy is consistent with all the 5 runs suggesting a pattern, within the statistical limitation of 5 runs. The slope of the curve is also higher at $x > 3.0$, after which the delithiation follows a lower slope. This points towards formation of some strong bonds or restoration of some local order resulting in lowering

of formation energy. In another study with crystalline phases, Chan *et al.* [37] had also observed similar kinks in the formation energies near the start of the delithiation process. Perhaps the delithiation of an amorphous phase will not involve breaking of these symmetries and the curve will be smoother as observed by Chevrier *et al.* [75].

In order to further support our hypothesis about the change in local order around $x \approx 3$, the two structures were analyzed (refer Fig. 4.6), one corresponding to the peak with concentration $x = 2.88$ (on the left) and the other one formed just after crossing the peak with concentration $x = 2.75$ (on the right). In terms of concentration, they only differ by one Li atom. The left one has roughly a similar structure as the starting one in terms of Si atoms with two dimers and 4 isolated Si atoms. With a removal of one Li atom, the right structure forms which has an extra Si-Si dimer as compared to the left one. This explains the drop in the formation energy after $x = 2.88$ due to the formation of a strong Si-Si dimer bond.

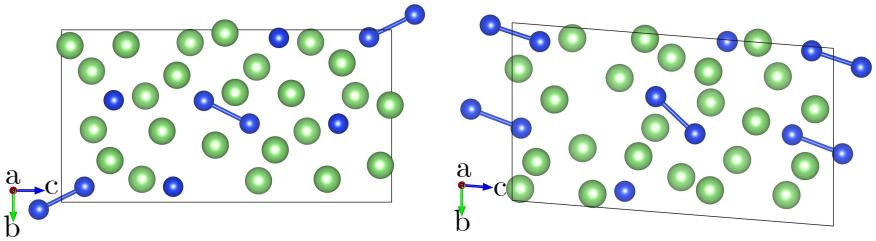

Figure 4.6: Crystal structure obtained at Li concentration $x = 2.88$ (on the left) during delithiation of c-$Li_{15}Si_4$ is compared with the next consecutive delithiated structure at $x = 2.75$ (on the right). The formation of an additional Si-Si dimer in the right one is associated with a drop in the formation energy curve, otherwise increasing during delithiation.

The formation energy curves fitted with the cubic spline and the gaussian smoothing were then used to compute the voltage curve (Fig. 4.7) as per Eq. 4.5. The spline provides a simplest fitting of formation energy with a cubic polynomial that results in a quadratic behaviour of voltage profile(orange). The gaussian

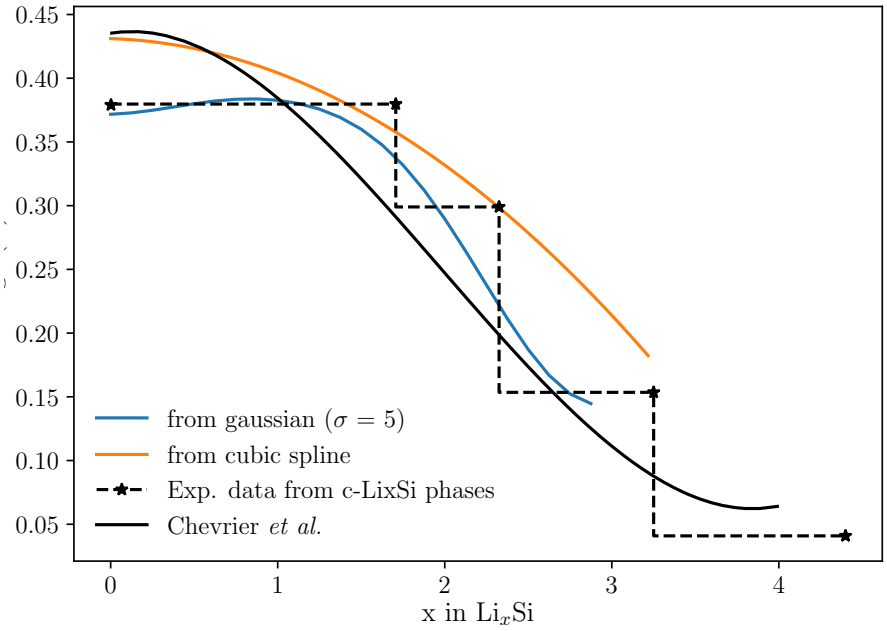

Figure 4.7: Potential-composition curve for delithiated silicon obtained from the derivative of cubic smoothing spline(orange) and a gaussian smoothing (blue) with $\sigma = 5$ of the cohesive energies. Markers represent the values calculated from the experimental date calculated at 415 °C [62, 193] and the solid black line is the smoothing spline from a previous *ab-initio* study of silicon lithiation [75].

smoothing (with $\sigma = 5$) provides a more accurate description (blue) with the potential curve flattening as the Li concentration reaches zero. To avoid divergence at the other extreme, last 3 values were not used in gaussian smoothing, as discussed earlier these fluctuations might be due to symmetry breaking of crystalline phase. The literature data from Chevrier *et al.* obtained from a piecewise smoothing curve with a weight of 500 [75] is also plotted for reference along with experimental data of lithiation of c-Si at 415 °C [62, 193]. Both smoothing approximations (spline and gaussian smoothing) used in our work is in good agreement with the previous *ab-initio* data as well as the experimental data within a range of (±0.1 V). As the formation energy curves and the voltage profile is in good agreement with the lit-

erature, the structural evolution of Si atoms are discussed in the next section.

4.5 STRUCTURAL EVOLUTION OF SI ATOMS

The change in the radial distribution function is used as a first measure to study the structural evolution during delithiation. Fig. 4.8 shows the change in RDF for Si-Si, Li-Li and Li-Si pairs at different stages of delithiation. In the RDF of Si-Si, the Si-Si bond of dimers correspond to the first peak at 2.37 Å and the second peak at 4.69 Å corresponds to a pairing of an isolated Si atom to another Si atom forming a dimer. The first peak remain as is during delithiation but the second peak shifts close to ~4.1 Å. In the RDF of Li-Si, the first peak corresponding to Li-Si bonds is observed at 2.5 Å. The other peaks for long range order disappear first as more Li atoms are removed and the system move from Si atoms sitting in a Li rich state to Li atoms isolated in Si rich state. Specifically, the second and third peaks disappear after a 1:1 ratio of Li and Si atoms (Li_8Si_8. On comparing the RDF of fully delithiated Si with a-Si experimental data, it shows a good resemblance (Fig. 4.9). The position of the first peak as well as the full width at half peak is in good agreement with that of a-Si. The second peak identified at 3.8 Å is in good agreement with that of exp. data at ~3.8Å, however the shape is not the same and there is a shoulder peak as well. Although the RDF of delithiated Si is in close agreement to a-Si case with a strong first peak and a distinguishable second peak, the smaller cell size restricts us from making a conclusive remark on it. However, an analysis on the evolution of coordination number (CN) and neighbours of Si atoms will provide more details on the structural change that Si atoms undergo during delithiation.

Fig. 4.10 shows the values of coordination number per Si atom averaged over 5 runs for varying Li concentration along with the derivative of the gaussian fit (solid line) to highlight changes of slope. The pie charts on the top illustrates the distribution of local environments of all the 8 Si atoms at the fully lithiated c-$Li_{15}Si_4$(right) and the completely delithiated Si struc-

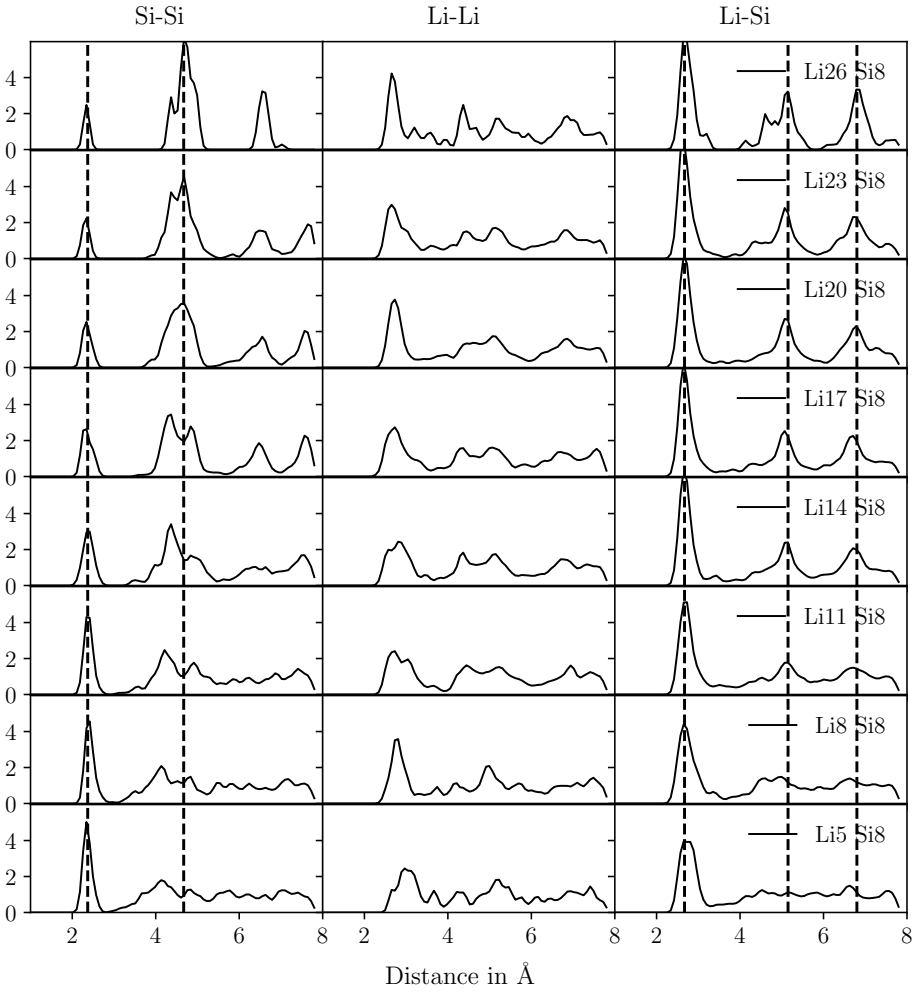

Figure 4.8: Radial distribution functions of Si-Si (first column), Li-Li (second column) and Li-Si (third column) averaged over 5 runs are plotted at different stages of delithiation of p-$Li_{13}Si_4$(rows). The concentration at each stage (row) is mentioned in the legend of Li-Si RDF. Dashed lines indicate the location of the first peak for Si-Si (2.38 Å) and Li-Si (2.67 Å) neighbours.

ture (left).The average coordination of the completely delithiated silicon structures is 4 with Tetrahedral (T:4) and See-saw (SS:4) environment, suggesting a similarity with some form of Si (amorphous or crystalline). The sudden rise in the coordin-

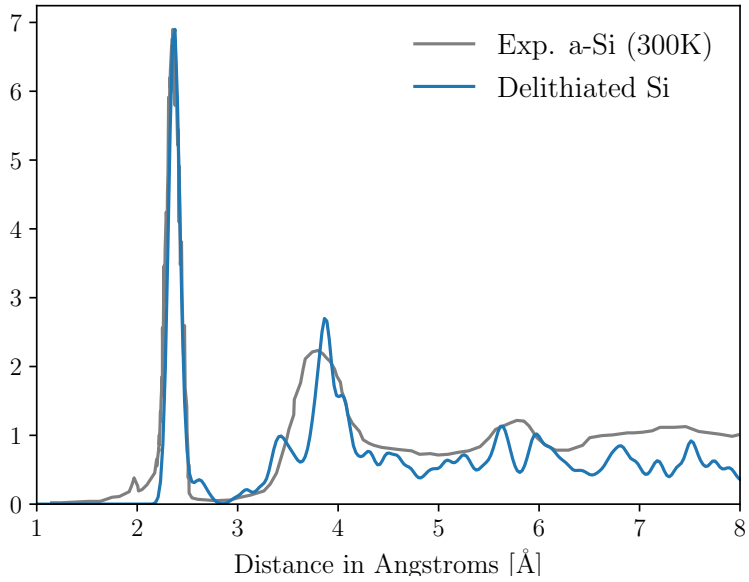

Figure 4.9: Radial distribution function of completely delithiated a-Si obtained from our delithiation process along with experimental data for amorphous Si at 300K [227]. RDF intensities are scaled to match the height of first peak.

ation number at the other end (near $x \sim 3$) is in line with the increase in the cohesive energy observed earlier due to breaking of crystalline symmetry. The derivative curves shows two major peaks of change in CN at $x \approx 2.3$ and $x \approx 1.3$. The first one is at the concentration close to that of Li_7Si_3 ($x = 2.33$) and the closest crystalline phase near the second peak is LiSi ($x = 1$). The formation energy of structures near the concentration of Li_7Si_3 was closer to that of the crystalline phase and a drop in coordination number also suggests some restoration of order.

As discussed earlier, there are two different Wyckoff sites of Si atoms in the starting c-$Li_{13}Si_4$ (with S:4 and T:5 local environment), their CN shows that their local structure also evolves differently during delithiation, at-least till Li concentration reaches $x \approx 2.3$. This finding also supports the restoration of some local order as observed in the change in overall coordination num-

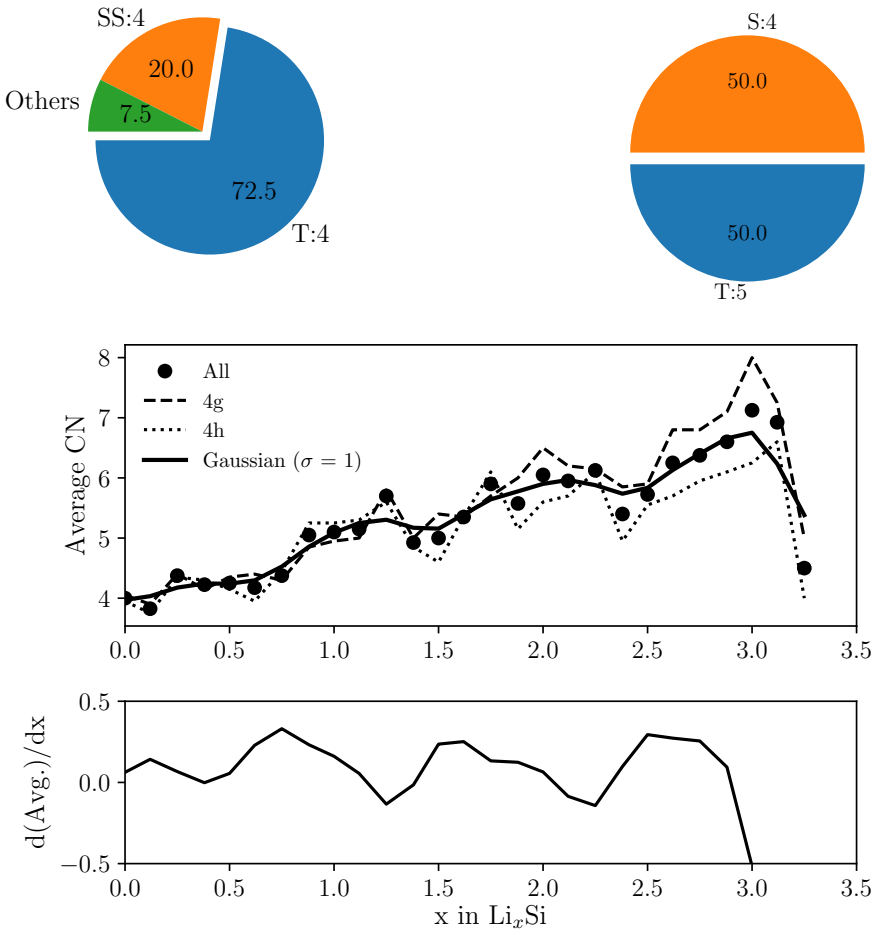

Figure 4.10: Average coordination number (dots) per Si atom for 5 runs are plotted vs Li concentration as the delithiation proceeds (top). Solid line is the gaussian smoothing (σ = 1) curve used for computing the derivative (bottom) to show the change in CN of Si atom. Coordination numbers of Si atoms with two different Wyckoff sites 4g (dashed) and 4h (dotted) are also plotted, where the latter is associated to the Si dimers in the original $Li_{13}Si_4$ structure. The pie charts on top shows the distribution of local environment for the starting c-$Li_{13}Si_4$ structure (right) and the completely delithiated Si structure (left).

ber and the cohesive energy. Moreover, the average coordination number between 4g and 4h becomes much closer after the second peak at $x \approx 1.3$, however the difference is within the statistics of the data and no conclusive remark can be made for this observation.

In order to observe the local structure of Si atoms with respect to their neighbouring Si and Li atom, average number of Li and Si neighbours of a Si atom are plotted along with their derivative curve (Fig. 4.11 and 4.12). The standard gaussian smoothing was used with σ =1 for finding the peaks by taking its derivative. Both the curves, i.e. the average Li neighbours and the average Si neighbours, are relatively smoother and roughly linear as compared to the coordination number plot (Fig. 4.10). The difference in the 4g and 4h are visible here as well but disappear below $x \approx 2.5$. The starting points of average Si neighbours for 4g and 4h depicts the isolated Si and dimer Si characteristics discussed above. Moreover, the calculated values of average Si neighbour are in good agreement with the values reported in a previous *ab-initio* calculations (hollow squares in Fig. 4.12) for lithiation of c-Si [177].

Overall the trend of the Li neighbour plot is similar to the change in the coordination number. As the delithiation proceeds Si-Li bonds break and new Si-Si bonds form and as there are more Li atoms (at-least at $x > 1$), the decrease in coordination number is expected to be dominated by the breaking of Li-Si bonds. This correlation in the coordination number and effective Li neighbour was also reported by Cubuk *et al.* [222] during lithiation of a-Si. However, they observed a more steeper change in the coordination number at-least till $x < 2$ and saturates afterwards. The steeper slope might be due to the starting amorphous phase with a relatively more open structure, i.e. more places to put a Li atom as compared to the crystalline counterpart. The discrepancy can also be attributed to the method used for counting the near neighbours and the cutoff distance. Kim *et al.* [177] showed that the average CN of Si atoms in a-Si can vary from 2.9–5.7 at the lower end ($x = 0.33$) to $1.23 - 9.97$ at the higher end ($x = 4.33$) of lithium concentration with a variation of cutoff

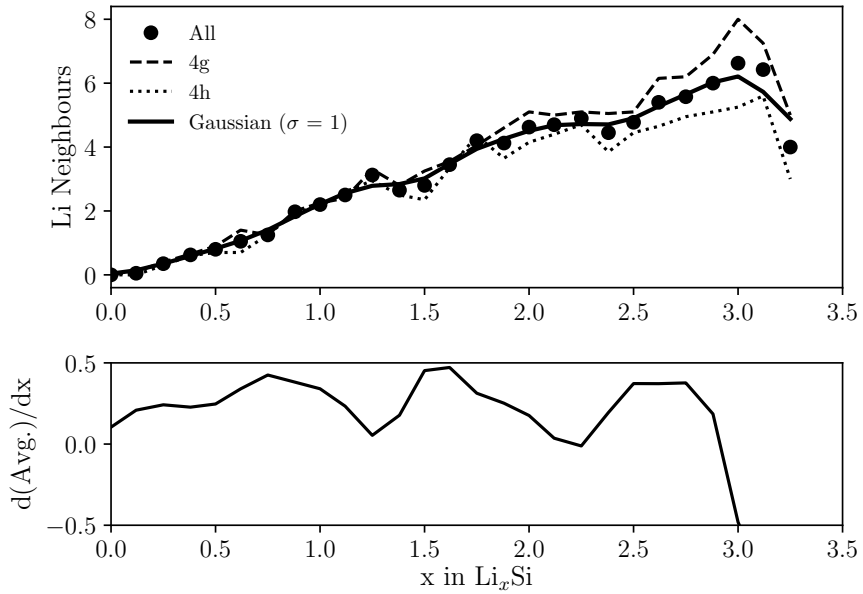

Figure 4.11: Average number of Li neighbours (filled circles) of Si atoms observed during delithiation are plotted vs Li concentration(top) along with the gaussian smoothing (σ=1) in solid line, which is used for computing the derivative curve (bottom). Similar data is also plotted for Wyckoff sites 4g and 4h of Si atoms.

radius from 2.5 to 3.1 Å. Note that with a lower cutoff radius of 2.5 Å, the average CN decrease from 2.9 to 1.23 as there are fewer tightly bonded atoms as lithiation proceeds. In the work of Cubuk *et al.*, this cutoff range is not mentioned explicitly and rather it changes with the lithiation level, making it difficult to have a fair comparison. In this work, we have used a robust Voronoi tesselation provided by chemenv tool to obtain the local environment of each site, which in turn provides the average coordination number. Nonetheless, our reported values of average Si neighbours are in good agreement with those reported by Kim *et al.* [177].

The data for the effective Li neighbours reported by Chevrier *et al.* [223] also confirms a linear relationship with an increase in the lithiation level as observed in our work. However, they used

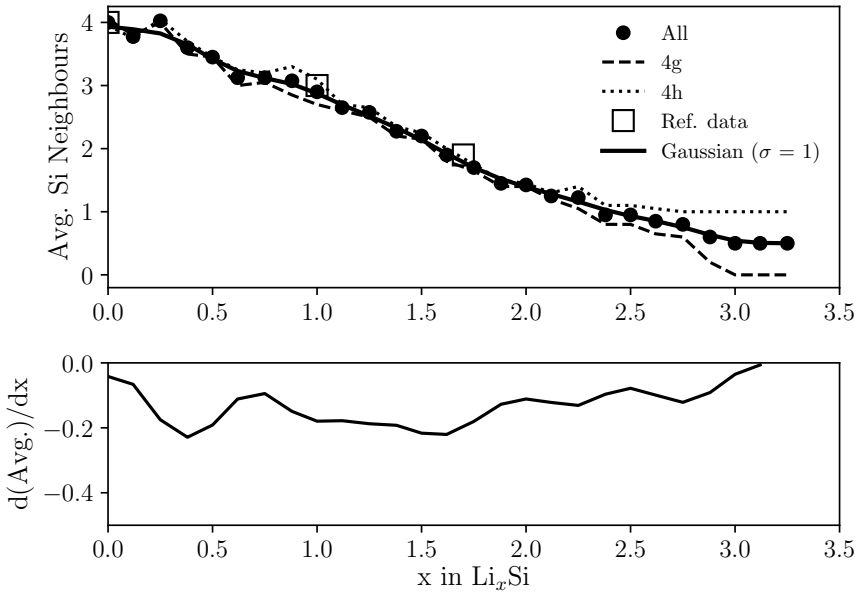

Figure 4.12: Average number of Si neighbours (filled circles) of Si atoms observed during delithiation are plotted vs Li concentration(top) along with the gaussian smoothing (σ=1) in solid line, which is used for computing the derivative curve (bottom). Similar data is also plotted for Wyckoff sites 4g and 4h of Si atoms. Reference data of crystalline phases (empty squares) from first-principles calculations [177] are also plotted for comparison.

a partial counting of Li neighbours shared between multiple Si atoms, i.e. one Li atoms shared by two Si atoms is counted as 0.5 for each Si atom as illustrated in Fig. 4.13. A partial counting yields a lower number of Li neighbours for each Si atom, which can be observed on comparing with our values. More specifically, our values goes from 0-8 at $x = 3$ as compared to their values going from 0 to 3 for the same range of lithiation.

Thus, our findings for the delithiation dynamics and structural evolution of Si atoms are in line with the literature. Moreover, the formation of an extra Si-Si dimer has been observed in the formation energy curve as well as the change in the local coordination of Si atoms.

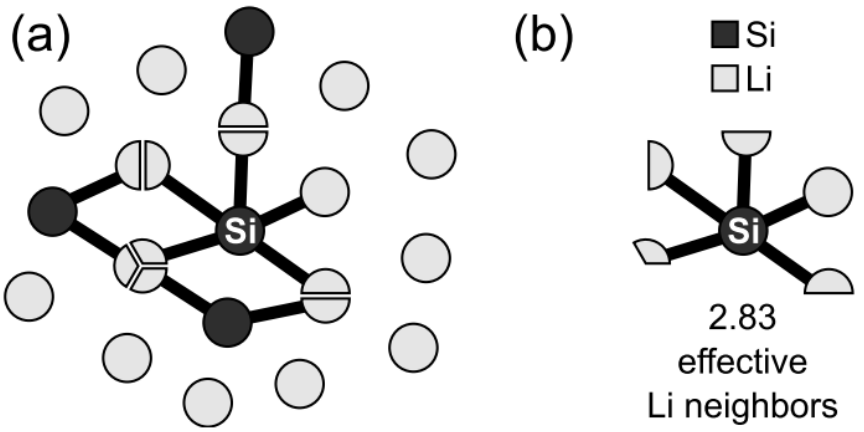

Figure 4.13: Schematic illustration of the method to partial count the number of Li atoms. a) Li atoms are shared with multiple Si atoms and are counted partially based on the type of sharing and b) the summation of these partial Li atoms yields an effective Li neighbour for the corresponding Si atom. Reproduced with permission from Ref.[223]. All rights reserved, Copyright 2010 IOP Publishing.

4.6 DELITHIATED SILICON

The average CN and the average number of Si neighbours suggest that the Si atoms in fully delithiated Si structures are 4-fold coordinated. The local environment analysis by Chemenv also confirms this as a majority of Si atoms were in the tetrahedral environment (T:4 refer to Fig. 4.10). To further analyze the local order, the RDF's are plotted for these structures as shown in Fig. 4.14. The space groups obtained by ABINIT shows three types of Si structures obtained from 5 different runs. The RDF's of all the 5 structures show a strong first nearest neighbour peak as well as a very strong second neighbour peak as well suggesting a restoration of crystalline nature. This recrystallization behaviour has also been observed by Jung *et al.* [76] during delithiation of Si NWs. However, the small structure of 8 atoms in the current work has forced symmetries due to the periodic boundary conditions and thus one can not comment on the crystalline

or amorphous nature of the Si structure. Perhaps working with a bigger supercell or another lithiated structure with sufficiently large number of Si atoms can help in answering this question. This often comes at an additional computational cost or with a classical potential parameterized to study the interaction of Li-Si system. In the next chapter, we will use one of these classical potentials for studying delithiation of larger supercells that might be helpful in answering further questions regarding delithiation of Si based anodes.

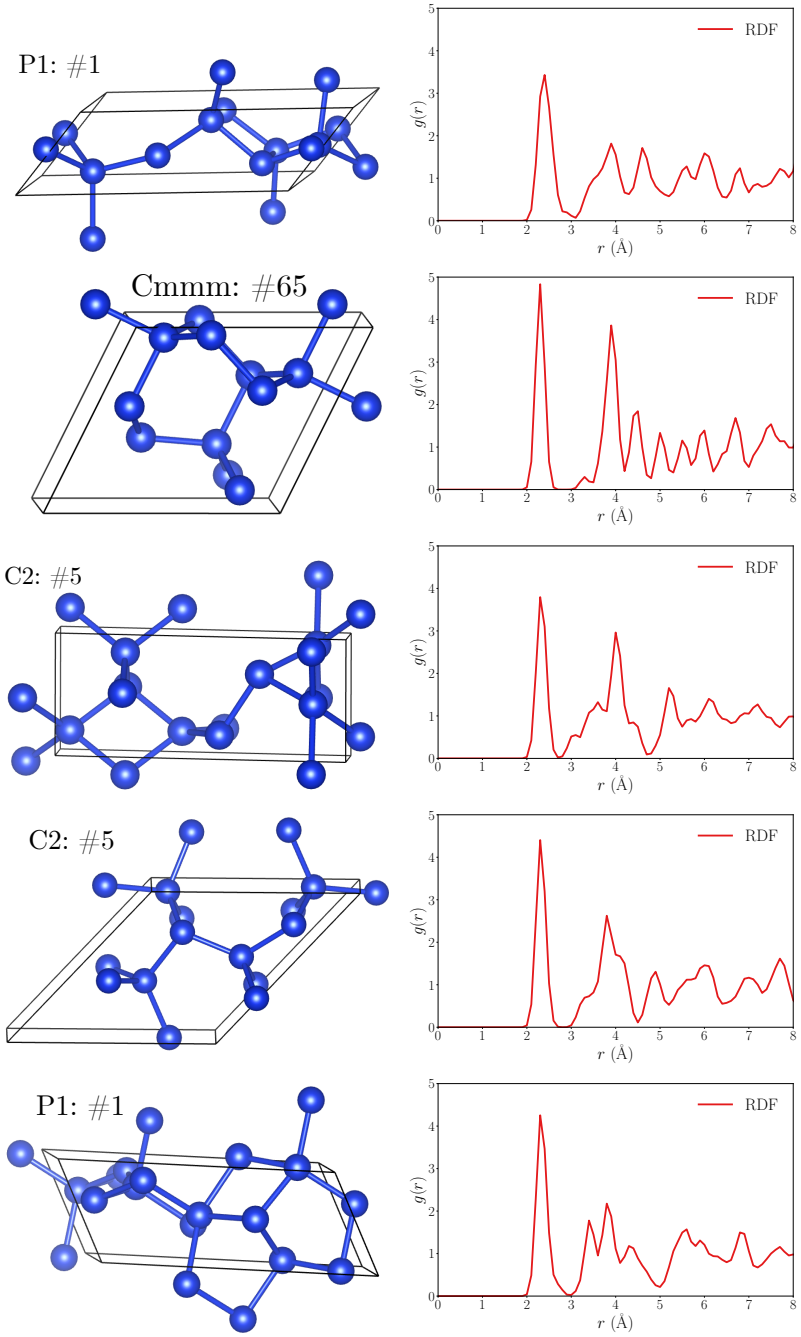

Figure 4.14: Delithiated Si structures (left) and their corresponding RDF's (right) obtained from 5 delithiation runs of c-$Li_{15}Si_4$. Space groups of each structure are also mentioned on the top left.

5

DELITHIATION USING CLASSICAL POTENTIALS

This chapter covers the validation of two different MEAM potentials followed by the use of one of them to study delithiation of a-$Li_{15}Si_4$ that can overcome the size limitation of first-principles calculations and possibly answer some questions on the morphology of delithiated Si.

In the previous Chapter, we have seen that first-principles DFT-based calculations can be used to compute properties at extreme conditions (low temperature effects) or those which are not well studied experimentally (diffusion of Li in c-LiSi). However, these methods are computationally expensive and are often limited to a few hundreds of atoms. We have observed this limitation in the previous Chapter while comparing the delithiated Si structure with a-Si, which needs thousands of atoms to have the correct statistics.

For these kinds of applications involving very large number of atoms, empirical-potentials like Modified Embedded Atom MethodMEAM potentials, are often helpful. The next section introduces two parameterization of MEAM potential and their validation against literature values.

5.1 VALIDATION OF MEAM POTENTIAL

This section compares two forms of second nearest neighbours (2NN) MEAM potential and their values are compared with the first-principles data. For comparison purposes, the version of MEAM parameterized by Cui *et al.* [153] will be referenced as M1, and the other one proposed by Godet *et al.* [228] will be referenced as M2 in the rest of the Chapter. All the classical molecular dynamics simulations are performed using the LAMMPS code [229] with a time step of 2 fs. The first value used for com-

parison is the cohesive energy for all the known c-Li_xSi phases calculated as:

$$E_{coh} = \frac{E_{Tot} - n_{Li}E_{Li} - n_{Si}E_{Si}}{n_{Li} + n_{Si}} \tag{5.1}$$

where E_{Li}, E_{Si} and E_{Tot} represent, respectively, the energy of one Li atom in the bcc structure, the energy of one Si atom in the diamond structure and the total energy of the phase studied. The number of Li and Si atoms are denoted by n_{Li} and n_{Si}, respectively.

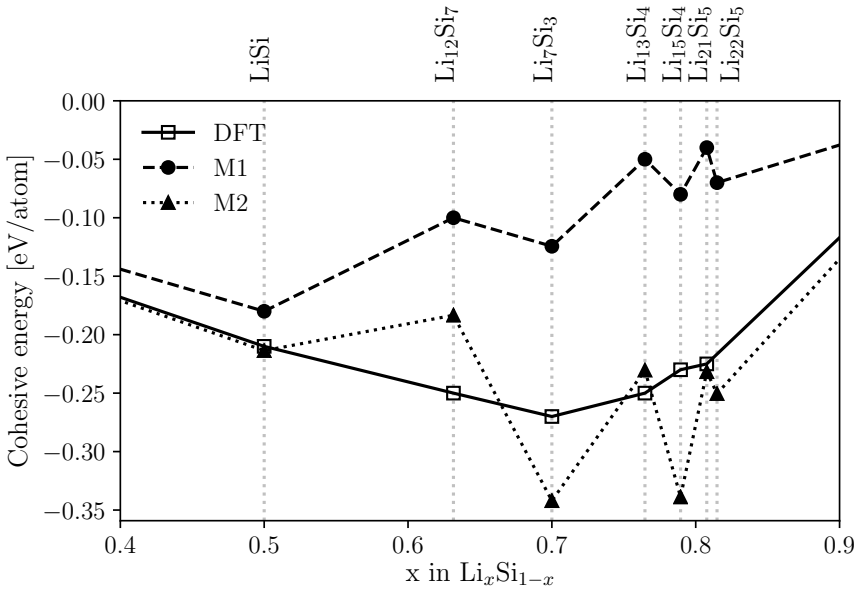

Figure 5.1: Cohesive energy of Li_xSi alloys, computed with MEAM potential (M1) parameterized by Cui *et. al.* [153] and (M2) by Godet *et al.* [228], and the DFT data reported by Chevrier *et al.* [75]. Connecting lines for each method marks the respective convex-hull.

Fig. 5.1 shows that the values obtained with M2 are closer to the DFT values as compared to the original M1, except for an overbinding of $Li_{15}Si_4$. M1 shows LiSi phase as the most stable phase, followed by $Li_{15}Si_4$ and $Li_{22}Si_5$ on the convex hull with

an increase in Li concentration. The cohesive energies of stable $Li_{12}Si_7$, $Li_{13}Si_4$, and $Li_{21}Si_5$ lies above the convex hull and are thus unstable at 0 K. While on the other hand, M2 only has LiSi and $Li_{15}Si_4$ as the stable phases with $Li_{15}Si_4$ overbonded by ~0.1 eV/atom. However, according to DFT results, the $Li_{15}Si_4$ is slightly above the convex hull at 0 K. Both the versions of MEAM potentials, miss out on $Li_{12}Si_7$ and $Li_{21}Si_5$, which are otherwise stable. However, M1 forms one more extra stable phase and does not strictly overbind any phase. The next metrics is the volume of formation, which is calculated in a similar way as cohesive energy:

$$V_f = \frac{V_{Tot} - n_{Li}V_{Li} - n_{Si}V_{Si}}{n_{Li} + n_{Si}} \tag{5.2}$$

where V_{Li}, V_{Si} and V_{Tot} represent the volume/Li atom for Li in the bcc structure, volume/Si atom for Si atom in the diamond structure and the total volume of the phase studied, respectively. The number of Li and Si atoms are denoted by n_{Li} and n_{Si}, respectively. Fig. 5.2 shows the calculated volume of formation curves from M1, M2 along with the DFT data from Ref. [75]. It shows that M1 values are in good agreement with DFT values for the overall trend and are shifted upward by $\approx$ .0.75 Å^3/atom. While values obtained from M2 are largely underestimated by $\approx$2 Å^3/atom, specially for Li_7Si_3, $Li_{13}Si_4$ and $Li_{15}Si_4$ crystal structures. Two of these structures (Li_7Si_3 and $Li_{15}Si_4$) are overbonded (as per their cohesive energies shown in Fig. 5.1), which could have resulted in an understimation of lattice parameter and thus yielding a higher volume of formation. However, the volume of formation for both these structures are amongst the lowest.

In order to confirm the stability of the Li_xSi structures, bulk modulus and the elastic modulus have also been computed from both the MEAM potentials and are compared with the DFT data from Ref. [230] as shown in Tab. 5.1. Before comparing the values, the negative values in the off diagonal terms have been verified for the mechanical stability criteria [98] and all the structures fulfil these criteria. First, let us compare the three structures (LiSi, $Li_{13}Si_4$, and $Li_{15}Si_4$), which are observed being under-

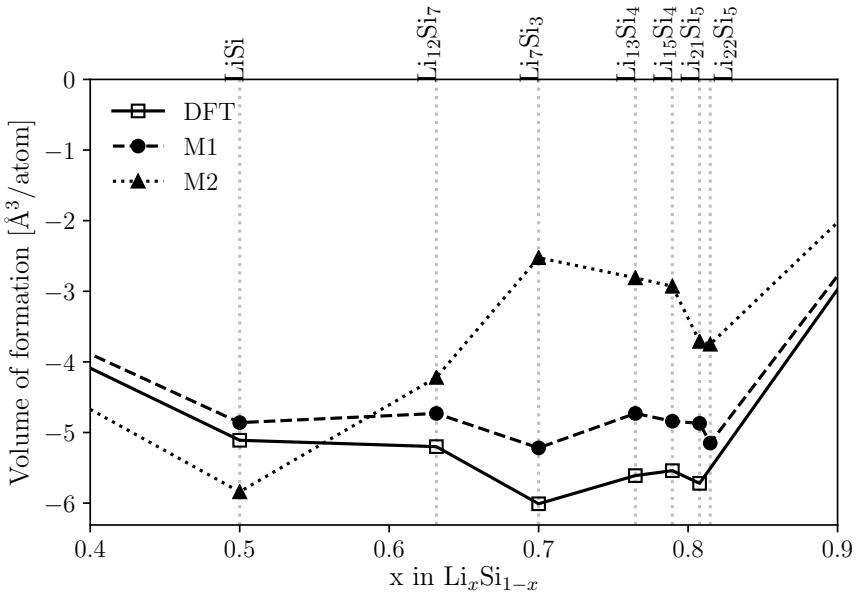

Figure 5.2: Volume of formation computed with MEAM potential (M1) parameterized by Cui *et. al.* [153] and (M2) by Godet *et al.* [228]. DFT data from Ref. [75] are also plotted for comparison.

estimated on their volume of formation by M2. Firstly, for two of them, namely $Li_{13}Si_4$ and $Li_{15}Si_4$, the bulk modulus are severely underestimated by M2 ($\sim$ 30%). Furthermore, for the latter one all the elastic constants are underestimated by roughly the same amount or more. For these structures, M1 stays roughly within a range of $\pm$10% error. For LiSi, we do not have the reference data of bulk modulus but in terms of first three diagonal elements, M1 overestimates by roughly 20%, while M2 overestimates by more than 50%. For the remaining structures both are roughly the same on the level of accuracy.

On the basis of these three tests: cohesive energy, volume of formation and elastic constants, M2 shows improvement as compared to M1 in the first to make it closer to DFT data, but it overbinds the $Li_{15}Si_4$ structure making LiSi go above the convex hull, that can be an issue for studying lithiation. For the second

metrics, M2 is significantly off from DFT data while M1 is in line with the overall trend of DFT data within close proximity. The third one, elastic constants depends on both the energy and volume to a higher order and thus are much more sensitive to inaccuracies in volume or energy [98]. In this section where M1 performs within the range of $\pm 10 - 15\%$, M2 deviates by more than 30-40% for some structures. Moreover, M1 is well studied and has been used for studying different properties of Li-Si system [150, 230–232], and M2 parameterization has recently been published and perhaps it needs some more tuning to improve the accuracy to a desirable level. Thus, we will use M1 for studying delithiation of a-$Li_{15}Si_4$.

5.2 SIMULATION METHOD

For studying delithiation, the starting a-$Li_{15}Si_4$ structure has been created from a $(10 \times 3 \times 3)$ supercell of c-$Li_{15}Si_4$ containing 6840 atoms. The starting structure is completeley melted at 4000 K for 100 ps using NPT ensemble followed by quenching to 300 K at a rate of ~9 K/ps. After quenching, the structure was further equilibrated at room temperature for another 100 ps and finally a conjugate gradient (CG) minimization was applied to get the room temperature density. This method has already been validated in literature [217, 228]. The obtained density of a-$Li_{15}Si_4$ thus obtained was 1.099 g/cm^3 at 300K, which is in good agreement with the experimental [33] and theoretical data [217].

For delithiating this a-$Li_{15}Si_4$ structure, we adopted the shell method suggested by Jung *et al.* [76] to randomly remove x number of atoms from a thin shell of thickness δ followed by n number of molecular dynamics run to let the system evolve. In another delithiation study, Kim *et al.* [217] has used a buffer layer of a-$Li_8Al_2O_3$, from which the Li atoms are removed, which in turn reduce the concentration of Li atoms in the anode (a-$Li_{15}Si_4$), however the current MEAM potential is only optimized for Li-Si system and we can not use such a design. Nonetheless in either of these methods, removal of Li atoms are from the surface that creates a concentration gradient for Li to diffuse from

Table 5.1: Bulk properties of known Li_xSi computed from the MEAM potential (M1) parameterized by Cui *et. al.* [153] and (M2) by Godet *et al.* [228]. The superscripts [a] and [b] represents the DFT data (LDA) from Ref. [230] and DFT data (GGA-PBE) from Ref. [153].

		B	C_{11}	C_{22}	C_{33}	C_{12}	C_{13}	C_{23}	C_{44}
Si	M1	99.3	169.1	169.1	169.1	64.4	64.4	64.4	56.0
	M2	99.2	163.4	163.4	163.4	67.2	67.2	67.2	63.3
	DFT[a]	96.2	161.3	161.3	161.3	63.6	63.6	63.6	76.7
LiSi	M1	80.5	112.4	112.4	94.5	57.9	72.2	72.2	41.6
	M2	93.79	164.3	164.6	129.9	53.6	69.5	69.6	58.2
	DFT[b]		101	101	77	19	37	37	45
$Li_{12}Si_7$	M1	56	87.4	86.5	79.4	40.6	43.9	40.0	16.5
	M2	42.8	92.9	78.9	73.8	27.5	22.1	19.9	29.4
	DFT[a]	40.5	100.3	106.5	101.5	5.7	13.5	8.7	31.2
Li_7Si_3	M1	48	98.7	98.7	93.3	36.2	17.2	17.3	22.6
	M2	32.7	134.8	134.8	72.7	-9.0	-7.5	-7.5	42.8
$Li_{13}Si_4$	M1	40.6	74.1	75.3	70.5	23.5	27.9	21.4	13.7
	M2	28.38	91.3	81.5	85.6	14.5	-8.3	-7.8	36.1
	DFT[a]	40.7	75.2	69.9	74.1	21.7	23.7	28	20.3
$Li_{15}Si_4$	M1	37.5	47.1	47.0	47.0	32.7	32.8	32.7	22.5
	M2	23.5	43.5	43.5	43.5	13.6	13.6	13.6	10.0
	DFT[a]	33.9	50.3	50.3	50.3	25.7	25.7	25.7	34.4
$Li_{21}Si_5$	M1	36.4	56.7	56.6	56.6	26.5	26.4	26.4	21.5
	M2	28.8	94.7	94.7	94.7	-4.2	-4.2	-4.2	22.4
	DFT[a]	34.9	65.5	65.5	65.5	19.7	19.7	19.7	33
$Li_{22}Si_5$	M1	35.9	51.7	51.7	51.7	28.0	28.0	28.0	29.6
	M2	26.3	90.5	90.5	90.5	-5.8	-5.8	-5.8	29.7
	DFT[a]	35.1	55	55	55	25.1	25.1	25.1	41.7
Li	M1	12.9	23.0	23.0	23.0	7.8	7.8	7.8	20.2
	M2	12.9	23.0	23.0	23.0	7.8	7.8	7.8	20.2
	DFT[a]	15.3	16.3	16.3	16.3	14.8	14.8	14.8	14.5

center to outwards. The rate of delithiation can be controlled by either the number of Li atoms removed at each step or the number of MD timesteps. However, the rate of delithiation should be comparable to the diffusion of Li atoms from center to surface to avoid any artifacts. Moreover, to speed up the simulation without any loss of generality, the delithiation process was car-

ried out at 1200 K, which is well below the melting temperature of bulk Si.

Based on the literature and the knowledge of Li diffusivity in a-Li_xSi, we selected a removal rate of 100 Li atoms per 100 ps, which is equivalent to a current density of ~6.4×10^5 A/cm^2. This is much higher than the current density used in laboratory experiments of the order $10^{-3} \sim 10^{-6}$ A/cm^2 [217]. Though, this is 100 times slower than the one used for delithiation of a similar block but $1/5^{th}$ in size (2.4 nm) as compared to the size of simulation cell (11 nm) used in this work [217]. They have roughly estimated that it takes $\approx$ 1 ps to equilibrate the change in concentration ($\Delta c \approx 3\%$ due to 100 Li atoms) for a cell of 2.4 nm thick. As the simulation cell in the current work is larger Δc will be smaller for 100 Li atoms removal and thus we suggest that 100 ps is large enough to equilibrate the structure.

In order to have a concentration gradient similar to using a buffer layer, an extra 20 Å vacuum layer is added on both sides of the cell along the x axis, along which the delithiation will take place and the system is allowed to evolve during MD steps within NVT ensemble. At each delithiation step, a dynamic shell of 5 Å thickness is created on the either edge of the atoms, from which 100 atoms are removed randomly as shown in Fig. 5.3. This creates a concentration gradient of Li atoms between the center and at the edge of the box and the added vacuum will amplify this gradient. During MD run, the Li atoms from center will diffuse towards the edge and will produce a homogenized structure for the next delithiation step. If there are less than 100 atoms in this buffer zone at any stage, then all the atoms are removed from the shell.

5.3 DELITHIATED SILICON

Fig. 5.4 shows a snapshot of initial delithiation setup (top) and after 30 delithiation steps(below). After repeating 90 such delithiation steps, the completely delithiated Si structure has been obtained. The delithiated structure is again quenched to 300 K under NVT thermostat followed by a CG minimization for further

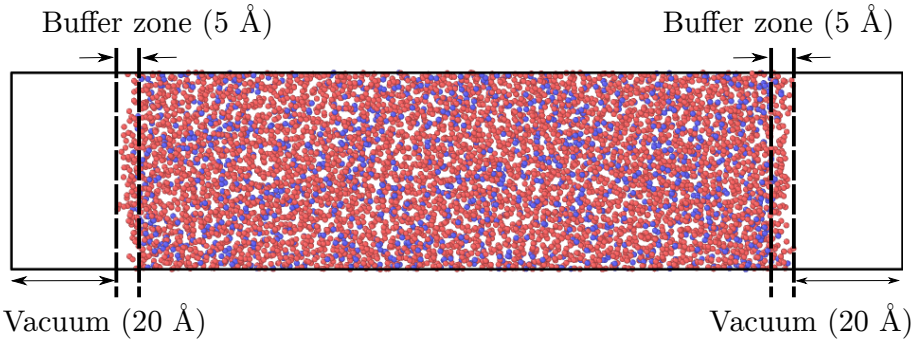

Figure 5.3: Illustration showing the vacuum of 20 Å added on either side of the simulation cell for creating Li concentration gradient when Li atoms are removed from the buffer zone at each delithiation step.

characterization. As a vacuum layer was used to facilitate delith-

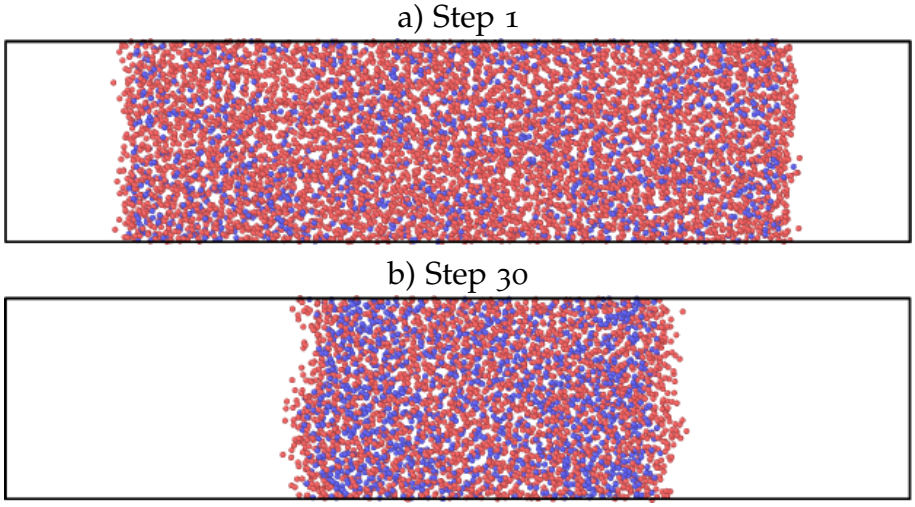

Figure 5.4: Snapshot of a-$Li_{15}Si_4$ delithiation at a) Step 1 and at b) Step 30 conducted under NVT ensemble at 1200 K. Li atoms are marked by red and Si atoms by blue spheres. Noticeable volume change can be observed in 30 delithiation steps.

iation, density calculation was not straightforward and thus an approximation was used. The cell dimension along the diffusion direction is discretized into a range of point and at each such

point z, with a pre-defined width w, a local density centered at z, $\rho_w(\bar{z})$ is obtained as:

$$\rho_w(\bar{z}) = \frac{n_{Li}m_{Li} + n_{Si}m_{Si}}{2wA_s} \times 1.66 \tag{5.3}$$

where m_{Li} and m_{Si} are the mass of Li and Si atoms in the atomic mass unit (a.m.u), respectively and thus 1.66 is multiplied to convert the density into g/cm^3. A_s is the cross sectional area of the slice. This results in a noisy density curve, which was then averaged to obtain the approximate density of the delithiated Si structure. Fig. 5.5 shows the delithiated structure and the calculation of average density from the local density $\rho_w(\bar{z})$.

The average density calculated from the above-mentioned method is $2.23 \pm 0.05\,g/cm^3$, which is close to the density of a-Si reported experimentally, i.e. $2.28\,g/cm^3$ [233]. However, the average density of a-Si computed with MEAM potential separately is $2.52\,g/cm^3$, which suggests that with respect to MEAM potential, the delithiated structure is loosely bonded as compared to a-Si. Though the RDF (refer Fig. 5.6) of a-Si (orange) and delithiated Si (blue) looks very similar (at 300 K), both having their first peak at ~2.45 Å. For the second peak there is a peak shift of ≈0.2 Å. The a-Si has its second peak at 3.95 Å, while the delithiated Si has the second peak at roughly 4.1 Å. The third peak is also shifted a bit on right, which agrees with a lower density as compared to a-Si. The RDF peaks of a partially delithiated a-$Li_{0.5}Si$ structure (green), from another study [76], are much more shifted to the right owing to the entrapped Li atoms and comparatively loosely bonded structure. Even the first peak is shifted by 1 Å to the right.

Nonetheless, MEAM potential was developed to study bulk properties of silicon and is not the best to replicate liquid silicon [152, 154]. As compared to the experimental data of a-Si (grey), there is significant peak broadening at the base. The second peak of the experimental data is at 3.8, i.e. a shift of 1 Å as well as the height of the second and the third peak is significantly lower in height. Cook *et al.* [154] has summarized these shortcomings of MEAM potential in depicting a-Si structure in a comparat-

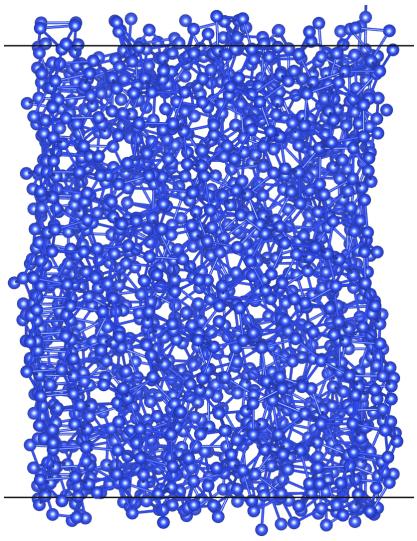

a) Structure of completely delithiated Si

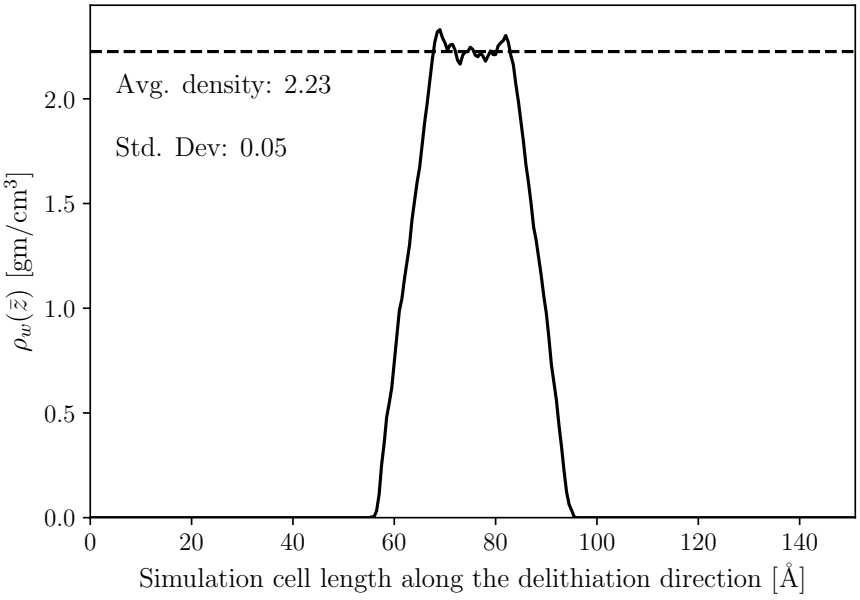

b) Local density profile computed with a slice of width 6 Å

Figure 5.5: Completely delithiated Si structure (a). Plot of local density profile to estimate the average density of the delithiated structure (b). The above structure is not up to scale and is enlarged for visual inspection.

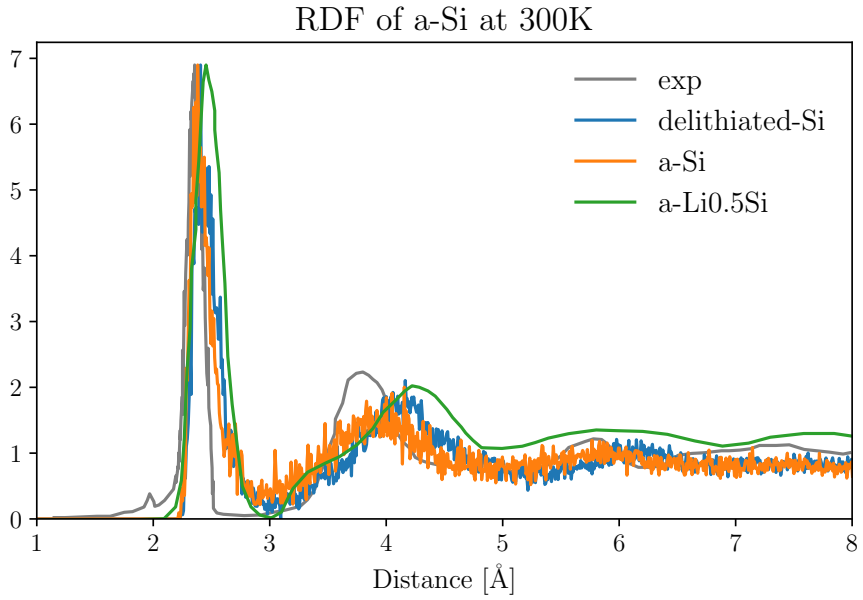

Figure 5.6: Radial Distribution Functions plotted for a-Si (orange) and delithiated Si (blue) obtained with the M1 potential along with the experimental data of a-Si (grey) for comparison [144, 227]. Green curve represents the RDF plot from another delithiation study on SiNW using Reaxff by Jung *et al.* [76]. RDF intensities are scaled to match the first peak height.

ive study of Tersoff, Stillinger-Weber (SW) and MEAM potential. Fig. 5.7 shows a comparative RDF of a-Si at 300 K obtained with these three potentials. It can be seen that, only Tersoff potential provide a clear peak separation, both SW and MEAM fail to do so and the former even has a signifcant shoulder to the first peak. As noticed while comparing with the experimental data, the second peak is shifted to the right as well as the peak height of second and third peaks are relatively smaller. Although Tersoff and SW give better results, they are limited to study pure Si and thus knowing the limitations of MEAM potential, one can draw useful insights about Li-Si interaction.

The shortcomings of MEAM potentials confirm that the discrepancy in the RDF of a-Si computed in this work as compared

to the experimental data is due to the limitation of the MEAM potential. The closeness in RDF between a-Si and delithiated Si also strongly indicates that the delithiated Si has a close resemblance to a-Si, which we further confirmed by performing the rings analysis.

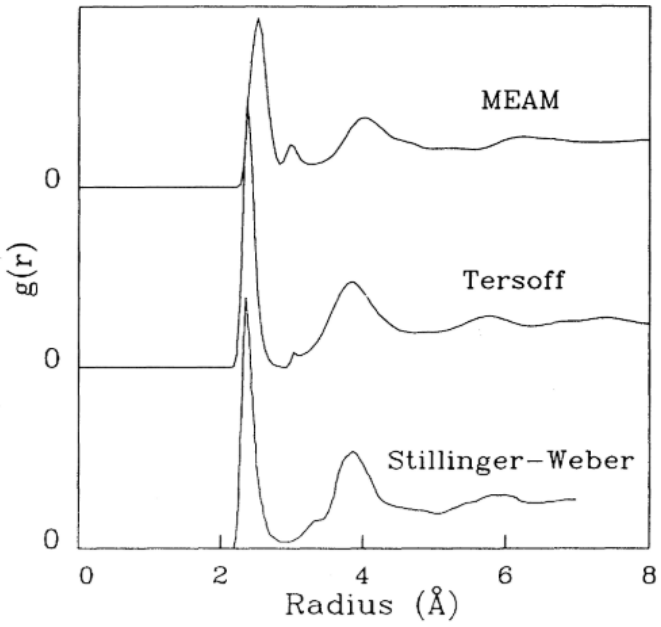

Figure 5.7: Comparison of a-Si RDF produced with MEAM potential, Tersoff and Stillinger-Weber at 300 K. Reprinted figure with permission from Ref. [154]. Copyright 1993 by the American Physical Society.

Fig. 5.8 shows the statistics of rings analysis performed on a-Si phases obtained from classical potentials, from first-principles and also some reference first-principles data on a-Si. All the a-Si structures produced with classical potentials (MEAM [153] and SW [142]) have very similar distributions and the DFT data agrees more closely with the the reference DFT data of Johari *et al.* [178]. Perhaps this can be attributed to the restriction of number of atoms in the first-principles calculations due to which there is not enough statistics. Even within the DFT data, the a-Si structure with 64 atoms shows some distribution on either extremes (10 member and 3 member rings), while the 8 atom

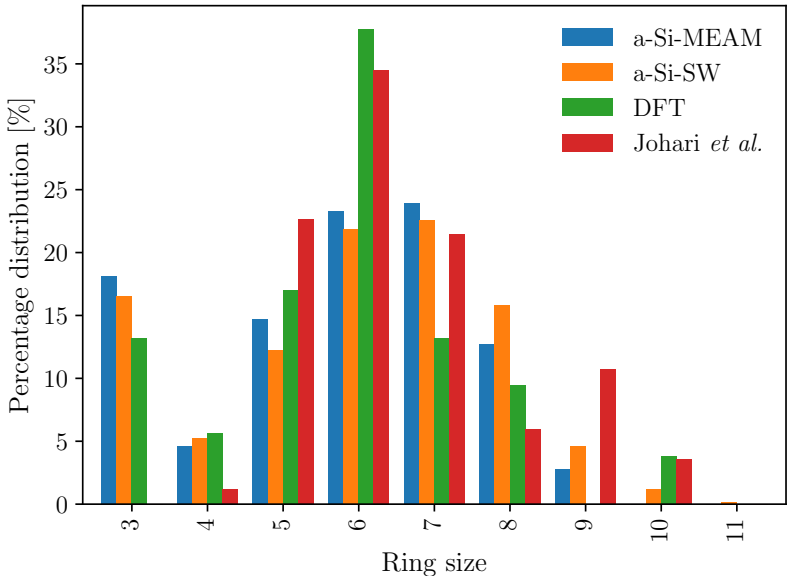

Figure 5.8: Statistics of rings analysis for a-Si and delithiated Si studied with MEAM potential [153] and a-Si obtained with Stillinger-Weber [142]. DFT data from delithiated structure (8 Si atoms cell) obtained in the previous Chapter is also plotted for comparison along with another *ab-initio* data on 64 atoms Si cell from Johari *et al.* [178].

DFT data from delithiated Si peaks doesn't show such a spread. Nevertheless, rings analysis augment the analysis from density computation and RDF analysis that delithiated Si resembles very close to a-Si. One can in principle performs more sophisticated study on the statistical analysis of local environments of a-Si and delithiated Si using chemenv as we did in the last chapter. It will provide more useful insight about how similar or different are the local environment of Si in both these cases and how it will affect the relithiation and cyclic capacity loss in LIBs.

6

CONCLUSIONS AND PERSPECTIVE

The scientific investigation of silicon-based anode materials is challenging from the application point of view as well as from fundamental understanding. Over the years, researchers have contributed by proposing innovative solutions from application side by using nanoparticles or nanocomposites, or by providing new theoretical/experimental tools for probing materials. Either way, we are moving closer every day to have a better understanding of how silicon-based anodes expands on lithiation and its effect on Li diffusivity or vice versa. A fundamental understanding of this interplay between Li transport and structural change in silicon can enable us to accurately design next-generation batteries. In this thesis, we tried to address both the issues: studying diffusion of Li in Li_xSi and analysing the change in the local environment of Si during lithiation/delithiation. As the former project was oriented towards assessing limitations of approximations while the motivation for the latter was from a physical understanding of the process, this thesis contains technically as well as physically oriented results and discussions. For this purpose, we used first-principles calculations as well as the classical empirical potentials, discussing their limitations and their potential applications. The main outcomes, challenges and future perspectives will be summarized in what follows.

From a methodical point of view, the transition-state-theory-based framework has been exploited to accurately describe Li diffusivity in bulk Si. The two main ingredients required for this: diffusion energy barrier and jump rate were obtained by the nudged elastic band method and phonon frequencies at the initial and the saddle point. Phonon frequencies were calculated by Abipy workflow within Density-Functional Perturbation Theory framework. In our work we recalled that the famous Arrhenius equation of diffusion, often used to measure diffusivity is in fact a special case of a more generic diffusion equation that arises from quantization of phonons. However, the input para-

meters for both definitions: quantum and classical approximations are the same, the simpler form of the latter seems more convenient for fitting the data. Nevertheless, we showed that at no additional computational cost, a more accurate description of diffusivity can be obtained. Furthermore, we have also applied this method on Li diffusivity in c-LiSi with multiple (6) jumps, in which case we developed a kinetic Monte Carlo-based computation to get the effective diffusion coefficient.

The low temperature quantum tunnelling effects and the high temperature anharmonic effects were also analyzed. The former is included by the Fermann and Auerbach model to include incoherent tunneling and the latter by the cBΩ model as well as the quasiharmonic approximation. The Fermann and Auerbach model treat incoherent tunneling also as a barrier jump and is augmented to the diffusion equation as a multiplier factor that goes to 1 as its approaching the classical limit. The cBΩ model relates the diffusion energy barrier to the bulk modulus (B) and the volume per atom (Ω). As both depend on temperature, the model brings a temperature-dependent energy barrier corresponding to the anharmonic effects in the system. On the other hand, the quasiharmonic approximation only rely on the first-order dependence on the volume. These methods are explained in detail in Chapter 2

The effect of these approximations on diffusivity has been analyzed. Firstly, we observed that the quantum tunneling effects, which significantly deviate proton diffusivity from the Arrhenius equation even at room temperature, are not that significant for Li atoms because of the heavier mass of Li atoms. Though they decrease the diffusivity values by 30% near room temperature, which has not been estimated yet for the Li-Si case. The anharmonic effects are also relatively small, although they increase the diffusion coefficient by 66%. In case of Li diffusion in c-LiSi, the quantum effects were negligible and the anharmonic effects were inconclusive. We have also discussed the limitations of these models and underlying assumptions in Chapter 3.

After developing the theoretical understanding from Chapter 2 and 3, a novel first-principles-based delithiation routine has been

developed and tested for the delithiation of c-$Li_{13}Si_4$ in Chapter 4. The study was motivated by the step-by-step delithiation process proposed by Chevrier *et al.* [75], with a modification to include full structural relaxation in between two steps, instead of fix volume scaling. A full structural relaxation will allow the structure to access the minima of the energy landscape. Furthermore 50 steps of molecular dynamics were included to remove any anharmonicity in the system due to removal of a Li atom. The whole flow was automated using Abipy and Pymatgen libraries for efficient computations.

We observed that at a certain lithiation level, the formation of an extra Si-Si dimer was associated with a sudden drop in the formation energy as well as the average coordination number of Si atoms. Moreover, the local environment of the delithiated structure was also studied by chemenv tool that showed 75% of the Si atoms return back to the tetrahedral coordination environment. Further comparison to a-Si was not possible due to limited cell size and thus an empirical-potential-based method was adopted in Chapter 4 that can enable a large scale simulation to find the resemblance between a-Si and the fully delithiated Si. For this purpose 2NN MEAM potential was validated and used to study the delithiation of a-$Li_{15}Si_4$ by using a shell method of removing 100 atoms followed by few MD steps for relaxation. Through this approach, we obtained a big supercell of delithiated Si that was characterized by density, RDF and rings statistics suggesting a strong resemblance to a-Si structure.

The first technical issue we faced in this study was the structural relaxation in ABINIT far from equilibrium during step-by-step Li removal. The flow has to be monitored manually and debug for errors related to structural relaxation possibly due to some numerical error that blows out. Similar limitation was mentioned by Chevrier *et al.* [75] as well to avoid full structural relaxation.

Comparative limitations of *ab-initio* methods have been discussed briefly in Chapter 4 and 5. It is important to find the correct balance between accuracy and compute efficiency. However, especially for the empirical potentials, proper validation

and testing has to be performed before starting to use them in a project. We had started with the Reactive force-field (Reaxff) to study the lithiation-delithiation kinetics in Li-Si system. Reaxff has performed quite well in terms of hydrocarbons and also for metals like Al, Si, Li, etc. However, its complicated form with several parameters makes it difficult to tune and limit its portability. Thus, we selected a simpler MEAM potential, which worked well within the domain of interest.

These limitations also open doors to future opportunities and scope of the project. On a broader view, several preliminary studies introduced in in Chapter 4 and Chapter 5 can provide a sound basis for a thorough analysis. For instance, the delithiation process tested in Chapter 4 can be used on a bigger supercell to get better statistics on delithiated Si atoms. Or to try an amorphous Li_xSi case, which might provide a better comparison with the experimental data without a jump in the coordination number curve. Silicon atoms in such a relatively open structure might evolve in a different way and the local environment of the fullly delithiated Si forms different proportion of coordination geometry. Some studies have already explored the lithiation-delithiation dynamics. However, a careful study of the change in the local environment of Si atoms in different lithiation/delithiation condition is still largely unexplored.

Another direction to proceed is to build up on the information provided in Chapter 3 to study diffusion of Li in bulk Si with defects. Understanding the effect of defects on transport properties are exciting to design and tune materials [72]. One can also perhaps explore the design of silicon entrapped by graphene as a battery material, something which is tested experimentally but not yet explored fully from a theoretical point of view [234]. It could be interesting to study the diffusion pathway of Li atom in a silicon-graphene heterostructure and how it is affected by the layers of graphene/silicon [28, 235–237]. How the presence of graphene increases or decreases the diffusion of Li atom, or during delithiation of such a heterostructure, what can be the rate limiting step? On a similar line of thought, phosphorene-graphene heterostructures are also of interest for

battery applications owing to high stability, cyclability and specific capacity [32, 238]. These are some of the questions worth looking for answers in order to provide a significant contribution in the field of electrochemical energy storing devices.

A

CONVERGENCE RESULTS

This Appendix contains additional plots for convergence tests and supplementary material of Chapter 3

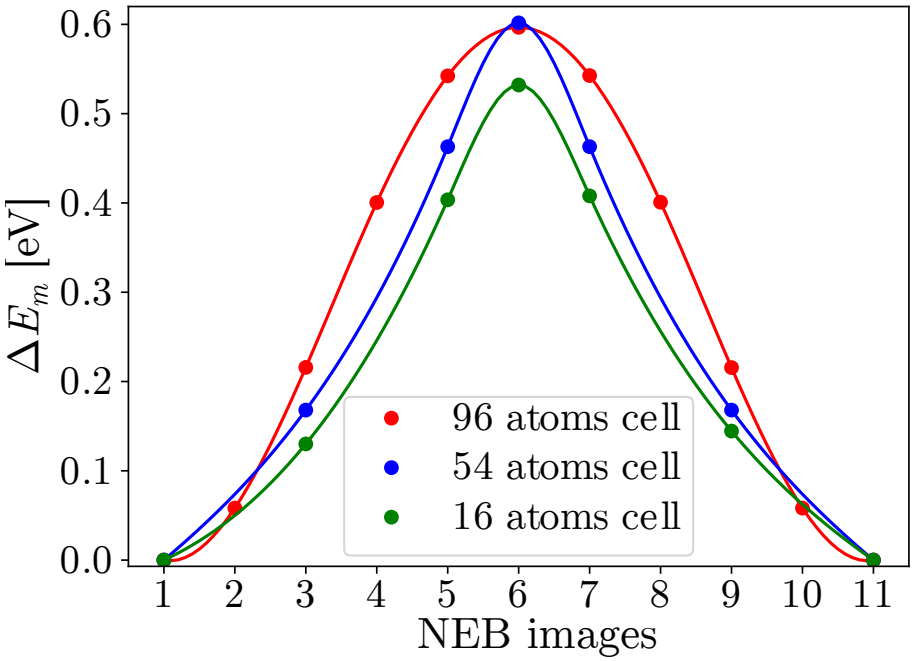

Figure A.1: Diffusion barrier for one interstitial Li atom to jump to adjacent interstitial position in bulk Si for varying supercell size.

Table A.1: Calculated Li migration energy barriers in different supercell size along with values reported in the literature.

Jump	E_b(eV)			
	31-atoms	63-atoms	127-atoms	Ref.[129]
Vac-Li1	0.242	0.266	0.247	0.252
Vac-Li2	0.218	0.247	0.261	0.235
Vac-Li4	0.439	0.428	0.430	0.466
Vac-Li6	0.281	0.259	0.252	0.272

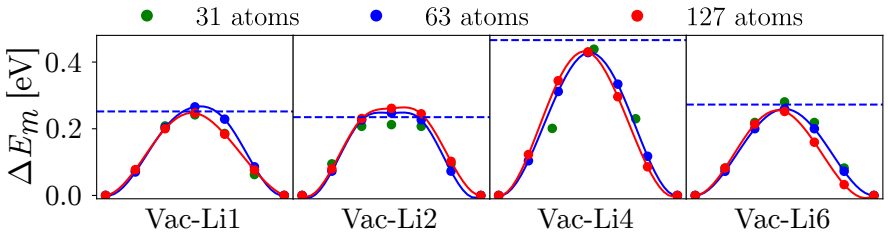

Figure A.2: Minimum energy paths for lithium vacancy diffusion in LiSi with varying supercell size. The solid horizontal line indicates the value reported in literature [129] (Refer Fig. 3.18 and Table 3.1 for nomenclature associated with the type of jump).

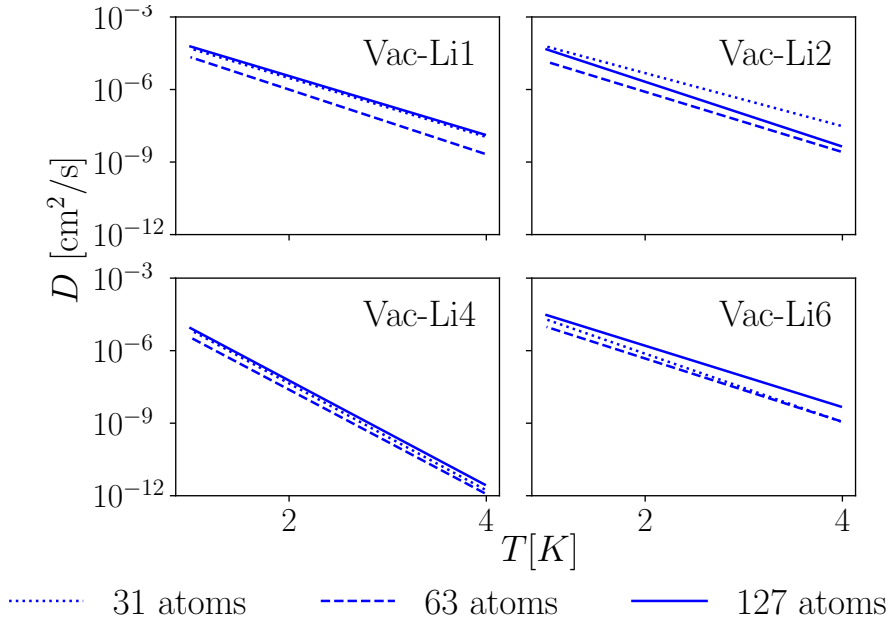

Figure A.3: Temperature dependence of the diffusion coefficient calculated for all the four types of Li vacancy jumps in LiSi with varying supercell size.

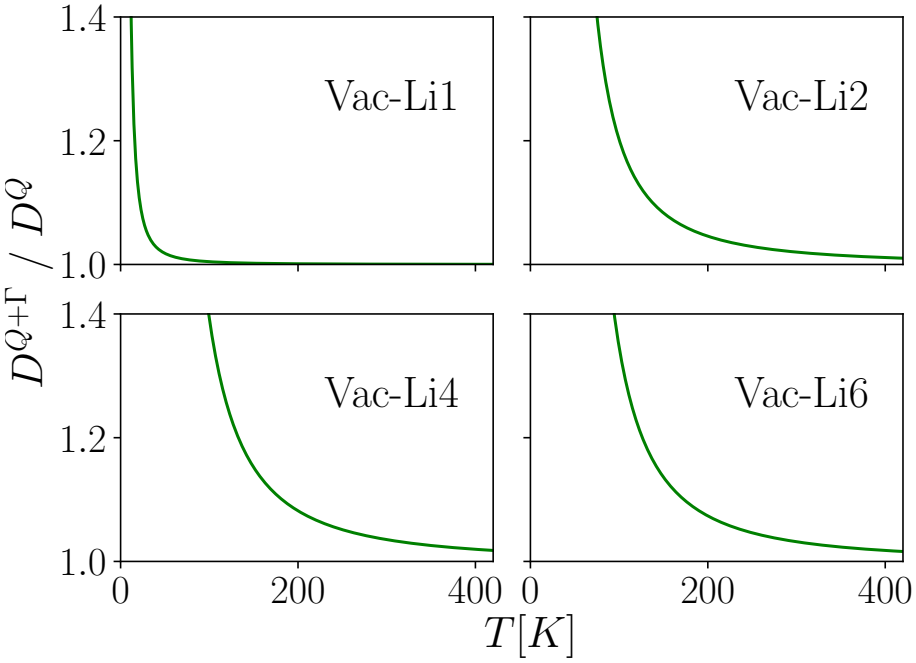

Figure A.4: Effect of including the quantum tunneling correction on the diffusion coefficient measured as a ratio of $D_{Q+\Gamma}/D_{Q}$ has been plotted as a function of temperature for all the four types of Li vacancy jumps.

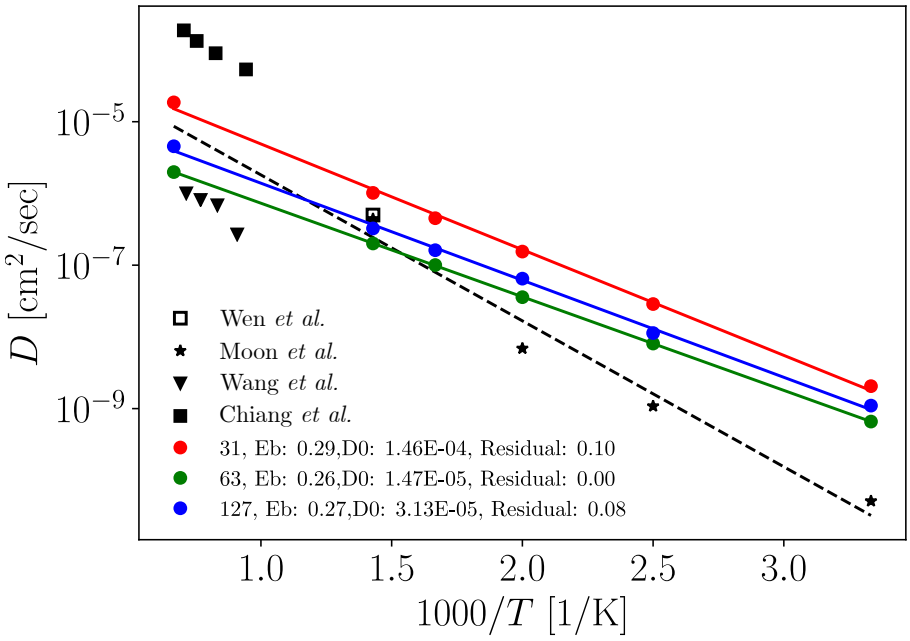

Figure A.5: Temperature dependence of the overall diffusion coefficient obtained using KMC simulation for a) 31 (green), b) 63 (blue), and c) 127 (red) atoms LiSi cell. Black Markers indicate previous experimental [62] and theoretical results [129, 174, 176].

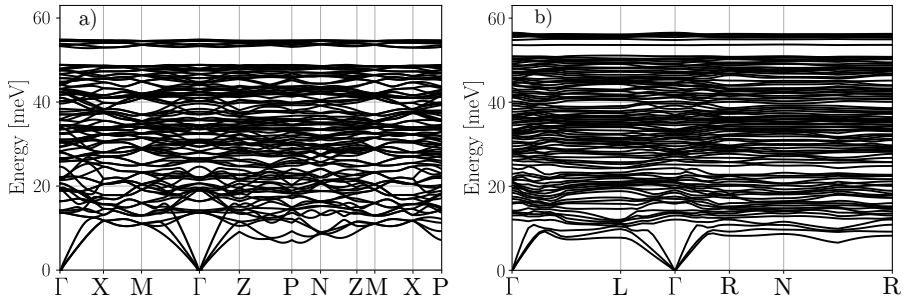

Figure A.6: Phonon band structures of a) bulk LiSi structure (32 atoms), and b) LiSi structure with one Li vacancy (31 atoms). These small-cell results are shown for illustration purpose only.

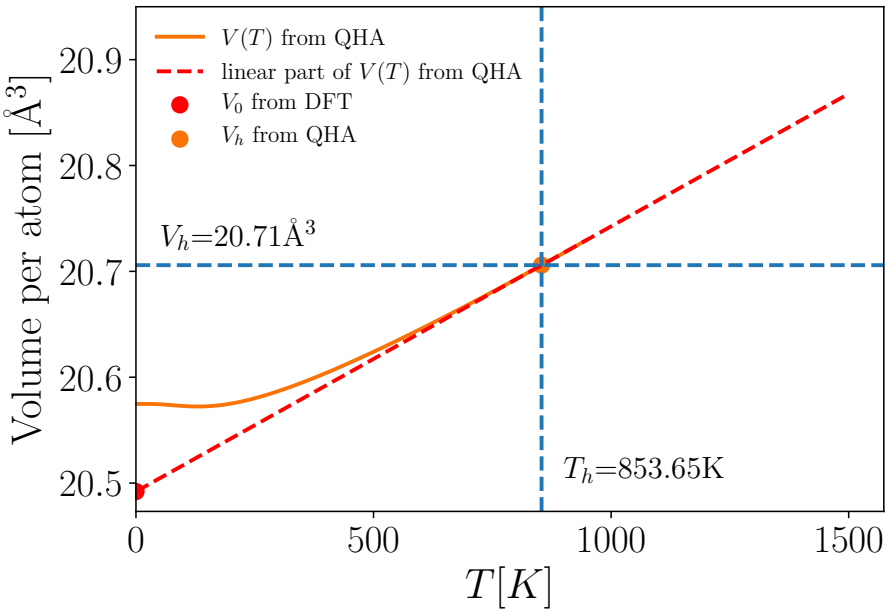

Figure A.7: Temperature dependence of the volume of bulk Si (orange curve) obtained from the first-principles calculations of Ref. [71]. The dashed (red) line represents the linear part of the high temperature approximation and dots are the DFT calculated values at equilibrium volume (red dot) and at 20.71 Å^3 (orange dot), corresponding to 853.65 K.

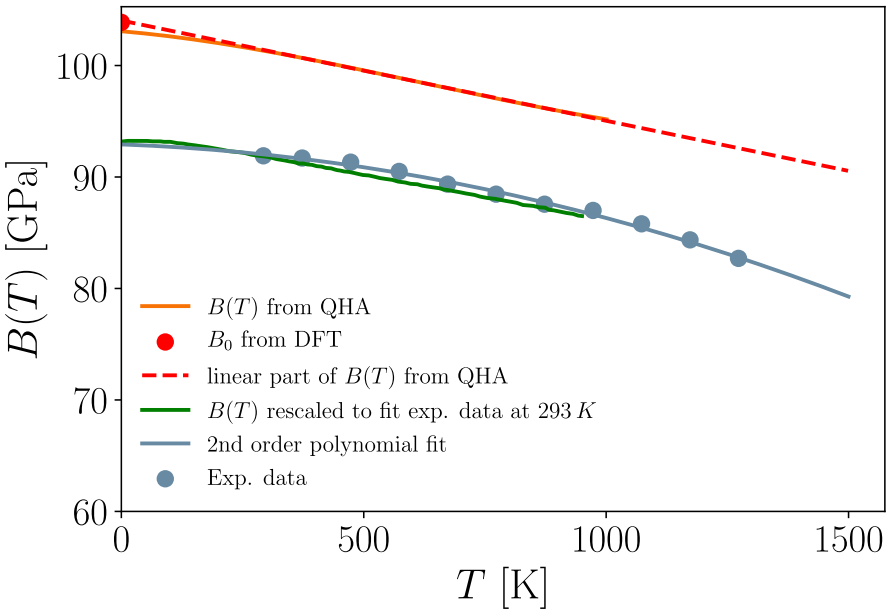

Figure A.8: Temperature dependence of the theoretical bulk modulus for bulk Si (orange curve) obtained from the first-principles calculations of Ref. [71]. The dashed (red) line represents the linear part of high temperature approximation and the green curve is the rescaled one to match the room temperature experimental values (blue dots) from Ref. [239].

B

COORDINATION ENVIRONMENTS

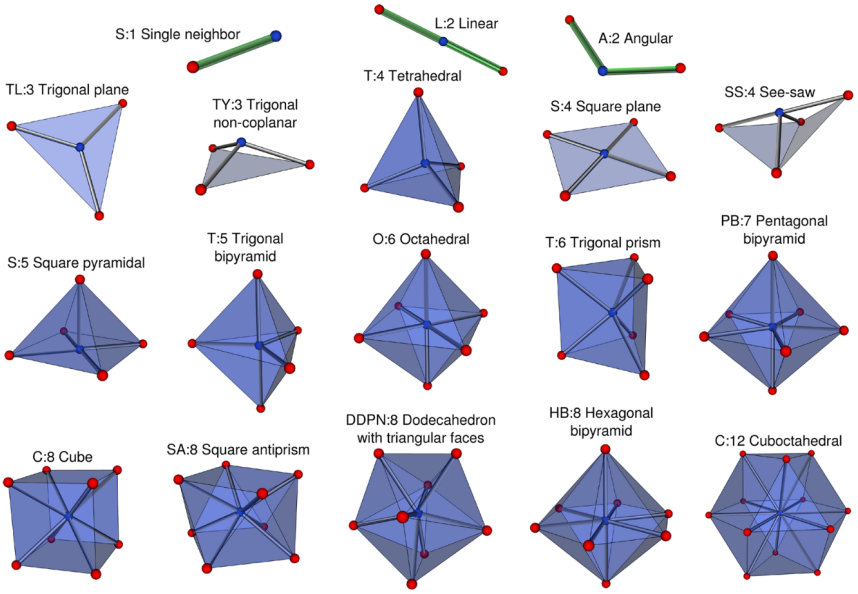

Figure B.1: Illustration of most commonly identified coordination environments. Reprinted with permission from Ref. [156]. Copyright 2017 American Chemical Society.

C

SCIENTIFIC COMMUNICATION

PEER-REVIEWED JOURNAL PUBLICATIONS

- **Kumar, V.**, Di Stefano, D., Rignanese, G-M., and Gonze, X.,"First-principles investigation of Li diffusion in Si and LiSi including nuclear quantum effects," (*submitted in J. Chem. Phys.*)
- Sandhu, G., Coulombier, M., **Kumar, V.**, Kassa, H. G., Avram, I., Ye, R., Stopin, A.,Bonifazi, D., Gohy, J-F., Leclère, P., Gonze, X., Pardoen, T., Vlad, A., Melinte, S., "Kinked silicon nanowires-enabled interweaving electrode configuration for lithium-ion batteries," *Scientific Reports* **8**:9794, 2018, doi:10.1038/s41598-018-28108-3

ORAL PRESENTATIONS

- BATWAL Annual Meeting 2019, Liège, (Belgium), Oct 7, 2019.
- IMCN Ph.D. Day, Louvain la Neuve (Belgium), May 25, 2018.
- 233rd ECS Meeting, Seattle, WA (USA), May 13-17, 2018.
- DPG Spring Meeting, Berlin (Germany), Mar 11-16, 2018.

POSTERS

- IMCN Ph.D. Day, Louvain la Neuve (Belgium), May 29, 2019.
- 14^{th} ETSF Young Researcher Meeting, Tarragona (Spain), June 5-9, 2017.
- CECAM summer school, Laussane (Switzerland), June 12-16, 2017.
- IMCN Ph.D. Day, Louvain la Neuve (Belgium), May 24, 2017.

OTHER ACTIVITIES

- CECI training on High Performance Scientific Computing, Oct-Nov, 2016.
- ICTP Summer school on Multiscale Computational Modelling of Materials for Energy Applications, Trieste (Italy), July 4-15, 2016.

BIBLIOGRAPHY

[1] J. Cook *et al.*, Environmental Research Letters **8** (2013).

[2] J. Cook et al., Environmental Research Letters **11** (2016).

[3] D. Lüthi, M. Le Floch, B. Bereiter, T. Blunier, J. M. Barnola, U. Siegenthaler, D. Raynaud, J. Jouzel, H. Fischer, K. Kawamura, and T. F. Stocker, Nature **453**, 379 (2008).

[4] R. S. Nerem *et al.*, Proc. Natl. Acad. Sci. U. S. A. **115**, 2022 (2018).

[5] T. F. Stocker et al., 'IPCC, 2013: Climate Change 2013: The Physical Science Basis. Contribution of Working Group I to the Fifth Assessment Report of the Intergovernmental Panel on Climate Change.' (2013), https://www.ipcc.ch/report/ar5/wg1/.

[6] 'Climate Change: How Do We Know?' https://climate.nasa.gov/evidence/, accessed: 2020-01-5.

[7] A. Raftery et al., Nat. Clim. Change **7**, 637–641 (2017).

[8] R. Millar *et al.*, Nat. Geosci. **10**, 741–747 (2017).

[9] G. J. Hedley, A. Ruseckas, and I. D. W. Samuel, Chemical Reviews **117**, 796 (2017), pMID: 27951633, https://doi.org/10.1021/acs.chemrev.6b00215 .

[10] Y. H. Cho, S. Booh, E. Cho, H. Lee, and J. Shin, APL Mater. **5** (2017), 10.1063/1.4997978.

[11] F.-h. Du, K.-x. Wang, and J.-s. Chen, J. Mater. Chem. A Mater. energy Sustain. **00**, 1 (2015).

[12] Y. Mekonnen, A. Sundararajan, and A. I. Sarwat, in *SoutheastCon 2016* (2016) pp. 1–6.

[13] J. M. Tarascon, J. M. Tarascon, M. Armand, and M. Armand, Nature **414**, 359 (2001).

[14] X. Zuo, J. Zhu, P. Müller-Buschbaum, and Y.-J. Cheng, Nano Energy **31**, 113 (2017).

[15] D. Ouyang, M. Chen, Q. Huang, J. Weng, Z. Wang, and J. Wang, Applied Sciences (Switzerland) **9** (2019).

[16] D. Lisbona and T. Snee, Process Saf. Environ. **89**, 434 (2011).

[17] J. B. Goodenough and Y. Kim, Chem. Mater. **22**, 587 (2010).

[18] Y. A. Du and N. A. W. Holzwarth, Phys. Rev. B **76**, 174302 (2007).

[19] M. S. Islam and C. A. J. Fisher, Chem. Soc. Rev. **43**, 185 (2014).

[20] H. Aral and A. Vecchio-Sadus, Ecotox. Environ. Saf. **70**, 349 (2008).

[21] 'Nobel Prize in Chemistry 2019,' (Oct, 2019), https://www.nobelprize.org/prizes/chemistry/2019/.

[22] D. Deng, Energy Sci. Eng. **3**, 385 (2015).

[23] D. Di Stefano et al., Chem **5**, 2450 (2019), 1708.02997 .

[24] M. Osiak, H. Geaney, E. Armstrong, and C. O'Dwyer, J. Mater. Chem. A **2**, 9433 (2014).

[25] F. Zheng, M. Kotobuki, S. Song, M. O. Lai, and L. Lu, J. Power Sources **389**, 198 (2018).

[26] A. Mukhopadhyay and B. W. Sheldon, Prog. Mater. Sci. **63**, 58 (2014).

[27] H. Wu and Y. Cui, Nano Today **7**, 414 (2012).

[28] H. Wang, M. Wu, X. Lei, Z. Tian, B. Xu, K. Huang, and C. Ouyang, Nano Energy **49**, 67 (2018).

[29] R. Fong, U. VonSacken, and J. R. Dahn, Journal of the Electrochemical Society **137**, 2009 (1990).

[30] N. Nitta, F. Wu, J. T. Lee, and G. Yushin, Mater. Today **18**, 252 (2015).

[31] V. L. Chevrier, J. W. Zwanziger, and J. R. Dahn, J. Alloys Compd. **496**, 25 (2010).

[32] J. Sun, H. W. Lee, M. Pasta, H. Yuan, G. Zheng, Y. Sun, Y. Li, and Y. Cui, Nat. Nanotechnol. **10**, 980 (2015).

[33] M. N. Obrovac, L. Christensen, D. B. Le, and J. R. Dahn, J. Electrochem. Soc. **154**, A849 (2007).

[34] J. Li and J. R. Dahn, J. Electrochem. Soc. **154**, 156 (2007).

[35] B. Liang, Y. Liu, and Y. Xu, J. Power Sources **267**, 469 (2014).

[36] X. H. Liu et al., Nano Lett. **11**, 3312 (2011).

[37] M. K. Y. Chan, C. Wolverton, and J. P. Greeley, J. Am. Chem. Soc. **134**, 14362 (2012).

[38] L. Q. Zhang, X. H. Liu, Y. Liu, S. Huang, T. Zhu, L. Gui, S. X. Mao, Z. Z. Ye, C. M. Wang, J. P. Sullivan, and J. Y. Huang, ACS Nano **5**, 4800 (2011).

[39] M. Whittingham, Science **192**, 1126 (1976).

[40] C.-M. Park, J.-H. Kim, H. Kim, and H.-J. Sohn, Chem. Soc. Rev. **39**, 3115 (2010).

[41] C. K. Chan, H. Peng, G. Liu, K. Mcilwrath, X. F. Zhang, R. A. Huggins, and Y. Cui, Nat. Nanotechnol. , 31 (2007).

[42] J. R. Szczech and S. Jin, Energy Environ. Sci. **4**, 56 (2011).

[43] C. K. Chan, H. Peng, G. Liu, K. McIlwrath, X. F. Zhang, R. A. Huggins, and Y. Cui, Nat. Nanotechnol. **3**, 31 (2008).

[44] S. Misra, N. Liu, J. Nelson, S. S. Hong, Y. Cui, and M. F. Toney, ACS Nano , 5465 (2012).

[45] J. H. Cho and S. T. Picraux, Nano Lett. **14**, 3088 (2014).

[46] J. Luo, X. Zhao, J. Wu, H. D. Jang, H. H. Kung, and J. Huang, J. Phys. Chem. Lett. **3**, 1824 (2012).

[47] G. Sandu, L. Brassart, J. F. Gohy, T. Pardoen, S. Melinte, and A. Vlad, ACS Nano **8**, 9427 (2014).

[48] N. Liu, H. Wu, M. T. McDowell, Y. Yao, C. Wang, and Y. Cui, Nano Lett. **12**, 3315 (2012).

[49] X. Zhao, X. Rui, W. Zhou, L. Tan, Q. Yan, Z. Lu, and H. H. Hng, J. Power Sources **250**, 160 (2014).

[50] G. Sandu et al., Sci. Rep. **8**, 9794 (2018).

[51] M. J. Chon, V. A. Sethuraman, A. McCormick, V. Srinivasan, and P. R. Guduru, Phys. Rev. Lett. **107**, 1 (2011).

[52] M. T. McDowell, S. W. Lee, J. T. Harris, B. A. Korgel, C. Wang, W. D. Nix, and Y. Cui, Nano Lett. **13**, 758 (2013).

[53] J. W. Wang, Y. He, F. Fan, X. H. Liu, S. Xia, Y. Liu, C. T. Harris, H. Li, J. Y. Huang, S. X. Mao, and T. Zhu, Nano Lett. **13**, 709 (2013).

[54] C. Y. Chou and G. S. Hwang, Appl. Surf. Sci. **323**, 78 (2014).

[55] M. Pharr, K. Zhao, X. Wang, Z. Suo, and J. J. Vlassak, Nano Lett. **12**, 5039 (2012).

[56] X. Zhang, S. W. Lee, H. W. Lee, Y. Cui, and C. Linder, Extrem. Mech. Lett. **4**, 61 (2015).

[57] X. H. Liu, L. Zhong, S. Huang, S. X. Mao, T. Zhu, and J. Y. Huang, ACS Nano **6**, 1522 (2012).

[58] P. Haldar and A. Chatterjee, Energy Procedia **54**, 310 (2014).

[59] J. Kim, Y. H. Kim, S. H. Choi, and W. Lee, ACS Nano **5**, 5242 (2011).

[60] W. Wan, Q. Zhang, Y. Cui, and E. Wang, J. Phys. Condens. Matter **22**, 415501 (2010).

[61] E. M. Pell, Phys. Rev. **119**, 1014 (1960).

[62] C. J. Wen and R. A. Huggins, J. Solid State Chem. **37**, 271 (1981).

[63] N. Balke, S. Jesse, Y. Kim, L. Adamczyk, A. Tselev, I. N. Ivanov, N. J. Dudney, and S. V. Kalinin, Nano Lett. **10**, 3420 (2010).

[64] Y. Ding and J. Ni, Appl. Phys. Lett. **95**, 083115 (2009).

[65] A. Kuhn, P. Sreeraj, P. Rainer, H.-d. Wiemh, P. Heitjans, R. Pottgen, H. D. Wiemhofer, M. Wilkening, and P. Heitjans, J. Am. Chem. Soc. **133**, 11018 (2011).

[66] K. Yoshimura, J. Suzuki, K. Sekine, and T. Takamura, J. Power Sources **174**, 653 (2007).

[67] H. Mehrer, *Diffusion in Solids* (Springer, Berlin, Heidelberg, 2007) Chap. 7, pp. 105–125.

[68] D. Di Stefano, M. Mrovec, and C. Elsässer, Phys. Rev. B **92**, 224301 (2015).

[69] B. Cheng, A. T. Paxton, and M. Ceriotti, Phys. Rev. Lett. **120**, 225901 (2018).

[70] K. Toyoura, Y. Koyama, A. Kuwabara, F. Oba, and I. Tanaka, Phys. Rev. B **78**, 214303 (2008).

[71] G.-M. Rignanese, J.-P. Michenaud, and X. Gonze, Phys. Rev. B **53**, 4488 (1996).

[72] D. S. Kim, H. L. Smith, J. L. Niedziela, C. W. Li, D. L. Abernathy, and B. Fultz, Phys. Rev. B **91**, 014307 (2015).

[73] V. Saltas, A. Chroneos, and F. Vallianatos, Mater. Chem. Phys. **181**, 204 (2016).

[74] Q. Zhang, Y. Cui, and E. Wang, Model. Simul. Mater. Sci. Eng. **21**, 074001 (2013).

[75] V. L. Chevrier and J. R. Dahn, J. Electrochem. Soc. **156**, A454 (2009).

[76] H. Jung, M. Lee, B. C. Yeo, K. R. Lee, and S. S. Han, J. Phys. Chem. C **119**, 3447 (2015).

[77] X. Gonze, Phys. Rev. A **52** (1995).

[78] S. Baroni, P. Gianozzi, and A. Testa, Phys. Rev. Lett. **58**, 1861 (1987).

[79] M. Born and R. Oppenheimer, Zur Quantentheorie der Molekeln Annalen der Physik **84**, 457 (1927).

[80] R. M. Dreizler and E. K. U. Gross, *Density Functional Theory* (Springer-Verlag Berlin Heidelberg, 1990).

[81] R. M. Martin, *Electronic Structure: Basic Theory and Practical Methods* (Cambridge University Press, 2004).

[82] G. Antonius, S. Poncé, E. Lantagne-Hurtubise, G. Auclair, X. Gonze, and M. Côté, Phys. Rev. B **92**, 085137 (2015).

[83] E. del Corro et al., Nano Lett. **16**, 2363 (2016).

[84] Y. Gillet, S. Kontur, M. Giantomassi, C. Draxl, and X. Gonze, Sci. Rep. **7**, 7344 (2017).

[85] A. Erba, J. Baima, I. Bush, R. Orlando, and R. Dovesi, J. Chem. Theory Comput. **13**, 5019 (2017).

[86] P. Giannozzi, G. Grosso, and G. Parravicini, Riv. Nuovo Cim. **13**, 1–80 (1990).

[87] X. Gonze, Phys. Rev. A **52**, 1086 (1995).

[88] R. G. Parr and W. Yang, *Density-Functional Theory of Atoms and Molecules* (Oxford University Press, 1994).

[89] F. Jense, *Introduction to Computational Chemistry* (John Wiley & Sons Ltd., Sussex, 2007).

[90] D. S. Sholl and J. A. Steckel, *Density Functional Theory* (Wiley & Sons Inc., New Jersey, 2009).

[91] D. Marx and J. Hutter, *Ab Initio Molecular Dynamics* (Cambridge University Press, New York, 2009).

[92] P. Hohenberg and W. Kohn, Phys. Rev. B **136**, 864 (1964), 1108.5632 .

[93] W. Kohn and L. Sham, Phys. Rev. **140**, A1133 (1965).

[94] J. Sun, M. Marsman, G. I. Csonka, A. Ruzsinszky, P. Hao, Y.-S. Kim, G. Kresse, and J. P. Perdew, Phys. Rev. B **84**, 035117 (2011).

[95] A. D. Becke., J. Chem. Phys. **98**, 1372 (1993).

[96] M. Payne, M. Teter, D. Allan, T. Arias, and J. Joannopoulos, Revi. Mod. Phys. **64**, 1045 (1992).

[97] G. Kresse and J. Furthmüller, Phys. Rev. B **54**, 11169 (1996).

[98] M. Born and H. Kuang, in *Dynamical Theory of Crystal Lattices* (Clarendon, Oxford, 1962) Chap. 4, p. 166.

[99] R. P. Feynman, Phys. Rev. **56**, 340 (1939).

[100] O. Nielsen and R. M. Martin, Phys. Rev. Lett. **50**, 697 (1983).

[101] R. Fletcher, *Practical Methods of Optimization* (John Wiley Sons, 1987).

[102] X. Gonze and J. P. Vigneron, Phys. Rev. B **39**, 13120 (1989).

[103] X. Gonze, D. C. Allan, and M. P. Teter, Phys. Rev. Lett. **68**, 3603 (1992).

[104] X. Gonze, Phys. Rev. B **55**, 10337 (1997).

[105] X. Gonze and C. Lee, Phys. Rev. B **55**, 10355 (1997).

[106] D. R. Hamann, K. M. Rabe, and D. Vanderbilt, Phys. Rev. B **72**, 1 (2005).

[107] D. R. Hamann, X. Wu, K. M. Rabe, and D. Vanderbilt, Phys. Rev. B **71** (2005).

[108] X. Wu, D. Vanderbilt, and D. R. Hamann, Phys. Rev. B **72**, 1 (2005).

[109] P. E. Blöchl, E. Smargiassi, R. Car, D. B. Laks, W. Andreoni, and S. T. Pantelides, Phys. Rev. Lett. **70**, 2435 (1993).

[110] P. G. Sundell, M. E. Björketun, and G. Wahnström, Phys. Rev. B **76**, 094301 (2007).

[111] C. Wert and C. Zener, Phys. Rev. **76**, 1169 (1949).

[112] E. M. Pell, Phys. Rev. **119**, 1222 (1960).

[113] D. A. Porter and K. Easterling, *Phase Transformation in Metals and Alloys*, 2nd ed. (Chapman and Hall, UK, London, 1994) pp. 60–109.

[114] H. Eyring, J. Chem. Phys. **3**, 107 (1935).

[115] M. G. Evans and M. Polanyi, Trans. Faraday Soc. **32**, 1333 (1936).

[116] G. Henkelman and H. Jónsson, J. Chem. Phys. **113**, 9978 (2000).

[117] G. Henkelman, B. P. Uberuaga, H. Jónsson, G. Henkelman, and H. Jo, J. Chem. Phys. **113**, 9901 (2000).

[118] J. K. Baird and E. M. Schwartz, Z. Phys. Chem. **211**, 47 (1999).

[119] C. P. Flynn and A. M. Stoneham, Phys. Rev. B **1**, 3966 (1970).

[120] J. T. Fermann and S. M. Auerbach, J. Chem. Phys. **112**, 6787 (2000).

[121] J. R. Hulett, Q. Rev. Chem. Soc. **18**, 227 (1964).

[122] G. H. Vineyard, J. Phys. Chem. Solids **3**, 121 (1957).

[123] A. Seeger, in *Hydrogen in Metals I.* (Springer, 1978) Chap. 13.

[124] I. O. Thomas and G. P. Srivastava, J. Phys. Condens. Matter **29** (2017).

[125] A. Fleszar and X. Gonze, Phys. Rev. Lett. **64**, 2961 (1990).

[126] P. Pavone, K. Karch, O. Schutt, W. Windl, D. Strauch, P. Giannozzi, and S. Baroni, Phys. Rev. B **48**, 3156 (1993).

[127] P. Varotsos and K. Alexopoulos, Phys. Rev. B **15**, 4111 (1977).

[128] P. Varotsos and K. Alexopoulos, Phys. Rev. B **30**, 7305 (1984).

[129] J. Moon, B. Lee, M. Cho, and K. Cho, J. Power Sources **328**, 558 (2016).

[130] Y. A. Du, J. Rogal, and R. Drautz, Phys. Rev. B **86**, 174110 (2012).

[131] T. Vegge, Phys. Rev. B **70**, 035412 (2004).

[132] A. B. Bortz, M. H. Kalos, and J. L. Lebowitz, J. Comput. Phys. **17**, 10 (1975).

[133] D. T. Gillespie, J. Comput. Phys. **22**, 403 (1976).

[134] R. Kirchheim, Acta Metall. **35**, 271 (1987).

[135] R. Kirchheim, Prog. Mater. Sci. **32**, 261 (1988).

[136] A. Ramasubramaniam, M. Itakura, M. Ortiz, and E. Carter, J. Mater. Res. **23**, 2757 (2008).

[137] K. A. Fichthorn and W. H. Weinberg, J. Chem. Phys. **95**, 1090 (1991).

[138] K. Lejaeghere, V. Van Speybroeck, G. Van Oost, and S. Cottenier, Crit. Rev. Solid State Mater. Sci. **39**, 1 (2014).

[139] L. He, F. Liu, G. Hautier, M. J. T. Oliveira, M. A. L. Marques, F. D. Vila, J. J. Rehr, G. M. Rignanese, and A. Zhou, Phys. Rev. B **89**, 064305 (2014).

[140] K. Lejaeghere et al., Science **351** (2016).

[141] J. Tersoff, Phys. Rev. B **38**, 9902 (1988).

[142] F. H. Stillinger and T. A. Weber, Phys. Rev. B **31**, 5262 (1985).

[143] M. I. Baskes, Phys. Rev. B **46**, 2727 (1992).

[144] R. L. C. Vink, G. T. Barkema, W. F. Van der Weg, and N. Mousseau, J. Non. Cryst. Solids **282**, 248 (2001).

[145] L. Pizzagalli, J. Godet, J. Guénolé, S. Brochard, E. Holmstrom, K. Nordlund, and T. Albaret, J. Phys. Condens. Matter **25**, 55801 (2013).

[146] S. Daw, Murray, M. Foiles, Stephen, and I. Baskes, Michael, Mater. Sci. Reports **9**, 251 (1993).

[147] J. Tersoff, Phys. Rev. B **37**, 6991 (1988).

[148] M. S. Daw and M. I. Baskes, Phys. Rev. B **29**, 6443 (1984).

[149] A. C. T. van Duin, S. Dasgupta, F. Lorant, and G. W. A., J. Phys. Chem. A **105**, 9396 (2001).

[150] F. Fan, S. Huang, H. Yang, M. Raju, D. Datta, V. B. Shenoy, A. C. T. van Duin, S. Zhang, and T. Zhu, Model. Simul. Mater. Sci. Eng. **21**, 074002 (2013).

[151] M. S. Daw and M. I. Baskes, Phys. Rev. Lett. **50**, 1285 (1983).

[152] B.-J. Lee, M. Baskes, H. Kim, and Y. Koo Cho, Phys. Rev. B **64**, 184102 (2001).

[153] Z. Cui, F. Gao, Z. Cui, and J. Qu, J. Power Sources **207**, 150 (2012).

[154] S. J. Cook and P. Clancy, Phys. Rev. B **47**, 7686 (1993).

[155] F. Aurenhammer, R. Klein, and D.-T. Lee, *Voronoï Diagrams and Delaunay Triangulations* (WORLD SCIENTIFIC, 2013).

[156] D. Waroquiers, X. Gonze, G. M. Rignanese, C. Welker-Nieuwoudt, F. Rosowski, M. Göbel, S. Schenk, P. Degelmann, R. André, R. Glaum, and G. Hautier, Chem. Mater. **29**, 8346 (2017).

[157] C. A. Fuller, Q. Berrod, B. Frick, M. R. Johnson, S. J. Clark, J. S. O. Evans, and I. R. Evans, Chemistry of Materials **31**, 7395 (2019).

[158] A. E. Shields, A. J. Miskowiec, K. Maheshwari, M. C. Kirkegaard, D. J. Staros, J. L. Niedziela, R. J. Kapsimalis, and B. B. Anderson, The Journal of Physical Chemistry C **123**, 15985 (2019).

[159] N. Wagner, D. Puggioni, and J. M. Rondinelli, Journal of Chemical Information and Modeling **58**, 2491 (2018).

[160] U. Kasavajjula, C. Wang, and A. J. Appleby, J. Power Sources **163**, 1003 (2007).

[161] D. Ma, Z. Cao, and A. Hu, Nano-Micro Lett. **6**, 347 (2014).

[162] L. Y. Beaulieu, K. W. Eberman, R. L. Turner, L. J. Krause, and J. R. Dahn, Electrochem. Solid-State Lett. **4**, A137 (2001).

[163] H. Li, X. Huang, L. Chen, Z. Wu, and Y. Liang, Electrochem. Solid-State Lett. **2**, 547 (1999).

[164] P. G. Bruce, B. Scrosati, and J. M. Tarascon, Angew. Chemie - Int. Ed. **47**, 2930 (2008).

[165] H. Kim, M. Seo, M. H. Park, and J. Cho, Angew. Chemie - Int. Ed. **49**, 2146 (2010).

[166] L. Luo, J. Wu, J. Luo, J. Huang, and V. P. Dravid, Sci. Rep. **4**, 3863 (2014).

[167] L. Luo, H. Yang, P. Yan, J. J. Travis, Y. Lee, N. Liu, D. Molina Piper, S. H. Lee, P. Zhao, S. M. George, J. G. Zhang, Y. Cui, S. Zhang, C. Ban, and C. M. Wang, ACS Nano **9**, 5559 (2015).

[168] X. H. Liu et al., Nat. Nanotechnol. **7**, 749 (2012).

[169] S. P. Kim, D. Datta, and V. B. Shenoy, J. Phys. Chem. C **118**, 17247 (2014).

[170] B. Key, R. Bhattacharyya, M. Morcrette, V. Seznéc, J.-M. Tarascon, and C. P. Grey, J. Am. Chem. Soc. **131**, 9239 (2009).

[171] N. Ding, J. Xu, Y. X. Yao, G. Wegner, X. Fang, C. H. Chen, and I. Lieberwirth, Solid State Ion. **180**, 222 (2009).

[172] G. A. Tritsaris, K. Zhao, O. U. Okeke, and E. Kaxiras, J. Phys. Chem. C **116**, 22212 (2012).

[173] H. Kim, K. E. Kweon, C. Y. Chou, J. G. Ekerdt, and G. S. Hwang, J. Phys. Chem. C **114**, 17954 (2010).

[174] Z. Wang, Q. Su, H. Deng, and Y. Fu, ChemElectroChem **2**, 1292 (2015).

[175] Z. Wang, Q. Su, H. Deng, W. He, J. Lin, and Y. Q. Fu, J. Mater. Chem. A **2**, 13976 (2014).

[176] H.-H. Chiang, J.-M. Lu, and C.-L. Kuo, J. Chem. Phys. **144**, 034502 (2016).

[177] H. Kim, C.-Y. Chou, J. G. Ekerdt, and G. S. Hwang, J. Phys. Chem. C **115**, 2514 (2011).

[178] P. Johari, Y. Qi, and V. B. Shenoy, Nano Lett. **11**, 5494 (2011).

[179] M. Dixit, H. Engel, R. Eitan, D. Aurbach, M. D. Levi, M. Kosa, and D. T. Major, J. Phys. Chem. C **119**, 15801 (2015).

[180] C. O. Hwang, J. Chem. Phys. **125**, 2004 (2006).

[181] N. Sandberg, B. Magyari-Köpe, and T. R. Mattsson, Phys. Rev. Lett. **89**, 065901 (2002).

[182] M. Mantina, Y. Wang, R. Arroyave, L. Q. Chen, Z. K. Liu, and C. Wolverton, Phys. Rev. Lett. **100**, 215901 (2008).

[183] D. Zhao, Y. Kong, A. Wang, L. Zhou, S. Cui, X. Yuan, L. Zhang, and Y. Du, J. Phase Equilibria Diffus. **32**, 128 (2011).

[184] C. P. Flynn, Zeitschrift fur Naturforsch. - Sect. A J. Phys. Sci. **26**, 99 (1971).

[185] G. DeLorenzi, C. P. Flynn, and G. Jacucci, Phys. Rev. B **30**, 5430 (1984).

[186] V. Saltas, A. Chroneos, and F. Vallianatos, J. Mater. Sci.: Mater. Electron **29**, 12022 (2018).

[187] E. Wimmer, W. Wolf, J. Sticht, P. Saxe, C. B. Geller, R. Najafabadi, and G. A. Young, Phys. Rev. B **77**, 134305 (2008).

[188] P. Varotsos, W. Ludwig, and K. Alexopoulos, Phys. Rev. B **18**, 2683 (1978).

[189] P. Varotsos, J. Appl. Phys. **101** (2007), 10.1063/1.2745359.

[190] A. Chroneos, Appl. Phys. Rev. **3** (2016).

[191] H. Okamoto, J. Phase Equilibria Diffus. **30**, 118 (2009).

[192] M. H. Braga, A. Dębski, and W. Gąsior, J. Alloys Compd. **616**, 581 (2014).

[193] V. L. Chevrier, J. W. Zwanziger, and J. R. Dahn, Can. J. Phys. **87**, 625 (2009).

[194] L. A. Stearns, J. Gryko, J. Diefenbacher, G. K. Ramachandran, and P. F. McMillan, J. Solid State Chem. **173**, 251 (2003).

[195] X. Gonze et al., Comput. Mater. Sci. **25**, 478 (2002).

[196] X. Gonze et al., Z. Kristallog. **220**, 558 (2005).

[197] X. Gonze et al., Comput. Phys. Commun. **180**, 2582 (2009).

[198] X. Gonze et al., Comput. Phys. Commun. **205**, 106 (2016).

[199] J. P. Perdew, K. Burke, and M. Ernzerhof, Phys. Rev. Lett. **77**, 3865 (1996).

[200] D. R. Hamann, Phys. Rev. B **88**, 085117 (2013).

[201] M. J. van Setten, M. Giantomassi, E. Bousquet, M. J. Verstraete, D. R. Hamann, X. Gonze, and G. M. Rignanese, Comput. Phys. Commun. **226**, 39 (2018).

[202] M. Methfessel and A. T. Paxton, Phys. Rev. B **40**, 3616 (1989).

[203] Q. Zhang, W. Zhang, W. Wan, Y. Cui, and E. Wang, Nano Lett. **10**, 3243 (2010).

[204] R. Caracas, R. G.-M., and X. Gonze, Z. Kristallog. **220**, 458 (2005).

[205] F. D. Murnaghan, Proc. Natl. Acad. Sci. U. S. A. **9**, 244 (1944).

[206] J. Moon, B. Lee, M. Cho, and K. Cho, J. Power Sources **272**, 1010 (2014).

[207] A. S. Fedorov, Z. I. Popov, A. A. Kuzubov, and S. G. Ovchinnikov, JETP Lett. **95**, 143 (2012).

[208] D. E. Jiang and E. A. Carter, Phys. Rev. B **70**, 064102 (2004).

[209] A. G. Morachevskii and A. I. Demidov, Russ. J. Appl. Chem. **88**, 547 (2015).

[210] A. F. Voter, Phys. Rev. Lett. **63**, 167 (1989).

[211] G. Voth, J. Phys. Chem. **97**, 8365 (1993).

[212] P. E. Blöchl, C. G. Van de Walle, and S. T. Pantelides, Phys. Rev. Lett. **64**, 1401 (1990).

[213] H. Grabert and H. R. Schober, in *Hydrogen in Metals III*, edited by H. Wipf (Springer, Berlin, Heidelberg, 1997) Chap. 2.

[214] D. Di Stefano, *First-principles investigation of hydrogen interaction with metals*, Ph.D. thesis, Albert-Ludwigs-Universitat Frieburg (2016).

[215] J. Evers, G. Oehlinger, and G. Sextl, Angew. Chemie Int. Ed. English **32**, 1442 (1993).

[216] F. Taubert, S. Schwalbe, J. Seidel, R. Hüttl, T. Gruber, R. Janot, M. Bobnar, R. Gumeniuk, F. Mertens, and J. Kortus, Int. J. Mater. Res. **108**, 942 (2017).

[217] K. J. Kim, J. Wortman, S.-Y. Kim, and Y. Qi, Nano Lett. (2017).

[218] J. Rohrer and K. Albe, J. Phys. Chem. C **117**, 18796 (2013).

[219] V. L. Chevrier, H. M. Dahn, and J. R. Dahn, J. Electrochem. Soc. **158**, A1207 (2011).

[220] N. Liao, B. Zheng, H. Zhou, and W. Xue, Electrochim. Acta **156**, 115 (2015).

[221] W. W. Tipton, C. R. Bealing, K. Mathew, and R. G. Hennig, Phys. Rev. B **87**, 184114 (2013).

[222] E. D. Cubuk and E. Kaxiras, Nano Lett. **14**, 4065 (2014).

[223] V. L. Chevrier and J. R. Dahn, J. Electrochem. Soc. **157**, A392 (2010).

[224] A. Urban, D.-H. Seo, and G. Ceder, npj Comput. Mater. **2**, 16002 (2016).

[225] L. Y. Beaulieu, T. D. Hatchard, A. Bonakdarpour, M. D. Fleischauer, and J. R. Dahn, J. Electrochem. Soc. **150**, A1457 (2003).

[226] E. D. Cubuk, W. L. Wang, K. Zhao, J. J. Vlassak, Z. Suo, and E. Kaxiras, Nano Lett. **13**, 2011 (2013).

[227] K. Laaziri, S. Kycia, S. Roorda, M. Chicoine, J. L. Robertson, J. Wang, and S. C. Moss, Phys. Rev. Lett. **82**, 3460 (1999).

[228] J. Godet, T. Bunjaku, and M. Luisier, 'Lithiation-delithiation cycles of amorphous Si nanowires investigated by molecular dynamics simulations,' (2019), arXiv:1909.03268 .

[229] S. J. Plimpton, J. Comput. Phys. **117**, 1 (1995).

[230] S. Schwalbe, T. Gruber, K. Trepte, F. Biedermann, F. Mertens, and J. Kortus, Computational Materials Science **134**, 48 (2017).

[231] H. Wang, X. Ji, C. Chen, K. Xu, and L. Miao, AIP Adv. **3** (2013).

[232] H. Wang and H. B. Chew, Extrem. Mech. Lett. **9**, 503 (2016).

[233] J. Wang and S. C. Moss, Phys. Rev. B **60**, 13520 (1999).

[234] G. Wang, B. Xu, J. Shi, X. Lei, and C. Ouyang, Appl. Surf. Sci. **436**, 505 (2018).

[235] R. Hu and J. Zhou, Appl. Surf. Sci. **457**, 789 (2018).

[236] X. Gao, J. Li, Y. Xie, D. Guan, and C. Yuan, ACS Appl. Mater. Interfaces **7**, 7855 (2015).

[237] S. Zhu, J. Zhou, Y. Guan, W. Cai, Y. Zhao, Y. Zhu, L. Zhu, Y. Zhu, and Y. Qian, Small **1802457**, 1 (2018).

[238] B. Van Troeye, A. Lherbier, J. C. Charlier, and X. Gonze, Phys. Rev. Mater. **2**, 1 (2018).

[239] S. Rajagopalan, Nuovo Cim. B Ser. 11 **51**, 222 (1979).